Accurate Abundances of Giant Stars in the Local disk

A manual analysis of IR APOGEE spectra

Ivalu Barlach Christensen

Lund Observatory
Lund University

2020-EXA160

Degree project of 60 higher education credits (for a degree of Master)
May 2020

Supervisor: Nils Ryde

Lund Observatory
Box 43
SE-221 00 Lund
Sweden

Abstract

Purpose: In order to study the Galactic Chemical Evolution, elemental abundances are needed. The purpose of this work is to investigate the chemical evolution of the Milky Way by determining several elemental abundances of giants in the local disk. Large surveys are up and coming, and several surveys are already working, and with these, the aim is high quality abundance measurements of several elements of several thousands of stars. Apache Point Observatory Galactic Evolution Experiment (APOGEE) analyses abundances using a fast pipeline, industrialized to encompass measurements of all stars with the wealth of data. This pilot-study aims to investigate how accurate and precise the abundances can be measured and gain as much scientific information from the spectra by reanalyzing a sub-sample of APOGEE abundance measurements manually.
Method: The data used is a subset of IR spectra from the APOGEE survey, of giant stars that have also been analyzed accurately using high resolution optical spectra, which thus can be used as a benchmark. The stellar sample consists of 291 spectra in the local disk giants with a resolution of 22 500 and signal-to-noise of above 100. Giant stars enable us to probe deeper into the Milky Way. The stellar parameters of these stars have been determined in the optical in order to be as independent from APOGEE as possible. The abundances are determined by synthesizing a spectrum compared to the observed spectrum with focus on the line of interest using Spectroscopy Made Easy (SME), and the giants are assigned to the thin and thick disk using optical measurement.
Results: Abundance elements of light elements (Na, Al, K), α-elements (Mg, Si, S, Ca, Ti), iron peak elements, (V, Cr, Co, Ni), and neutron-capture elements (Cu and Ce) are determined. The traditional method of spectral synthesis will allow for each line of interest of each element to be investigated and allow for **manual** inspection of each analysis, thus maximizing the accuracy and precision without calibration. Using available distance measurements of the sample, ages are determined, showing higher α-abundance in older stars.
Conclusions: A manual analysis gives more accurate and precise abundance measurements, showing it is beneficial to measure APOGEE spectra with this method.

Acknowledgements

I would like to thank my supervisors, Nils Ryde and Henrik Jönsson, for the constant encouragement and trust during this work. Brian Thorsbro, Rebecca Forsberg and Martin Montelius for the weekly meetings. Jane Lund Plesner and my parents for supporting me through thesis-writing, and Laura L. Jensen for supporting me with reading parts of my thesis throughout the work. I would like to thank the Government of Greenland for financially supporting me through my masters, and thanks to J.G.C. for keeping me sane during the proofreading process.

Popular Science Summary

> ”She used to dream of the sun,
> the stars and the moon.”
>
> 14-year-old girl by Laura Aviana

In greenlandic myths, our ancestors rise to the heavens and are perpetuated as stars, forever watching over us. Although astronomy has proven that stars are complex balls of gas, just like our Sun, there is one thing astronomy and greenlandic myths agree on: stars are a window to the past.

13.7 billion years ago, the simplest elements were formed; hydrogen and helium. Stars are formed of these elements, fueled by hydrogen. The temperature inside stars allows for a process called *nucleosynthesis*, where hydrogen is burned into helium, releasing energy as heat. This process occurs during the lifetime of a star, until the star burns all the hydrogen inside.

The strongest tool of an astronomer is light. Light can be split into its constituents, known as *spectroscopy*. In the 1850s, Gustav Kirchoff explained that the dark lines in our Sun’s spectrum, also known as the Fraunhofer lines, are related to the material present in the atmosphere. Elements on the surface of a star absorb specific colors, creating darker lines in the spectrum of light.

Elements are formed in different environments. The elements in the periodic table are arranged according to the number of protons in the nucleus of an atom. In the core of stars, elements can be formed up until iron, the 26th element in the periodic table. With similar formation processes in stars, the periodic table can be split in four groups. The elements lighter than iron are divided into the *odd*-elements, which are odd-numbered, and α-elements, which are even-numbered. In the periodic table, the elements around iron are referred to as *iron-peak* elements, named due to their abundance in our Solar System. Elements heavier than iron are formed through a process called *neutron-capture*, where the nucleus of an atom grows by capturing the free neutrons, which is also a building block in a nucleus. Which elements are formed inside stars are also dependent on the mass of the star, because the mass determines the temperature inside stars.

The mass of a star determines the fate of a star. More massive stars have shorter lives, as they burn their hydrogen faster. The short-lived, massive stars form heavier elements, enriching our Galaxy through a spectacular explosion, known as a *supernova*. The material ejected by stars are building materials for the next generation of stars. Yet, the more abundant type of stars - much like our Sun - can live as long as the age of our Universe today. These long-lived, lower-mass stars enrich our Galaxy later, allowing us to analyze how the dust, that forms stars, has changed since the beginning of the Milky Way.

The cycle of stars forming from dust created by stars means that younger stars contain more heavier elements. As a star contains the information of their birth environment, observing several stars of different ages can tell us how their birthplace - the dust in our home Galaxy - has formed and evolved.

In this thesis, I have analyzed the composition of 291 giant stars in the neighborhood of our Sun to investigate how our Galaxy has evolved. These stars have been observed with Apache Point Observatory Galactic Evolution Experiment, APOGEE, measuring giant stars in the infrared wavelength. Giant stars are very bright, making it possible for us to see those that are more distant in our Galaxy. The dust, expelled by the death of stars, is transparent to infrared light. 14 elements of the four element-groups are measured in these 291 stars in this work. The abundances of the different groups show that they are formed in similar ways inside stars. These abundances also show that the lower mass stars are enriching our Galaxy later due to their long lifetimes. I show that a careful analysis of abundance measurements give better results, and this gives a better insight to how our Milky Way has evolved.

Contents

List of Figures

List of Tables

Chapter 1

Introduction

Understanding our home in the Universe, how it was formed and how it has evolved through time is one of the oldest questions in astrophysics. A modern study in astrophysics is the study of how galaxies form and evolve, which is studied intensively to understand the evolution of our galaxy, the Milky Way. Since Newton (1672) introduced his theory of light, stars have shown to be more than just mere dots in our night sky. Stars are born from massive molecular clouds, enriched in chemistry by the death of stars, and will contribute in heavier elements when they die. Elemental abundances are therefore great tracers of the galactic chemical evolution. The abundance of elements depend on the nature of the enrichment, through different types of nucleosynthetic processes. To this end, large spectroscopic surveys are up and coming, supplying abundance measurements of several elements of several hundred thousands stars.

Following the Copernican thinking, the Milky Way is not an unusual galaxy, which makes it a benchmark galaxy for studying galaxy evolution. The Milky Way is thought to be a typical spiral galaxy (Bland-Hawthorn & Gerhard 2016), providing a great probe to study spiral galaxies. In the first landmark paper of the subject of galactic chemical evolution, Edvardsson et al. (1993) studied a large sample, for the time, of 189 stars, determining abundances of disk stars, in order to constrain the chemical evolution. This seminal paper is still the basis of the field. The Milky Way is indeed an important benchmark, as the components, that make up our galaxy, the stars, can be fully resolved and investigated. This allows us to study the chemical compositions of individual stellar atmospheres, thus a window to the interstellar medium through time. A schematic overview of the Milky Way components can be seen in figure 1.1, with the bulge/bar, the thin and thick disk and a stellar halo surrounding it all (Bland-Hawthorn & Gerhard 2016).

Several models have been suggested to explain the dichotomy of morphological and elemental abundances with metallicity of the thin and thick disk, observed by e.g. Adibekyan et al. (2011); Bensby et al. (2014). The leading chemical evolution model by Chiappini et al. (1997) suggests the formation of the thin disk and thick disk/halo occurring due to two major gas accretion events of pristine gas. Spitoni et al. (2019) show a two-infall

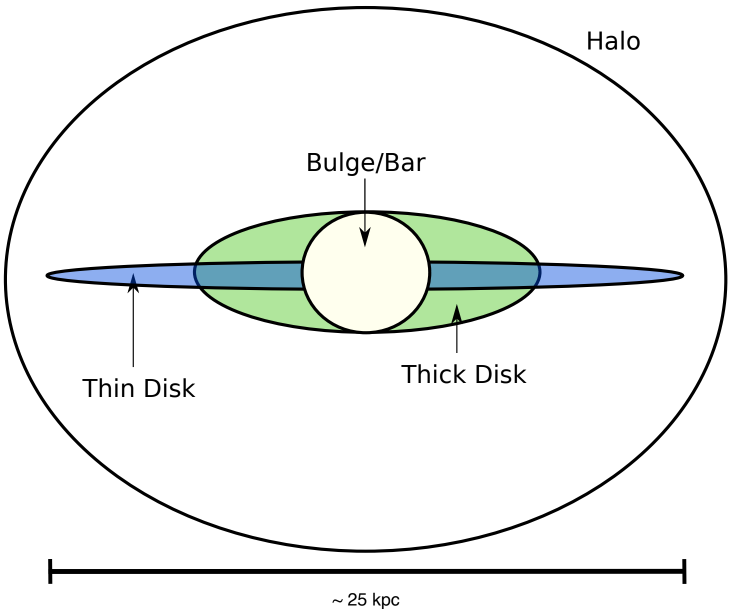

Figure 1.1: A schematic illustration of the stellar components of the Milky Way. The green shows the thick disk, the blue shows the thin disk, the beige indicates the bulge/bar and the white surrounding it all indicates the stellar halo.

model with a delayed second gas infall which can explain the observed measurements by Hayden et al. (2015). Recent studies have investigated the chemical compositions of individual stars giving clues to where the stars were born (Minchev et al. 2018). The trends of elements formed by SNe II of the inner parts of the galaxy using APOGEE-measurements can be explained with a single evolutionary track, suggesting a uniform evolution (Hayden et al. 2015). Investigating the age-[Fe/H] relation using APOGEE, Feuillet et al. (2016) used a sample of 705 local giants with known distances, and suggested that radial migration results in a larger spread in overall metallicity [M/H] for older stars than younger stars.

In discussing the element trends, [X/Fe] vs. [Fe/H], for understanding the galactic chemical evolution, four main groups of elements are identified, based on their presumed nucleosynthetic formation channels. The four main groups of elements are light/odd-Z elements, α-elements[1], iron-peak elements and neutron-capture elements. Several papers have measured elemental abundances in the optical both in dwarf and giant stars.

Using dwarf stars, Bensby et al. (2014) determined detailed abundance-measurements, investigating light-, α and iron-peak elements. Adibekyan et al. (2012) argued a difference in orbital parameters between the thin and thick disk. Battistini & Bensby (2016) investigated the evolution of r- and s-process elements, both using dwarf and sub-giant stars

---

[1] α-elements are elements that are formed through the triple α-process, and heavier elements are formed by adding an α-element/^{4}He.

investigating the Milky Way stellar disk in the Solar neighbourhood.

Giants have lower surface gravities and effective temperatures and consequently have higher spectral line density due to molecular lines, but Jönsson et al. (2017) demonstrated that giants are excellent as probes for abundance measurements as long as one is careful with blending of lines. Jönsson et al. (2017) and Jönsson et al. (2017b) investigated the abundances of α-elements (oxygen, magnesium, calcium and titanium) using giants measured in the optical regime. Following these papers, iron-peak elements scandium, vanadium, chromium, manganese, cobalt and nickel abundances by Lomaeva et al. (2019), and neutron-capture elements zirconium, lanthanum, cerium and europium abundances by Forsberg et al. (2019), have been determined in the bulge and compared with the Milky Way disks using giants.

Each element is a product of the environment, and the observation of an element can constrain a possible scenario that has occurred in the past, giving clues to the cosmic origins of elements as well as the interstellar medium. The mean α-abundances measured shift toward lower [Fe/H] in the outer regions, which is explained by an "inside-out formation" (Spitoni et al. 2019). Spitoni & Matteucci (2011) investigated the effects of radial gas flow, concluding that inside-out formation of the galaxy with varying star formation efficiency and radial gas flow all have an effect on the abundance gradients in the disk.

A large sample of stars to investigate the Galaxy, unveiling the evolution of our galaxy, as well as investigating the sub-populations, is of high demand. A new era of large surveys, such as *Gaia-ESO* (Gilmore et al. 2012), *GALactic Archeology with HERMES* (GALAH) (Buder et al. 2018) and *Apache Point Observatory Galactic Evolution Experiment* (APOGEE) (Majewski et al. 2017), are devised to specifically study the chemical evolution of the Milky Way. The abundance trends from the APOGEE survey have indeed led to a large activity in the field of galactic chemical evolution observations. This thesis is devised to develop a method tailored for specific stars in order to increase the accuracy. This method allows for a more time-consuming analysis with accurate atomic data resulting in high quality measurements of abundances, with the aim to observe something never seen before, e.g. sub-populations.

APOGEE measures spectra with high signal-to-noise ratio at medium resolution, providing spectra of sufficient quality for abundance measurements. With the newest data release of APOGEE of an astounding 473,307 spectra (Ahumada et al. 2019), it is appealing to obtain as much scientific results fast. Previous studies using abundance measurements from *APOGEE Stellar Parameters and Chemical Abundance Pipeline* (ASPCAP), have used a sub-sample of specific stars. Although APOGEE releases several 100,000s spectra in each data release (Holtzman et al. 2018), only a fraction of the entire sample are used to investigate the galactic chemical evolution (e.g. Hayden et al. (2015); Feuillet et al. (2016)). APOGEE has several sub-projects, thus observes and measures abundances of dwarfs and giants simultaneously, to fulfill each sub-projects, e.g. cool dwarf measurements to study stellar ages (Claytor et al. 2019). With the continuous release and development of APOGEE, advancements of acquiring accurate abundances are of interest (Hawkins et al. 2016). In a recent paper, Sarmento et al. (2020) determined the stellar parameters manually using FGK-giants, supporting manual analysis to improve measurements specifically for a sub-sample.

Investigating our Galaxy, as well as investigating the sub-populations with high accuracy, are the goals of fully constraining the chemical evolution. The advantage of using giants is that it is possible to probe deeper into the Milky Way. The near-infrared wavelength regime of APOGEE allows for observations in the galactic dust plane. With the two telescopes in both hemispheres, as well as the window through the dust plane and using giants to probe deeper, APOGEE gives a large possibility to investigate the entire Milky Way.

This pilot-study aims to obtain accurate and precise **abundance** measurements of several elements from near-IR APOGEE spectra. A method devised specifically to study **K-giants** should minimize systematic errors due to approximations covering different stars. I will investigate a bench-marked sub-sample of **local disk** stars, with accurate stellar parameters determined using optical spectra (Jönsson et al. 2017), with the aim to support the measurements of APOGEE, to ensure a large sample of accurate and precise abundance measurements, and to investigate how well these spectra can be measured, and how much better accuracy and precision can be achieved using a manual method. The atomic data as well as the spectra are manually analyzed to ensure high precision in elemental abundances compared with abundance measurements by Jönsson et al. (2017b), Lomaeva et al. (2019) and Forsberg et al. (2019). A goldmine of data-sets are delivered from the **IR-survey, APOGEE**, and obtaining as much information with large, cherry-picked sub-samples of stars from the wealth of **spectra** is the final goal.

Chapter 2

Background Theory

In this chapter, the background science of stellar evolution and how elements are formed are discussed. The four elemental groups consisting of light, α, iron-peak and neutron-capture elements have different production channels. Knowledge of the stellar cycle as well as the cosmic origin of elements helps discern the building blocks of the cosmos.

Since the primordial nucleosynthesis shortly after the big bang, where hydrogen, helium and lithium were formed, stars have been involved in the production of elements in nature. The cosmic origin of many of the elements are well-constrained, but for some, the production channels are still debated. The periodic table can be split in four groups, based on their formation channel: 1) the *odd-Z*, odd-numbered, and 2) α-elements, even-numbered in the periodic table for elements up until 3) the *iron-peak* elements, which are the elements with peak abundances in the solar system around iron. Above iron, $A > 56$, are 4) the *neutron-capture* elements, growing the nuclei by capturing free neutrons.

Stars evolve due to the evolving interior and spend most of the lifetime in the main sequence, synthesizing hydrogen to helium in the core. The timescales of the main sequence stage highly depend on their initial masses, with solar mass stars being at this stage for $\sim$ 10 billion years and high mass stars for $\sim$ 100 million years.

Stars with different masses, enriching the interstellar medium at different timescales, also enrich the interstellar medium with different elements. Heavier elements than helium, are formed in the later stages, when the process of the stellar death begins. When a star leaves the main sequence stage and exhaust the core of hydrogen, further evolution also depends on the initial mass of the star.

For low mass stars (< 8 $M_\odot$), the temperatures do not reach high enough for further nucleosynthesis than the pp-chain[1], CNO-cycle[2] and triple-α-process, described further in section 2.2.1. When the core has exhausted hydrogen, the stars evolve to the red giant branch. After the He-core flash, the stars evolve to the horizontal branch or red clump stars for metal-rich stars where the core synthesizes helium to carbon and hydrogen to helium in a thin shell outside the core. Before the stars reach the horizontal branch stage, for stars with masses < 4 $M_\odot$, the first dredge up occurs in the convective envelope, homogenizing 80% of the stellar mass (Busso et al. 1999). For the final stages of the death, the core contracts, expanding the outer layers and the star evolves to the asymptotic giant branch, which has two burning shells. No further evolution occurs, and nucleosynthesis terminates. The core contracts expelling the convective zone, including the synthesized material, resulting in a planetary nebula, and the remaining core left forms a white dwarf with a carbon-oxygen core. Planetary nebulae for lower masses enrich the interstellar medium with helium and carbon.

Despite lower mass stars having terminated nucleosynthesis, there is a caveat for further evolution. A significant fraction of lower mass stars are in binary systems. During the later stages, as the envelope expand, the companion white dwarf can accrete the envelope of its companion. The increase of mass during the accretion increases the temperature due to the negative heat capacity of stars, thus re-igniting nucleosynthesis and form heavier elements. The once dead star evolves further, exploding again with a supernovae (SNe) type I (Matteucci & Greggio 1986). SNe I effectively produce elements like sodium and iron.

The death of intermediate mass stars, ($\sim$ 4-8 $M_\odot$) leaves a core of heavier elements. The intermediate masses synthesize carbon and oxygen in the core, where the helium-shell outside the core ignites the CNO-cycle. The asymptotic giant branch-phase occurs in stars < 8 $M_\odot$, where the third dredge-up occurs. Strong winds will expel these elements to the ISM. With the ^{13}C-pocket in asymptotic giant branch-stars, s-process elements are effectively synthesized. The third dredge-up mixes these heavier elements to the surface in addition to helium and carbon. The second dredge-up occurs only for the heavier intermediate mass stars of > 3.5 $M_\odot$ (Busso et al. 1999), effectively mixing the products of the CNO-cycle to the surface.

For high mass stars (> 8 $M_\odot$), the core continues to synthesize elements up until iron (A = 56), having shells of hydrogen, helium, carbon, oxygen and silicon. Within these shells, burning occurs, effectively synthesizing α-elements, described in more details below. The energetic collapse with subsequent explosion of high mass stars is called SNe type II. For the more massive stars of high mass stars (> 60 $M_\odot$) the energy expulsion is higher, where these are referred to as hypernovae (Grimmett et al. 2019). The energetic expulsion of the convective zone leaves a neutron star or a black hole.

---

[1] The proton-proton chain reaction synthesized hydrogen to helium, effectively having the reaction $4\ {}^{1}\mathrm{H} \rightarrow {}^{4}\mathrm{He} + 2\ \mathrm{e}^{+} + 2\nu_e$.

[2] The CNO-cycle occurs in more massive stars, where carbon, nitrogen and oxygen are available. Hydrogen increases the C, N and O, effectively having the reaction ${}^{12}\mathrm{C} + 4\ {}^{4}\mathrm{He} \rightarrow {}^{12}\mathrm{C} + {}^{4}\mathrm{He}$.

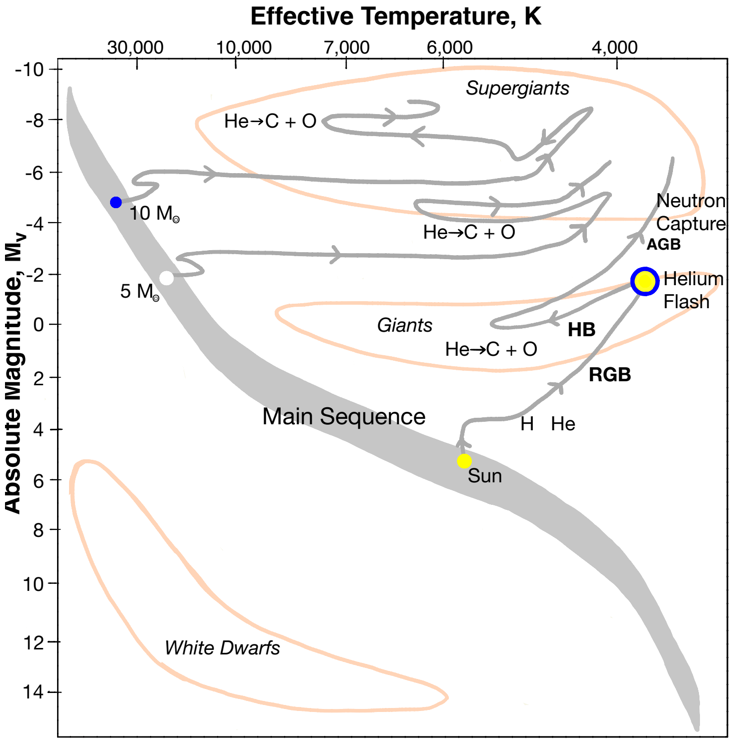

Figure 2.1: The evolutionary stages of a solar-like, 5 M$_\odot$ and 10 M$_\odot$ star can be seen in this HR diagram. The nucleosynthesis of hydrogen and helium-burning are indicated. The evolutionary stages of red giant branch (RGB), horizontal branch (HB) and asymptotic giant branch (AGB) are indicated as well.

The evolutionary stages of solar-like, 5 M$_\odot$ and 10 M$_\odot$ stars on an HR diagram can be seen in figure 2.1. Examples of where nucleosynthesis is favored are indicated.

Different masses and different stages produce elements with different timescales. Although, investigating all elemental abundances, or at least elements of different groups, is of desire, this is unfortunately not possible since some elements have no spectral lines or lines too weak for abundance measurements.

2.1 Elements of Interest

Within the wavelength-range of APOGEE, the elements with spectral lines strong enough to derive a stellar abundance are marked in the periodic table in figure 2.2. APOGEE primarily targets giant stars, and the sample (which is described later in detail, see section 3.1) is benchmarked by optical measurements of giants in the local disk. The elements of interest are odd-Z -, α -, iron-peak - and neutron-capture elements (marked pink, blue, ivory and green, respectively) in figure 2.2. Elements of these different nucleosynthetic origins

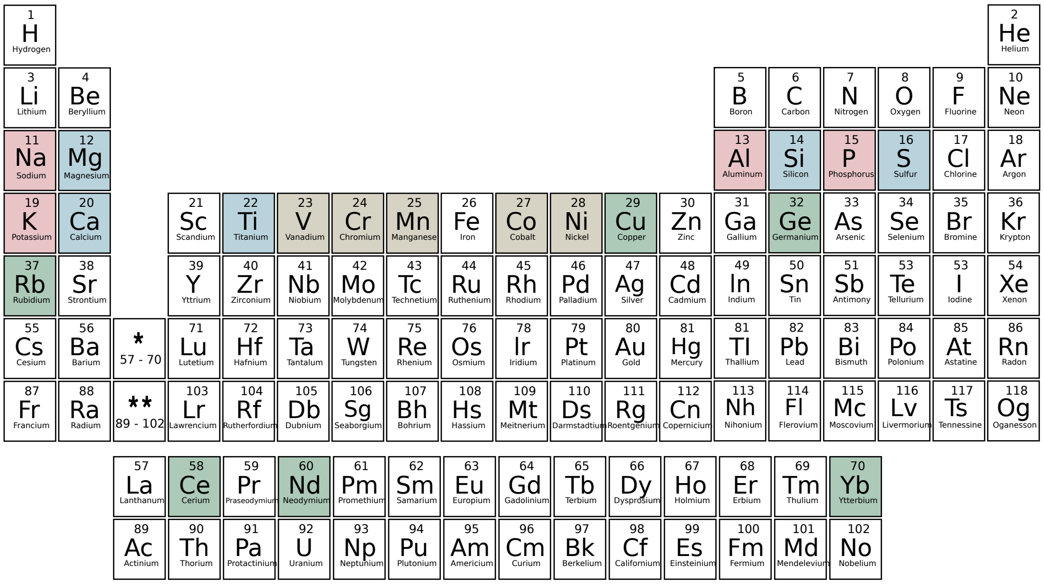

Figure 2.2: The periodic table shows the elements of interest, that are observable within the range of APOGEE (colored). Odd Z-elements are marked pink, α-elements are blue, iron-peak elements are ivory and neutron-capture elements are green.

are investigated: Sodium (Na), aluminium (Al), phosphorous (P) and potassium (K) are the odd Z-elements; magnesium (Mg), silicon (Si), sulphur (S), calcium (Ca) and titanium (Ti) are the α-elements; vanadium (V), chromium (Cr), manganese (Mn), cobalt (Co) and nickel (Ni) as the iron-peak elements; and copper (Cu), germanium (Ge), rubidium (Rb), cerium (Ce), neodymium (Nd) and Ytterbium (Yb) as the neutron-capture elements.

2.2 Nucleosynthesis

Hoyle (1946) first proposed that nucleosynthesis occurs in stellar interior, due to the high temperature and density of elements, and later Burbidge et al. (1957) expanded the theory with nucleosynthesis to occur through neutron capture. Due to the averaged binding energy per nucleon (see figure 2.3), elements with $A \leq 56$ are formed through exothermic processes, providing the power source of stars, and an endothermic formation process of $A > 56$. In the discussion below, the elements investigated in this thesis are highlighted with boldface.

2.2.1 Odd- and α-Elements

In this thesis, the focus of odd Z-elements are sodium, aluminium, phosphorous and potassium. The α-elements investigated here are magnesium, silicon, sulphur, calcium and

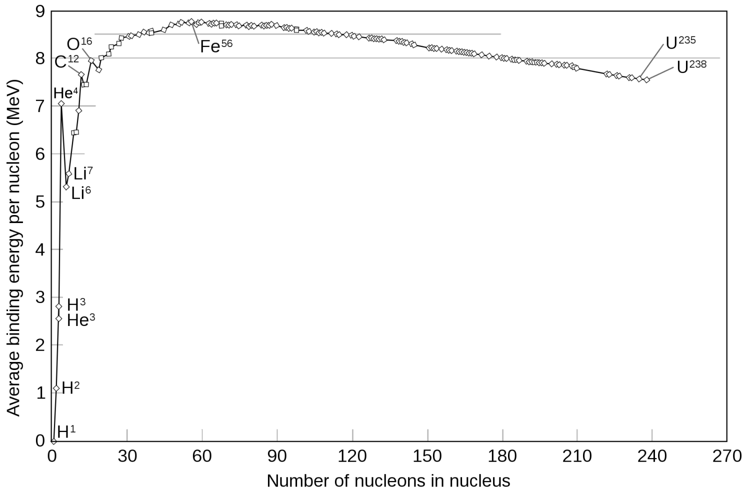

Figure 2.3: The figure shows the average binding energy per nucleon, showing nuclear fusion occurs up until ^{56}Fe. The figure is adopted from `https://en.wikipedia.org/wiki/Iron-56#/media/File:Binding_energy_curve_-_common_isotopes.svg`

titanium, see section 2.1. These elements are mainly formed through the capture of an α-particle, mainly in SNe II.

As previously explained, high mass stars develop thin shells of "heavier" elements outside the core. Nucleosynthesis occurs within these shells, and are highly temperature dependent. Due to the negative heat capacity, as energy is lost from the star, the temperature rises.

The burning stages occur only when the preceding burning has completed. Within stars, these burning reactions occur mainly due to fusion with an α-particle, increasing the element, Z, with two in the core. The reactions that occur during α-burning produce the Odd-Z and α-elements.

Hydrogen Burning Hydrogen burning occurs during the main sequence stage of evolution, providing the energy source of the star. In the stellar interior, the temperature of the core allows for proton-proton chain reactions, where four hydrogen-elements form one helium. In more massive stars than our Sun, the reaction of forming helium occurs during the CNO-cycle.

Helium Burning As hydrogen is exhausted from the core, the following burning that occurs is helium burning. When helium-burning occurs, the star has entered the horizontal branch stage, where helium nuclei are fused into carbon. The triple-α reaction occurs during a high α-density, and the capture of another α-particle is required before the short-lived ^{8}Be (2α) breaks apart into two α-particles again. During the helium-burning-phase, and as the stable ^{12}C is produced, another α-particle can be captured, producing ^{16}O. The helium burning effectively produces carbon and oxygen.

Explosive helium-burning occurs during the end stages of the energetic death of massive stars, where temperatures are high enough for the triple-α reaction to occur.

Carbon Burning When helium is exhausted from the core, more massive stars can reach a higher temperature due to the negative heat capacity. The contraction allows for temperatures of $> 5 \cdot 10^8$ K in the core (Clayton 1983), allowing for carbon burning to occur during the end-stage of the red-giant phase. The two main reactions during the carbon burning are the binary-collision of carbon-nuclei:

$$^{12}\mathrm{C} +^{12} \mathrm{C} \rightarrow^{20} \mathrm{Ne} +^{4} \mathrm{He}, \quad \text{and} \tag{2.1}$$

$$^{12}\mathrm{C} +^{12} \mathrm{C} \rightarrow^{23} \mathrm{Na} +^{1} \mathrm{H} \tag{2.2}$$

Secondary reactions during the carbon burning produces an abundant ^{24}Mg + n by fusing two carbon nuclei.

During SNe I, a runaway carbon burning occurs, and during SNe II, a shock wave due to the pre-supernova occurs, allowing explosive carbon-burning to occur rapidly. This quick process produces high abundances of **Mg**, **Na** and **Al** (Clayton 2003).

Neon Burning Succeeding the carbon burning, the core contracts until the temperature reaches $\sim 1.2 \cdot 10^9$ K and neon-burning starts. A significant effect at these temperatures is photodisintegration, where α-particles are released. The main reactions during neon burning are (Clayton 1983):

$$^{20}\mathrm{Ne} + \gamma \rightarrow^{16} \mathrm{O} +^{4} \mathrm{He} \tag{2.3}$$

and an abundance of **Mg** is produced with the released α-particle:

$$^{20}\mathrm{Ne} +^{4} \mathrm{He} \rightarrow^{24} \mathrm{Mg} + \gamma \tag{2.4}$$

During the explosive neon burning of a massive star's death, a significant amount of **Al** and **P** is formed (Morgan 1980).

Oxygen burning As the carbon - and neon burning ceases to provide the nuclear fusion in the core of stars, the core contraction causes the temperature to rise further. This allows for oxygen burning to occur around 2.7-3.5 $\cdot 10^9$ K. The main synthesis is the binary-collision of oxygen (Clayton 2003):

$$^{16}\mathrm{O} +^{16} \mathrm{O} \rightarrow^{28} \mathrm{Si} +^{4} \mathrm{He} \tag{2.5}$$

$$\rightarrow^{31} \mathrm{P} +^{1} \mathrm{H} \tag{2.6}$$

$$\rightarrow^{32} \mathrm{S} \tag{2.7}$$

Due to secondary reactions contributing, Si is the most abundant element during the oxygen-burning, yet a significant abundance of **S** and **Ca** is produced during this phase (Clayton 2003).

During the explosive oxygen-burning, a large amount of **K** is formed, yet there is a contribution from the s-process in the formation of K (see section 2.2.3 for details of s-process) (Woosley & Weaver 1995; Clayton 2003).

Silicon Burning As the last burning-stage, the silicon burning captures an $\alpha/{}^4$He-particle, and builds the heavier elements until SNe II-event.

$$^{28}\mathrm{Si} +^{4}\mathrm{He} \rightarrow^{32}\mathrm{S} \tag{2.8}$$

$$^{32}\mathrm{S} +^{4}\mathrm{He} \rightarrow^{36}\mathrm{Ar} \tag{2.9}$$

$$^{36}\mathrm{Ar} +^{4}\mathrm{He} \rightarrow^{40}\mathrm{Ca} \tag{2.10}$$

$$^{40}\mathrm{Ca} +^{4}\mathrm{He} \rightarrow^{44}\mathrm{Ti} \tag{2.11}$$

$$^{44}\mathrm{Ti} +^{4}\mathrm{He} \rightarrow^{48}\mathrm{Cr} \tag{2.12}$$

Ca is formed during oxygen burning, with a quasi-equilibrium state between ^{36}Ar and ^{40}Ca through thermal ejection and capture of an α-particle. When temperatures remain constant in Si-nuclei, statistical equilibrium demands a transmutation of Si into **Ni**. The primary production channel of Ni is through the decay of Fe (see section 2.2.2 for more details).

During the explosive silicon burning, **Ti** is produced with a contribution from SNe Ia (Woosley & Weaver 1995). The Ti formed during the silicon burning can capture an α-particle and have a minor contribution to the **Cr**-abundance.

When a massive star dies, the shock-wave causes high temperatures, with temperatures high enough to break nuclei into α-particles. The ejected material cools down rapidly, reassembling the broken nuclei, but not all reassemble, thus creating an abundance of α-particles. This abundance of α-particles caused by the core-collapse is the alpha-rich freeze-out (Jordan et al. 2003).

2.2.2 Iron Peak Elements

In this thesis, the focus of iron-peak-elements reaction are of vanadium, chromium, manganese, cobalt and nickel, see section 2.1 and highlighted below. The iron-peak elements is a group named due to the abundance measurements of elements in the Solar System, see figure 2.4. The abundance of Fe is high in the Solar System although there is a decrease in abundance with higher atomic number. Around the peak of Fe, the elements, known as the **iron-peak**, are Ti, V, Cr, Mn, Co and Ni. In this thesis, although Ti is one of the peaks, it is treated as an α-element. Despite being treated in the same group in this thesis, the iron-peak elements might have different formation channels.

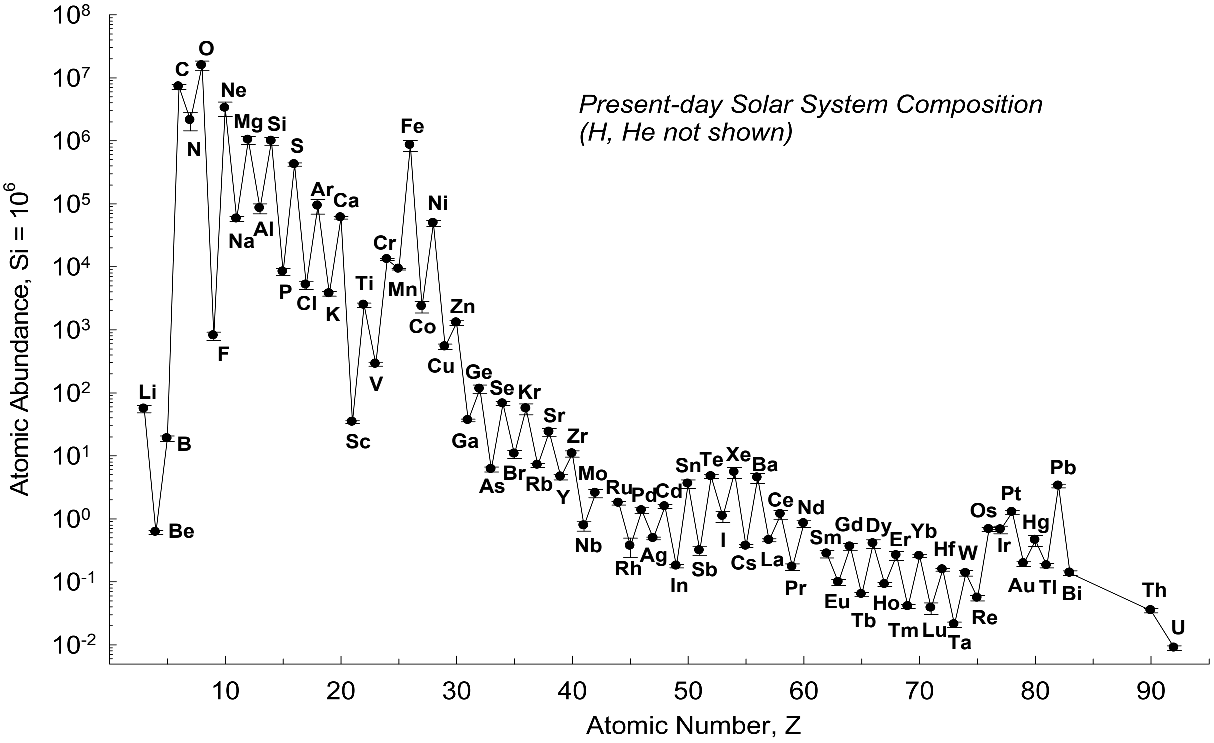

Figure 2.4: The figure shows the elemental abundances in the solar systems normalised to Si-abundance of 10^6, with a peak around Fe. Around this peak are V, Cr, Mn, Co and Ni, identified as iron-peak elements in this thesis. The figure is adopted from Lodders (2010).

Vanadium V-isotopes are produced during explosive oxygen and neon burning. The stable V-isotope is mainly produced during explosive oxygen and silicon burning, with SNe Ia being the main contribution to the abundance in the cosmos (Woosley & Weaver 1995; Clayton 2003).

Chromium Cr is mainly produced during oxygen and silicon burning in massive stars (Woosley & Weaver 1995). The more abundant isotope, ^{52}Cr, is produced primarily during silicon burning, where radioactive Fe decays to Mn and furthermore to Cr (Clayton 2003), with the ejection of Cr through SNe I and SNe II being comparable, despite SNe II occurring 5 times more frequent than SNe I (Clayton 2003).

Manganese Mn has one isotope produced during explosive silicon burning and with ^{55}Ca through nuclear statistical equilibrium (Woosley & Weaver 1995), with some contribution from SNe I (Bravo & Martínez-Pinedo 2012). This element was not analyzed in this work.

Cobalt The only stable isotope, ^{59}Co, is produced during silicon burning and during the alpha-rich freeze-out, as well as with s-process during helium burning in massive stars (Clayton 2003; Woosley & Weaver 1995). A contribution of the Co-abundance is due to

SNe I (Bravo & Martínez-Pinedo 2012), where Fe is also produced (Clayton 2003). For the higher masses, Grimmett et al. (2019) suggested a contribution of hypernovae at higher [Fe/H].

Nickel Ni is mainly a product of the alpha-rich freeze-out and neutron capture during helium burning (Woosley & Weaver 1995), where Fe decays to Ni (Clayton 2003). The contribution of abundances are due to SNe I and II, where a larger fraction is due to the SNe I (Clayton 2003).

2.2.3 Neutron Capture Elements

In this thesis, the focus of neutron-capture elements are copper, germanium, rubidium, cerium, neodymium and ytterbium, see section 2.1. The production channels vary with different contribution of different formation sites.

For the heavier elements, Burbidge et al. (1957) first introduced the term neutron-capture elements, where the elements are synthesized by capturing a neutron. For the endothermic production of the heavier elements, the environment to produce these do not need to be of a high temperature, but needs to have a high density of free neutrons. The pre-existing elements grow by capturing neutrons in its nuclei, and creates a stable isotope or the obtained neutron decays to a proton:

$$\mathrm{n} \rightarrow \mathrm{p} + \mathrm{e}^- + \bar{\nu} \tag{2.13}$$

The element grow by capturing neutrons until an unstable isotope is reached, and through β^--decay a proton will change the element. The growth of isotope-stability is visualized in the valley of stability (see figure 2.5, where the elements marked in black show stable isotopes and the elements marked in light blue show the growth-area through β^--decay). Neutron-capture process can be divided into two processes, as *slow* (s-) and *rapid* (r-) process, introduced by Burbidge et al. (1957). The timescales of slow and rapid indicate the rate at which a successive capture of a free neutron occur. The s-process elements capture the free neutron, allowing for β^--decay to occur before the next successive neutron capture. This process occurs in environments with densities of $\mathrm{n} \leq 10^{11}$ cm^{-1} (Busso et al. 1999). The r-process captures neutrons rapidly, growing the isotope heavier before β^--decay occurs. This process occurs in densities between $10^{23} \leq \mathrm{n} \leq 10^{28}$ cm^{-1} (Kratz et al. 2007).

s-process

Weak s-process The neutron source for the weak s-process is mainly driven by the reaction originating from Ne (Busso et al. 1999):

$$^{22}\mathrm{Ne} +^{4}\mathrm{He} \rightarrow^{25}\mathrm{Mg} + \mathrm{n} \tag{2.14}$$

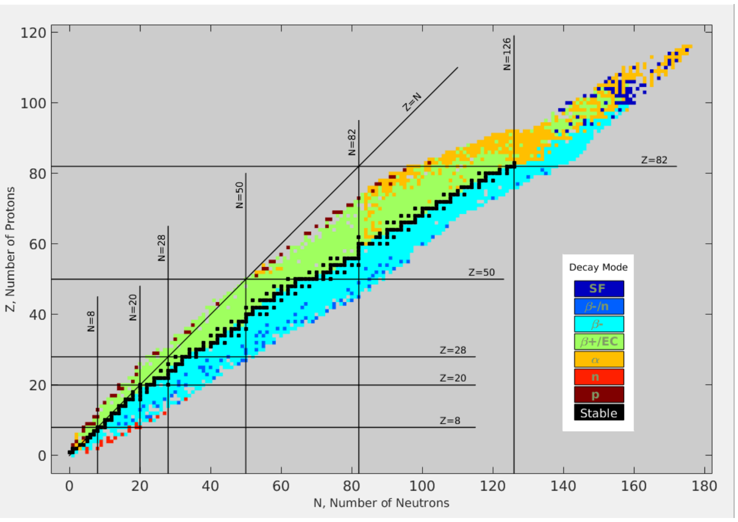

Figure 2.5: The figure shows the valley of stability. The colours indicate the process, that forms the elements, with black indicating the stable isotopes with growing neutrons and protons. Excess of neutrons per proton or vice versa are unstable and decays with respect to the ratio. For lighter elements, the common decays are indicated as light blue for β^- and green for β^+. For the heaviest elements, the common decays become α emission and spontaneous fission. The figure is adopted from `https://en.wikipedia.org/wiki/Valley_of_stability#/media/File:DecayModeNuDat2.png`

Cu is a weak s-process element, produced in the helium shell and during helium burning in massive stars (Woosley & Weaver 1995; Romano & Matteucci 2007). There is a contribution from r-process and the alpha-rich freeze-out, which occur during the explosive burning at lower [Fe/H] (Clayton 2003; Romano & Matteucci 2007). Furthermore, **Ge** and **Rb** are known weak s-process elements, yet these elements are not analyzed, despite attempts, in the thesis.

Main s-process The main s-process nucleosynthesis occur mainly in the lower mass AGB stars, where the neutron flux source is due to the reaction of

$$^{13}\mathrm{C} + ^{4}\mathrm{He} \rightarrow ^{16}\mathrm{O} + \mathrm{n} \tag{2.15}$$

The main s-process elements of interest in this work are **Ce** and **Nd**. Lines are available of the latter but are not useful for an abundance analysis.

r-process

With a high neutron flux, the nuclei can capture a neutron before the decay of previous neutron capture. The *rapid* capture of neutron allows for a fast growth of the isotope, and heavier elements are formed.

The environment in which r-process elements are formed is currently debated heavily. The most likely sites are extreme environments, such as neutron star mergers, but also the traditional channel of massive stars (Siegel et al. 2019). A recent paper by Watson et al. (2019) observed kilonovae environments as a production site for neutron capture elements. Watson et al. (2019) identifiied the r-process element, strontium, with the detailed spectrum of the kilonova, AT2017gfo. The r-process element of interest in this work is **Yb**. Unfortunately, this element was attempted but not analyzed in this work due to the one line available being blended.

Chapter 3

Stellar Sample

In this chapter, the stellar sample, a sub-sample of APOGEE giants bench-marked with optical measurements, are described. The APOGEE spectra have a resolving power of R $\sim$ 22 500 with a high signal-to-noise ratio of above 100. The stellar sample consists of 263 giants, some with several spectra, with the sample having median distance of $\sim$ 400 pc.

3.1 Stellar Sample

In this section, the stellar sample investigated and the source of its properties are described. A summary of the stellar sample can be seen in table 3.1. The stellar sample consists of 263 K-giants, bench-marked with high quality optical measurements by Jönnson et al. (in prep.) using the FIES spectrograph in the Nordic Optical Telescope.

The spectra were observed using the *Apache Point Observatory Galactic Evolution Experiment* (APOGEE), an on-going survey of the Milky Way as part of the Sloan Digital Sky Survey (SDSS). The main targets of APOGEE are Red Giant Branch (RGB), red clump (RC) and asymptotic giant branch stars (AGB) (Zasowski et al. 2013). The APOGEE instrument observes 300 stars simultaneously with a high resolving power of R $\sim 22,500$, and the main purpose of the survey is constraining the chemical evolution of the Milky Way with a minimally biased sample. Of the 300 simultaneous measurements, $\sim$ 70 fibres are used to measure telluric lines for calibration purposes with the remaining measurements obtaining measurements for scientific purposes (Zasowski et al. 2013).

The distances for some of the 263 stars in the sample, investigated in this thesis, can be found in the work by McMillan (2018), using radial velocity measurements to estimate the distances, and Gaia DR2 (Gaia Collaboration et al. 2018), using the inverse parallax to estimate the distances. They are within 4 kpc, with the majority of the stars to be within 2 kpc. A histogram of the stellar sample distances can be seen in figure 3.1 using

Number of Measurements	291 (+ Solar spectrum)
Number of Stars	263
Wavelength Region	15000 - 17000 Å
Resolving power	22,500
Telescope	Apache Point Observatory & Las Campanas Observatory
S/N	100 - 1700 (median ∼ 340)
Distance	47 - 4890 pc (median ∼ 420 pc) (McMillan 2018)

Table 3.1: The table shows a summary of the stellar sample.

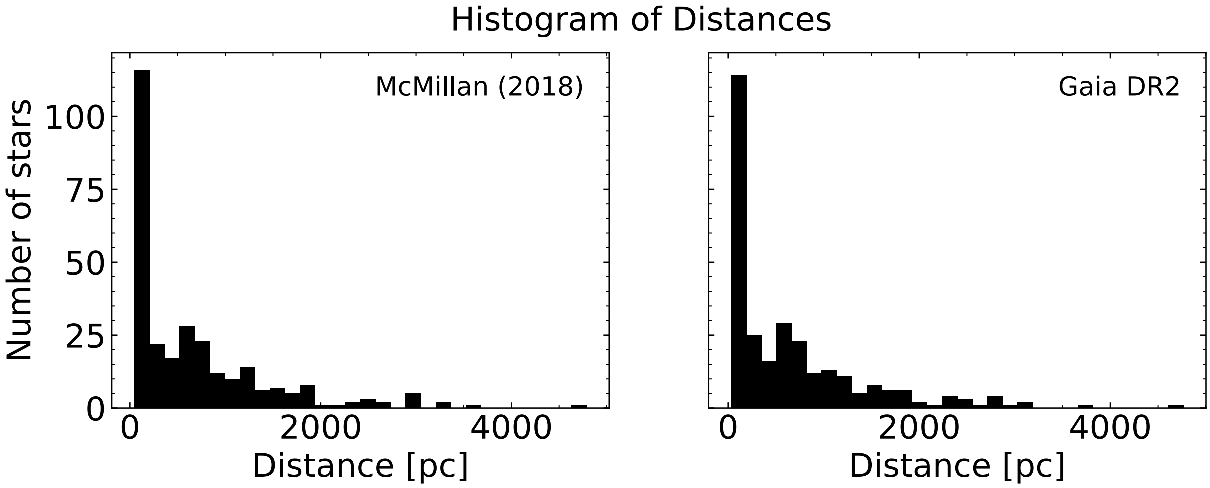

Figure 3.1: The histogram on the left shows the distances of the stellar sample in 30 bins measured by McMillan (2018), using radial velocity measurements. The median of the stellar sample is 417 pc. On the right are the distances of the stellar sample in 30 bins measured by Gaia Collaboration et al. (2018), estimating distances using the inverse parallax. The median of the stellar sample is 416 pc.

distances from McMillan (2018) and Gaia DR2 (Gaia Collaboration et al. 2018).

The wavelength coverage of APOGEE is in the H-band, between 15000 Å and 17000 Å, and due to the lower extinction at these wavelengths, enables dust penetration thus enabling observation of stars in the dusty galactic plane. The signal-to-noise ratio has a median of S/N $\sim$ 340 (S/N $\sim$ 100-1700). Using the APO-1-meter telescope, the signal-to-noise ratio is overall less than using APO-2.5-meter in this sample. This can be seen in figure 3.2.

The 263 stars in this sample have been bench-marked with optical measurements. The galactic positions of the sample can be seen in figure 3.3 with Gaia DR2 (Gaia Collaboration et al. 2018) measurements of right ascension and declination with [Fe/H]-measurements by Jönsson et al. (2017).

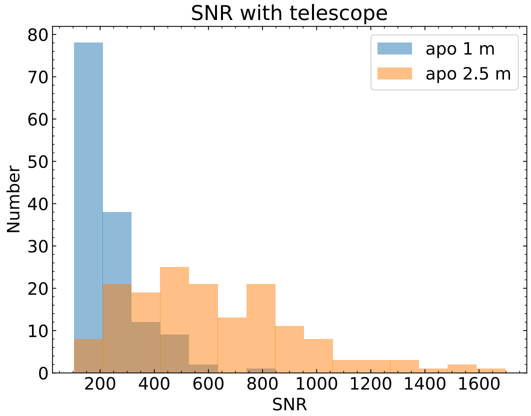

Figure 3.2: The figure shows a histogram of the signal-to-noise ratio using the APO 1-m telescope and APO 2.5-m telescope in 20 bins.

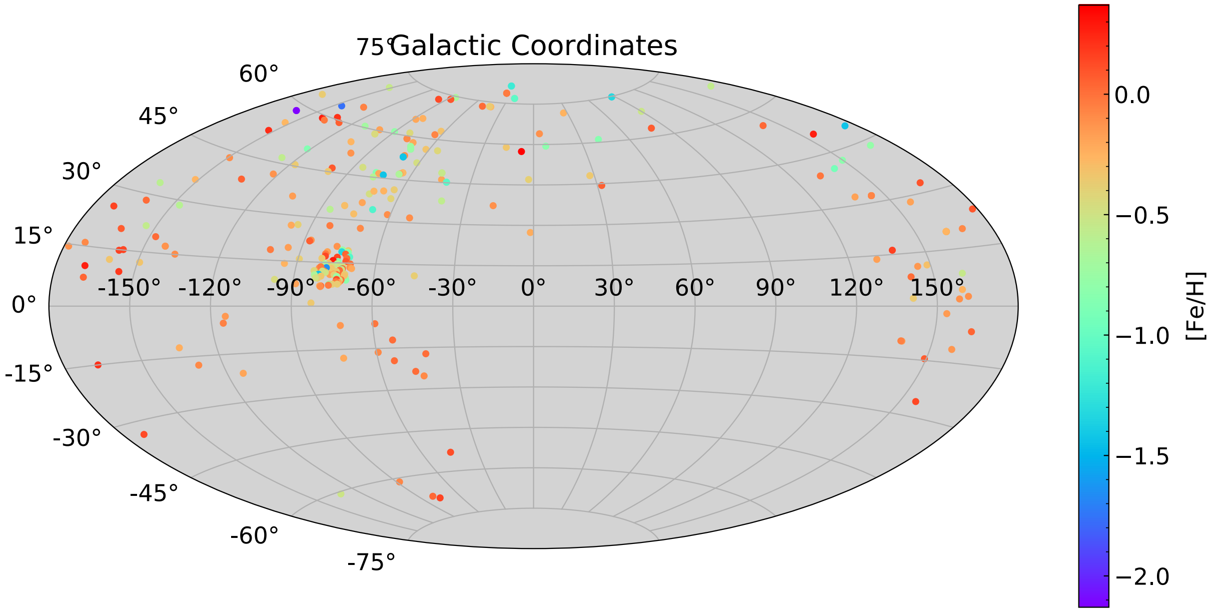

Figure 3.3: The figure shows the galactic coordinates of the stellar sample with varying metallicity, [Fe/H]. APOGEE is both in the northern and southern hemisphere, and the stellar sample is bench-marked with optical measurements by FIES in La Palma, which is in the northern hemisphere. The grouping at $l \sim -75°$ is the Kepler field.

APOGEE releases reduced spectra continuously, with data releases showing intermediate results of the abundances of each element of interest, and possibly results that could be improved for later data releases, as well as releasing stellar parameters and abundance measurements using *APOGEE Stellar Parameters and Chemical Abundances Pipeline* (ASPCAP), described in section 4.6. In this work, the stellar parameters and chemical abundances are measured independently of these measurements, described in section 4.4.

Chapter 4

Methodology

In this chapter, the method of abundance measurements is discussed. In order to measure the abundances, accurate model atmospheres are needed defined by the stellar parameters. The stellar parameters, as well as the model atmospheres, are important when synthesizing spectra, where accurate atomic data for each line of interest, are also required. $v_{\rm rad}$ and $v_{\rm mac}$ are constrained by different methods, aimed to best fit the observed spectra here obtained using APOGEE. The abundance measurements are done using *Spectroscopy Made Easy*, synthesizing spectra with χ^2-minimization.

Two well-known methods for determining abundances from spectra are using the equivalent width (EW), which is a measure of the area equivalent to the integrated absorption line, and synthesizing a spectrum, which uses statistical methods to recreate observations. The lower temperatures of giant stars mean that molecules exist and these have lots of lines in the spectra. Thus for the purpose of determining abundances in giants, spectral synthesis-method is the only method to use, in order to take care of the blends and lines broadening.

The code for spectral synthesis, I have chosen, is the well tested Spectroscopy Made Easy (SME) (Valenti & Piskunov 1996; Piskunov & Valenti 2017), which uses MARCS model atmospheres that are aimed for giant stars. This is an easy-to-use code, that measures on observational spectra using χ^2-minimization of synthesized spectra. In the following, I will describe determining stellar parameters such as the effective temperature, $T_{\rm eff}$, surface gravity, $\log g$, microturbulence, $v_{\rm mic}$, and metallicity, [Fe/H], although these are not determined in this work. Furthermore, the method of determining the abundance is by synthesizing a spectral line and the improvements of the linelist is described. The chapter ends with a description of determining the uncertainties of the abundance measurements and a description of the abundance measurements by APOGEE.

4.1 Model Atmosphere

The model atmosphere used in this thesis is the MARCS atmospheric model (Gustafsson et al. 2008). SME has integrated grids of these atmospheres, which assumes 1D-local thermodynamic equilibrium (LTE), spherically symmetric atmospheres in hydrostatic equilibrium. These four main assumptions account for how the line is formed due to the temperature and the pressure structures of the star of interest.

The MARCS grids are in **hydrostatic equilibrium**, which assumes that the inward gravity is equal to the outward pressure, thus preventing the star from collapsing or expanding. This assumption also provides that the gas motion in the photosphere is rather constant over time, which is an adequate assumption.

The model atmosphere is assumed to be **one-dimensional**, which means that the upper layer temperature structures are due to radiative cooling and heating.

The **spherically symmetric** assumption account for the large photosphere of giant stars. For dwarfs, the plane-parallel structure of the photosphere is adequate.

4.2 Stellar Parameters

The stellar parameters are also determined using SME. The stellar parameters are determined using optical measurements of the stellar sample used in this thesis (Jönsson et al. 2017). The stellar parameters are globally determined for the entire sample, where α Boo and μ Leo, with well-constrained stellar parameters, are used as benchmarks. The stellar parameters, with the abundances for Mg and Si (large electron donors), are free parameters.

Effective Temperature T_{eff} is determined using the several Fe I lines as each line gives the same abundance. NLTE corrections are added for the lines from Lind et al. (2012).

Surface Gravity $\log g$ is determined using the relation of the different ionisation levels, assuming the abundance is the same. In this thesis, the relation between Fe I and Fe II are used. The $\log g$ can also be determined using the wings of strong lines with strong wing-features.

Metallicity [Fe/H] is determined simultaneously as the effective temperature and the $\log g$.

Micro Turbulence v_{mic} is determined using strong and weak lines by requiring the abundances of these are the same.

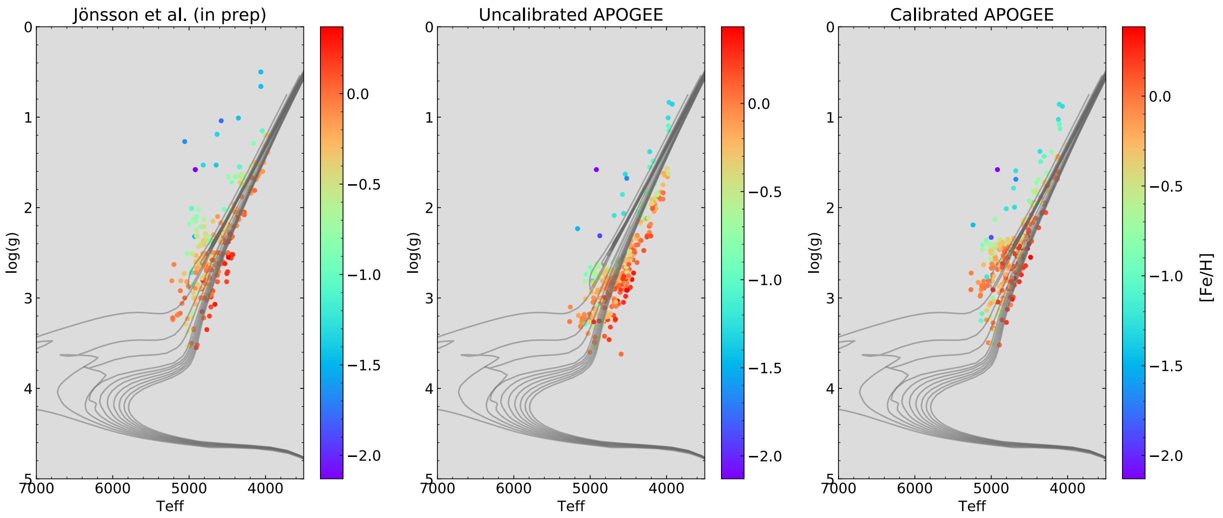

Figure 4.1: The figure shows Kiel diagrams of the 291 measurements of 263 K-giants with the stellar parameters, $\log g$ and T_{eff}, with varying metallicity, [Fe/H], measured by Jönsson et al. (in prep.), uncalibrated and calibrated APOGEE. The isochrones show stellar tracks of stars with different masses and ages.

Kiel-diagrams of the stellar sample used in this thesis can be seen in figure 4.1 with stellar parameters by optical measurements and APOGEE DR16 uncalibrated and calibrated, respectively. The manually determined stellar parameters by Jönsson et al. (in prep.) follow the isochrones nicely, showing the accuracy of the parameters. This suggest that the stellar parameters are better in this sense than the stellar parameters determined by ASPCAP, described in section 4.6. In section 6, the stellar parameters are discussed further, comparing abundance measurements using the stellar parameters presented in figure 4.1. The abundance measurements depend on well-constrained stellar parameters, thus accuracy and precision in these are important.

4.3 Constraining v_{mac} and v_{rad}

Other than the four main stellar parameters, the v_{mac} and v_{rad} are needed to be constrained using the spectral synthesis method (section 4.4). SME deals with the thermal and pressure broadening, and in order to fully constrain the line-profile, it is needed to incorporate the velocity fields of large motions, v_{mac}, which is global for all lines, since the abundance measurements later are provided by the line depths. Two methods in constraining these parameters are investigated: the **vmac-Si**-method and the **detour method**. The method which agrees with the bench-marked optical measurements best is considered the better method of constraining v_{mac} and v_{rad} as well as the Si-abundances.

The **vmac-Si method** is where Si-abundance is determined while simultaneously constraining the radial velocity, v_{rad}, and the macroturbulence, v_{mac}. The Si-lines used for this are the first three Si-lines in table 4.1, which show gaussian-profiles in metal-poor spectra. As each trend of these Si-lines show agreement with the optical measurements, the lines are kept for abundance measurements.

The **"detour"-method** is the method where only the v_{rad} and v_{mac} are constrained. Using SME, these are set as free parameters including Si. The Si-abundance, v_{rad} and v_{mac} are determined using the lines that showing gaussian profiles in the metal-poor spectra. The center and broadening of the fit determine these parameters of interest. Stronger gaussian-profiles better constrain these parameters, thus includes the constraints in v_{rad} and v_{mac} for the entire sample of this work. The lines used in this method are the last 5 Si-lines in table 4.1, where the Si-abundance obtained with this method are not the final abundances, but due to their gaussian-profiles in metal-poor spectra.

Element	Wavelength [Å]	log(gf)	E$_{low}$	E$_{up}$	Reference
Si I	16163.71	-0.862	5.9537	6.7206	Kurucz (2007)
Si I	16241.85	-0.770	5.9639	6.7271	Kurucz (2007)
Si I	16380.14	-0.465	5.8625	6.6192	Kurucz (2007)
Si I	15884.45	-0.826	5.9537	6.7341	Kurucz (2007)
Si I	16094.80	-0.105	5.9639	6.7341	Kurucz (2007) (gf: Pehlivan Rhodin et al. (2017))
Si I	16163.71	-0.862	5.9537	6.7206	Kurucz (2007)
Si I	16215.69	-0.631	5.9537	6.7181	Kurucz (2007)
Si I	16828.18	-1.028	5.9840	6.7206	Kurucz (2007)

Table 4.1: The table shows the Si-lines used to determine the v_{rad} and v_{mac} with the corresponding wavelength, line strength, lower and upper excitation energies. The first three Si-lines are the lines used in the **vmac-Si**-method and the lower five Si-lines are used in the **detour**-method.

In order to well-constrain these parameters, SME runs three times with these v_{mac}, v_{rad} and Si as free parameters. This is done three times due to v_{rad} becoming 0 after the third run, i.e. SME has stopped improving this value.

The v_{mac} and v_{rad} are constrained with respect to the width of the line and the center of dip, respectively, and considered when checking the quality of the fits. This is the important manual part of the thesis, as the quality of fits are not checked in the automatic systems.

A comparison of the determined Si-abundance of each method can be seen in figure 4.2. Although both abundance determination are using the same lines and exhibit the same scatter, the detour method agrees best with the optical measurements better than the vmac-Si-method, where the black Si-abundance trend in figure 4.2 shows to go through the solar Si-abundance at solar metallicity. A lower mean difference and standard deviation from the optical measurements show better agreement, and are taken as the more precise and accurate determination of Si-abundance. The final method in constraining v_{mac} and v_{rad} is using the **detour-method**:

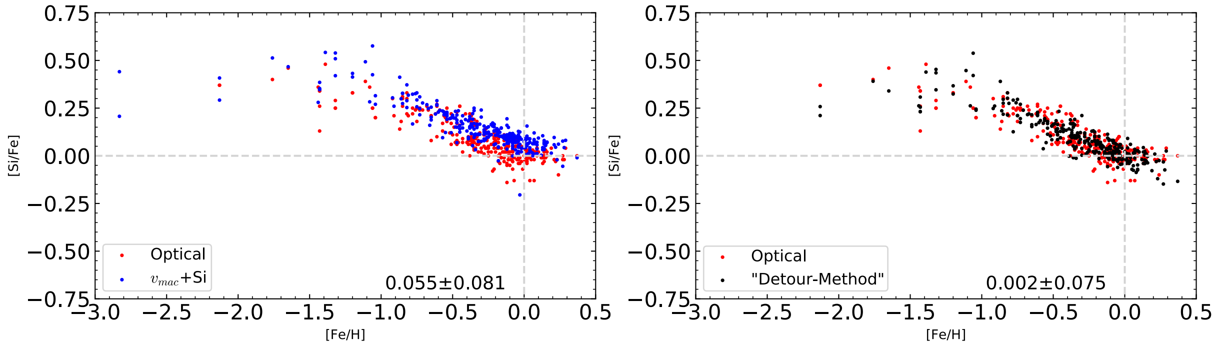

Figure 4.2: The Si-abundance trend comparisons to the optical Si abundance of the two methods of constraining v_{mac} and v_{rad}. The left comparison show the Si-abundance constrained simultaneously as v_{mac} using three Si-lines (blue). The right comparison show the Si-abundance using three lines after the v_{mac} has been constrained using five Si-lines (black). The optical Si-abundance are marked as red. Each red dot has a corresponding blue/black dot for the same star and hence lies at the same [Fe/H].

- Use the (last) five Si-lines in table 4.1
- Set Si, v_{mac} and v_{rad} as free parameters
- Re-run three times (until v_{rad} is fully constrained)
- Si-abundance is then determined in the same way as all other elements

4.4 Synthesis of Spectral Line

Using SME, the abundance is determined using an appropriate model atmosphere, described in section 4.1, using the stellar parameters determined for each star, described in section 4.2. The χ^2-minimization works with the width and the λ-shift of the line, thus the method described in section 4.3 is important for accurate abundance measurements.

In order to accurately synthesize a spectrum, a complete linelist is needed within the wavelength region. As well as having the complete species within the region, the atomic data is needed in order to synthesize the spectrum accurately. The improvement of these are described in section 4.4.1. For a weak line, to determine the abundance, the following equation for equivalent width need to be taken into account:

$$\log\left(\frac{W}{\lambda}\right) = \log(C) + \log(A) + \log(gf\lambda) - \theta_{ex}\chi - \log(\kappa_c), \tag{4.1}$$

where C is a constant, A is the abundance, $\log(gf)$ is the line strength, λ is the wavelength of the line, θ_{ex} is the excitation temperature, χ is the excitation potential and κ_c is the continuum opacity. In figure 4.3, (1) indicates where the weak line approximation holds.

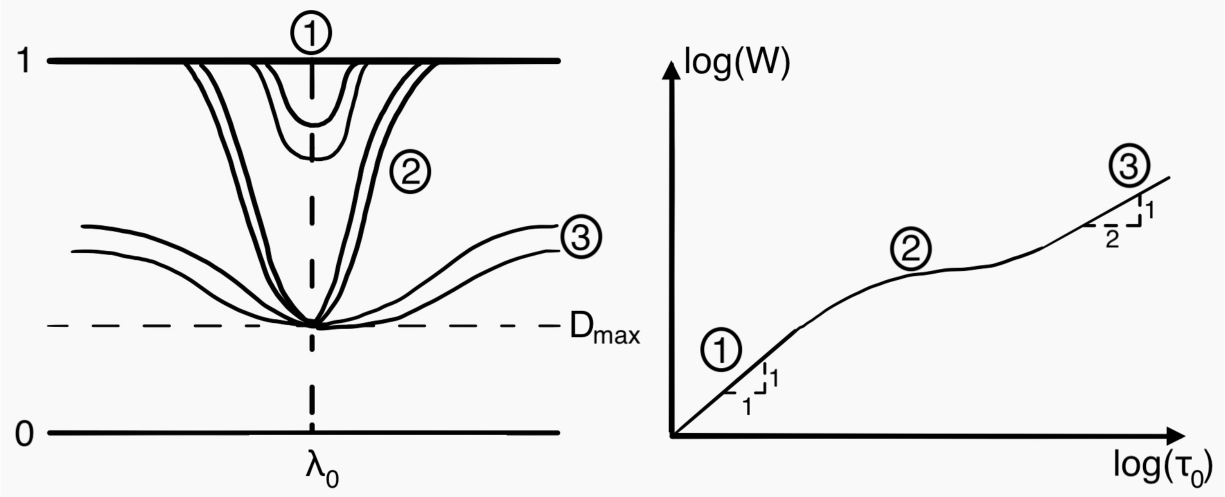

Figure 4.3: The figure shows the curve of growth and the corresponding line profile. The weak line (1) approximation holds, where the line becomes saturated (2) for higher abundances. For the strongest lines (3), winds develop and the line profile gets damped. D$_{max}$ shows the maximum depression of a strong line.

One of the important atomic data is the line strength, log(gf). This parameter is dependent on the Einstein coefficient, A_{21}, of a line, as:

$$A_{21} = \frac{2\pi\nu^2 \mathrm{e}^2}{\epsilon_0 m_e c^3}\frac{g_l}{g_u} f_{12}, \tag{4.2}$$

where ν is the frequency, e is the electron charge, ϵ_0 is the vacuum permittivity, c is the speed of light, m_e the electron mass, and g_u is the statistical weight of the upper level and $g_1 f_{12}$ is the oscillator strength.

A few assumptions to synthesize a spectrum are made which are described here:
The **local thermodynamic equilibrium** (LTE) assumes the levels are distributed collisionally. LTE assumes that the distribution of levels in atoms, ions and molecule follows a Boltzmann distribution. The velocity of the gas is described following the Maxwellian distribution:

$$\left[\frac{n(v_x)}{N}\mathrm{d}v_x\right]_{LTE} = \sqrt{\frac{m}{2\pi kT}}\exp\left(-\frac{mv_x^2/2}{kT}\right)\mathrm{d}v_x \tag{4.3}$$

with v_x as the velocity in x, N the number of levels, m as the particle mass, k the boltzmann constant, and T as the temperature. The excitation levels are distributed following the Boltzmann distribution:

$$\frac{n_i}{n_u} = \frac{g_i}{g_u}\exp\left(-\frac{\chi_i - \chi_u}{kT}\right) \tag{4.4}$$

with n_i is the number population of the ionized state, n_u the number density of unionized state, g_u and g_l being the upper and lower statistical weights, respectively, and χ_u and

χ_l being the upper and lower energies, respectively. The ionization levels are distributed following the Saha equation:

$$\left[\frac{N_{r+1}}{N_r}\right]_{LTE} = \frac{1}{N_e}\frac{2U_{r+1}}{U_r}\left(\frac{2\pi m_e kT}{h^2}\right)^{3/2} \exp\left(-\frac{\chi_l}{kT}\right) \tag{4.5}$$

with N_r and N_{r+1} being the lower and upper level number density, respectively, N_e being the electron number density, U_r and U_{r+1} being the partition functions for the lower and upper level, respectively, m_e the electron-mass, h the planck constant and χ_l the lower energy level.

Another important step aside from constraining stellar parameters and atomic data accurately, is determining the contrast between the continuum and line depth; another *manual* part of the thesis. Figure 4.4 shows two figures of spectra with lines of abundance interest with figure 4.4a showing a line of interest with good continuum regions as well as a good line. Figure 4.4b shows a line of interest on the wing of another element, and although the continuum masks are clear, the line cannot accurately be used to constrain the abundance due to blending of the lines (CO). The continuum masks are chosen as small segments, where SME linearly fits the continuum regions as the base-level. This is important as the abundance measurements are dependent on the line depth.
The elemental abundances are measured compared to the solar number density values as:

$$[\mathrm{X/Y}] = \log_{10}\left(\frac{n_\mathrm{X}}{n_\mathrm{Y}}\right)_\star - \log_{10}\left(\frac{n_\mathrm{X}}{n_\mathrm{Y}}\right)_\odot . \tag{4.6}$$

where n_X and n_Y are number densities of element X and Y, of the star of interest and the solar values. The number density values from Grevesse et al. (2007) are used as solar density, which can be seen in table 4.2.

When using SME (Valenti & Piskunov 1996; Piskunov & Valenti 2017), the following inputs are required in order to synthesize a spectral line using SME:

- Observed stellar spectra (reduced)
- Line list containing atomic and molecular data. This contains the name of the element, wavelength of transition, the line strength ($\log(gf)$), upper and lower energy and dampening effects, e.g. radiative, Stark and Van der Waals dampening.
- Spectral regions for:
  - **Segment** interval around a line of interest. These segment are ~ 20-30 Å in this work.
  - **Continuum** mask defines the zero-level used to determine the line depth. The continuum masks are within the segment interval.
  - **Line** mask defines the wavelength interval of where the line of interest is within. These intervals are within the segments and are ~ 1 Å.

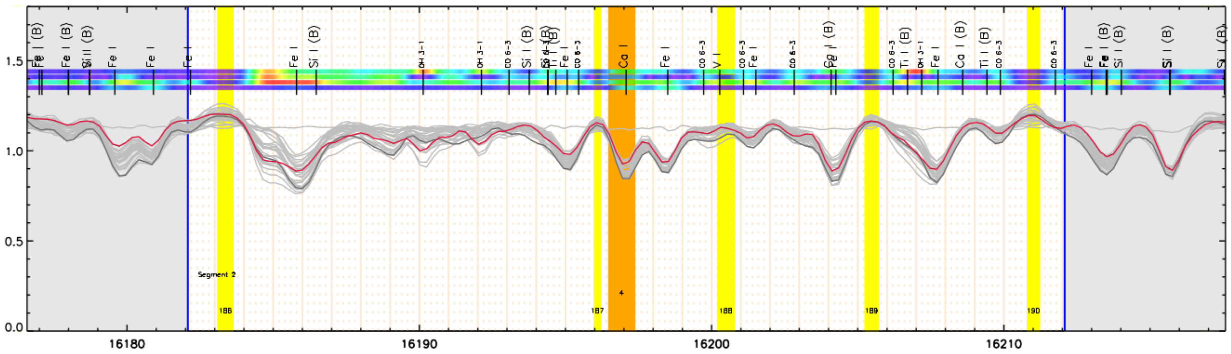

(a) The figure shows spectra of 50 stars of the ones used in this thesis, with α Boo and μ Leo (metal-rich stars) spectra as red and dark grey, respectively. The orange area shows the line mask with the yellow areas showing chosen continuum masks. The line of interest in this figure is Ca I to show a good line for abundance measurements using SME.

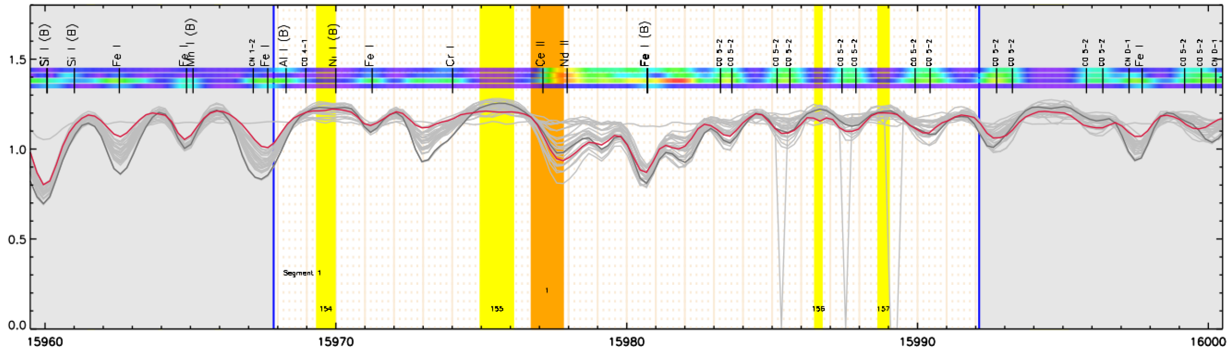

(b) The figure shows spectra of 50 stars, with α Boo and μ Leo spectra as red and dark grey, respectively. The orange area shows the line mask with the yellow areas showing chosen continuum masks. The line of interest in this figure is Ce II to show a bad line for abundance measurements as it is on the wings of a CO-line. The CO band-head prevents accurate abundance measurements.

Figure 4.4: Figures of masking lines of interest in abundance measurements using SME.

- A grid model of MARCS model atmospheres is used by SME. The MARCS atmospheric models (Gustafsson et al. 2008) assumes 1D hydrostatic, spherical symmetry and LTE, described in section 4.1.

- The stellar parameters are determined previously using high resolution optical measurements. As mentioned before, the parameters are effective temperature (T_{eff}), metallicity ([Fe/H]), velocities (v_{mic}, v_{mac} and v_{rad}) and surface gravity ($\log g$). In order to determine the abundances [X/Fe], these parameters are fixed. How these fixed parameters are determined is described in section 4.2.

In table 4.3 are the lines of interest of all elements, provided with wavelength, oscillator strength and lower energy. The atomic data are provided by the *Vienna Atomic Line Database* (VALD) (Ryabchikova et al. 2015) linelist and the oscillator strengths are provided by available laboratory measurements, described in 4.4.1. The linelist is updated

Elem.	n_x	Elem.	n_x	Elem.	n_x	Elem.	n_x	Elem.	n_x
H	12.00	P	5.36	Cu	4.21	Ag	0.94	Tb	0.28
He	10.93	S	7.14	Zn	4.60	Cd	1.77	Dy	1.14
Li	1.05	Cl	5.50	Ga	2.88	In	1.60	Ho	0.51
Be	1.38	Ar	6.18	Ge	3.58	Sn	2.00	Er	0.93
B	2.70	K	5.08	Kr	3.25	Sb	1.00	Tm	0.00
C	8.39	Ca	6.31	Rb	2.60	Xe	2.24	Yb	1.08
N	7.78	Sc	3.17	Sr	2.92	Ba	2.17	Lu	0.06
O	8.66	Ti	4.90	Y	2.21	La	1.13	Hf	0.88
F	4.56	V	4.00	Zr	2.58	Ce	1.70	W	1.11
Ne	7.84	Cr	5.64	Nb	1.42	Pr	0.58	Os	1.25
Na	6.17	Mn	5.39	Mo	1.92	Nd	1.45	Ir	1.38
Mg	7.53	Fe	7.45	Ru	1.84	Sm	1.00	Au	1.01
Al	6.37	Co	4.92	Rh	1.12	Eu	0.52	Tl	0.90
Si	7.51	Ni	6.23	Pd	1.66	Gd	1.11	Pb	2.00

Table 4.2: The table shows the solar abundances by Grevesse et al. (2007), which are the solar values used in *Spectroscopy Made Easy*.

with the lines used for abundance measurements with references in section 5.2. It should be noted that a later version of SME takes NLTE-effects into account, explained further in section 4.4.2. NLTE effects are included in determining the stellar parameters and aluminium-abundances.

4.4.1 Correction of Oscillator Strength

In order to accurately measure abundances by synthesizing lines, precise atomic data must be accurately known. The linelist used here is VALD. The VALD-linelist uses several different sources of measurements, calculations and/or estimates.

The oscillator strength can be measured in the laboratory or as astrophysical oscillator strength. The astrophysical oscillator strengths are determined using bench-mark stars with high resolution, e.g. the Sun. Following the weak line approximation, described in section 4.4, knowing the abundance can constrain the oscillator strength, gf. Constraining the oscillator strength using the Sun's spectrum assumes that the each elemental abundance of the Sun are well-constrained, but if the abundance(s) is (are) wrong, the gf-values are wrong. This is the best we can do.

Although it would be ideal to have laboratory $\log(gf)$-measurement, for accurate and precise measurements, measuring the oscillator strength with this method is complicated. Thus, for some oscillator strength, it is reasonable to resort to the astrophysical oscillator strength.

Elem.	λ [Å]	log(gf)	E$_{low}$ [eV]	Elem.	λ [Å]	log(gf)	E$_{low}$ [eV]	Elem.	λ [Å]	log(gf)	E$_{low}$ [eV]
Al 1	16718.97	-0.148	4.0853	Na 1	16373.87	-1.328	3.7526	P 1	15711.52	-0.51	7.1758
Al 1	16750.6	-0.404	4.0872	Na 1	16388.85	-1.027	3.7533	P 1	16254.75	0.0	8.2255
Al 1	16763.37	-0.514	4.0872	Nd 2	15284.46	-2.13	0.6804	P 1	16482.93	-0.29	7.2127
Ca 1	16136.82	-0.363	4.5313	Nd 2	15368.14	-1.55	1.264	Rb 1	15289.48	0.42	1.589
Ca 1	16150.76	-0.032	4.5322	Nd 2	15912.29	-2.39	0.5502	S 1	15403.77	0.73	8.6995
Ca 1	16155.24	-0.496	4.5322	Nd 2	15977.95	-2.47	1.1212	S 1	15469.82	-0.05	8.0452
Ca 1	16157.36	0.246	4.5541	Nd 2	16053.63	-2.2	0.7446	S 1	15475.62	-0.52	8.0455
Ca 1	16197.08	0.254	4.5347	Nd 2	16262.04	-1.99	0.9857	S 1	15478.48	0.18	8.0457
Ca 2	16561.06	0.389	9.235	Nd 2	16303.78	-2.11	0.8594	S 1	16590.96	-0.76	8.4167
Ce 2	15277.65	-1.94	0.6088	Nd 2	16382.92	-1.48	1.5448	S 1	16593.2	-0.56	8.4173
Ce 2	15784.75	-1.54	0.3178	Nd 2	16558.21	-2.4	0.9329	Si 1	15376.89	-0.973	6.2227
Ce 2	15958.4	-1.71	0.4703	Nd 2	16634.67	-2.37	1.1365	Si 1	15557.79	-0.81	5.9639
Ce 2	15977.12	-2.1	0.2323	Ni 2	15170.06	-2.36	15.7732	Si 1	15884.47	-0.826	5.9537
Ce 2	16327.32	-2.4	0.5608	Ni 2	15173.58	-0.547	5.4879	Si 1	15888.44	0.009	5.0823
Ce 2	16376.48	-1.79	0.1224	Ni 2	15195.27	-0.948	5.2825	Si 1	15960.08	0.397	5.984
Ce 2	16595.18	-2.19	0.1224	Ni 2	15199.62	-0.501	5.4692	Si 1	16060.02	-0.484	5.9537
Ce 2	16722.51	-1.65	0.4704	Ni 2	15290.72	-0.889	5.3053	Si 1	16094.8	-0.105	5.9639
Co 1	16757.64	-0.923	3.4092	Ni 2	15555.38	0.218	5.4879	Si 1	16163.71	-0.862	5.9537
Cr 1	15680.06	0.152	4.6969	Ni 2	15605.66	0.017	5.3053	Si 1	16215.69	-0.631	5.9537
Cr 1	15860.21	0.021	4.6969	Ni 1	15632.62	0.125	5.3053	Si 1	16241.85	-0.77	5.9639
Cr 1	15974.01	-2.291	5.9783	Ni 1	15753.61	-0.602	5.4692	Si 1	16380.14	-0.465	5.8625
Cr 1	16015.32	-0.21	4.6969	Ni 1	16136.1	-0.003	5.4879	Si 1	16381.55	-0.951	5.9639
Cu 1	16005.54	-0.045	5.3483	Ni 1	16278.8	-1.585	5.5254	Si 1	16680.77	-0.227	5.984
Cu 1	16006.74	0.255	5.3483	Ni 1	16310.5	0.222	5.2825	Si 1	16828.18	-1.028	5.984
Cu 1	16638.98	0.07	6.1227	Ni 3	16335.62	-9.7	25.3429	Ti 1	15186.7	-2.32	1.8792
Ge 1	16759.76	-0.3	4.9619	Ni 1	16363.09	0.588	5.2825	Ti 1	15334.84	-0.96	1.8871
K 1	15163.09	0.689	2.67	Ni 1	16388.74	-0.253	6.0346	Ti 1	15543.75	-1.08	1.8792
K 1	15168.4	0.48	2.6702	Ni 1	16480.55	-0.81	5.2825	Ti 1	15602.84	-1.435	2.2674
Mg 1	15740.7	-0.223	5.9315	Ni 1	16536.17	-0.156	6.04	Ti 1	15698.98	-2.01	1.8871
Mg 1	15748.99	0.129	5.932	Ni 1	16550.38	0.266	6.2169	Ti 1	15715.57	-1.2	1.8732
Mg 1	15765.84	0.4	5.9328	Ni 1	16584.44	-0.709	5.3053	Ti 2	15873.84	-1.9	3.1235
Mg 1	15879.56	-1.326	5.9459	Ni 1	16589.44	-0.345	5.4692	Ti 1	16330.54	-0.89	3.1081
Mg 1	15886.19	-1.896	5.9459	Ni 1	16673.7	0.388	6.0346	Ti 1	16635.15	-1.582	2.3447
Mg 1	15889.52	-1.876	5.9459	Ni 1	16761.24	-0.307	6.0424	V 1	15567.69	-1.868	4.6228
Mg 1	15948.38	-2.0	6.5879	Ni 1	16815.46	-0.417	5.3053	V 1	15700.61	-0.45	3.2241
Mg 1	15954.45	-1.82	6.5879	Ni 1	16818.74	0.473	6.04	V 1	15924.81	-1.108	2.1377
Mg 1	16595.58	-2.09	6.5161	Ni 1	16867.28	0.115	5.4692	V 1	15939.87	-0.353	3.2387
Mn 1	15159.15	0.619	4.8889	Ni 1	16875.17	-1.772	6.0424	V 1	16200.28	-0.237	4.6498
Mn 1	15217.74	0.52	4.8889	Ni 1	16945.31	-0.765	5.3634	V 1	16570.56	-1.535	2.1145
Mn 1	15262.49	0.393	4.8889	Ni 1	16996.24	0.458	5.3053	Yb 2	16498.4	-0.64	3.0169

Table 4.3: The table shows the lines of interest for abundance measurement of all the elements provided with wavelength, oscillator strength and the lower energy. The oscillator strengths are updated from the VALD-linelist with available laboratory measurements.

The astrophysical oscillator strength is usually measured on the Sun but can be done against often stars or a combination of e.g. the Sun, α Boo and μ Leo (well-measured giant stars). In table A.1, the oscillator strengths of the lines of interest can be seen with used line strength, marked as "Used $\log(gf)$", including the APOGEE DR16 astrophysical $\log(gf)$ (Smith et al. in prep.) which is measured as a combination of the Sun and α Boo, and Gustafsson et al. (2008) astrophysical $\log(gf)$, which are measured on the Sun. The VALD $\log(gf)$ values are updated with available oscillator strength measurements.

4.4.2 NLTE Corrections

Local thermodynamic equilibrium (LTE) is the assumption that the atmosphere's particles are dominated by collisions. To explain inter-atomic and intra-atomic partitioning, the Boltzmann and Saha equations hold. From that the source function is the Planck function. When the partitioning is not governed by the Boltzmann distribution, i.e. radiation needs to be taken into account, the LTE-assumption fails (Bergemann 2014).

Non-LTE is non-linear and non-local, requiring extensive calculations. The LTE-assumption holds in many cases for weak-lines as described in section 4.4, but for stronger lines, the line centers and the broadening of the wings are corrected by a NLTE-correction (Bergemann 2014; Bergemann & Nordlander 2014).

The non-LTE abundance corrections increase as the [Fe/H] decreases. Models predict the severity of abundance-corrections needed for each line breaking the LTE-assumption (Bergemann & Nordlander 2014).

In this thesis, the pre-calculated aluminium NLTE-corrections are applied using SME.

4.4.3 Thin and Thick Disk Separation

The stars in this work have been assigned probabilities of being thin and thick disk by chemistry and kinematics. Further in the thesis, the thin and the thick disk stars are investigated.

The thin and thick disk are separated as the high - and low α-abundance seen in the optical Mg-abundances (Jönsson et al. in prep.). The v_{rad} of these are separated at 70 km s^{-1}, where the mean v_{rad} is below for thin disk stars, and above for thick disk stars. For stars, which populations are not determined chemically, the v_{rad} determines the probability of which population the star belongs to. The s-rich stars are marked as these stars have shown a higher abundance in s-process elements using high resolution optical measurements. Stars with $V_{tot} > 200$ km s^{-1} are most likely halo stars.

	T_{eff}[K]	$\log g$[dex]	[Fe/H][dex]	v_{mic}[km/s]
Jofré et al. (2015)	4286 ±35	1.64 ± 0.06	-0.52 ±0.08	1.58 ± 0.12
This work	4308	1.66	-0.55	1.77

Table 4.4: The table shows the stellar parameters of Arcturus.

4.5 Uncertainty Measurements

There are two main uncertainties in abundance measurements: systematic uncertainties, due to models used in the spectral analysis, and the random uncertainties, due to the freedom of determining the continuum - and line masks which are highly dependent on the S/N (Jönsson et al. 2017a).

4.5.1 Systematic Uncertainties

Systematic differences occur due to the incorrect determination of stellar parameters and atomic data as well as incomplete atmospheric models. It is a challenge to estimate the uncertainties, yet a standard way of estimating these is done using a reference star. The sample in this work consists of K-giants, thus a well-measured giant is used as a reference, Arcturus (spectral type: K2III).

Arcturus, also known as αBoo, is a low [Fe/H] giant, bright in the night sky. The stellar parameters, determined using optical spectra, are needed to be accurately determined to minimise systematic uncertainties. For Arcturus, the stellar parameters compared with the benchmark Gaia stellar parameters, presented by Jofré et al. (2015), can be seen in table 4.4. The stellar parameters used in this work are within the errors determined, with the v_{mic} being slightly different. As the stellar parameters in this work agrees well with the benchmarked Gaia measurements, systematic uncertainties due stellar parameters are expected to be minimal. Thus, the primary contribution to uncertainties in the abundance measurements are thought to occur due to the atmospheric models and the atomic data, mainly oscillator strength.

4.5.2 Random uncertainties

SME calculates the uncertainties in the measurements, estimating an uncertainty contribution due to the model atmosphere (Piskunov & Valenti 2017). This is unfortunately not the true uncertainty measurements of the abundance measurement, thus a different approach in estimating the uncertainties is done.

In this work, the spectra are treated homogeneously where the masks of continuum and lines are treated equally and each measurement of each line masks are checked to ensure that the masking is not contributing to (random) uncertainties. Furthermore, the same

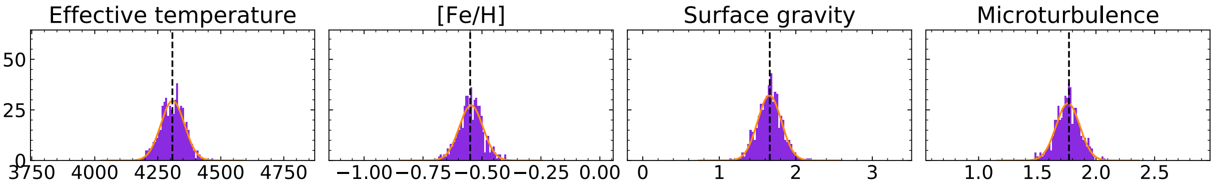

Figure 4.5: The figure shows a histogram of 500 stellar parameters centered with Arcturus measurements. The standard deviations are ±50 K for T_{eff}, ±0.15 dex for $\log g$, ±0.05 dex for [Fe/H], and ±0.1 km/s for v_{mic}

atomic data are used in each elemental abundance measurement, thus minimizing the contribution of uncertainties from choice of line - and continuum masks.

A method of measuring the uncertainties is using a well-measured spectroscopic star and vary the stellar parameters. In this sample, a standard well-measured giant star is Arcturus. Arcturus has the following stellar parameters:

$$\begin{aligned} T_{\text{eff}} &= 4308 \text{ K} \\ \log g &= 1.66 \text{ dex} \\ [\text{Fe/H}] &= -0.55 \text{ dex} \\ v_{\text{mic}} &= 1.77 \text{ km/s} \end{aligned}$$

The standard deviation of Arcturus-measurements determine the uncertainties of each elemental abundance measurements. A sample of 500-Arcturus spectra have stellar parameters varied following a Gaussian distribution centered around the Arcturus stellar parameters, described above. The standard deviation are ±50 K for the effective temperature, ±0.15 dex for surface gravity, ±0.05 dex for metallicity, and ±0.1 km/s for micro turbulence; which is typical for all stars in this thesis. A histogram of the parameters can be seen in figure 4.5. The standard deviation in the uncertainties follow the routine by Jönsson et al. (2017), where the stellar parameters are determined using optical measurements of these stars. The elemental abundance uncertainty measurements of the 500 Arcturus spectra with stellar parameters following figure 4.5 can be seen in figure 4.6. The uncertainties range from 0.04 dex (Na and Cu) to 0.11 (Ce). These are marked as the uncertainties in the abundance measurement plots.

4.6 APOGEE Measurements

APOGEE has an existing internal method of determining the stellar parameters and abundance measurements, called *APOGEE Stellar Parameters and Chemical Abundance Pipeline* (ASPCAP). This is developed to constrain these parameters specifically for APOGEE spectra. The reduction process of spectra is thoroughly described in Nidever et al. (2015).

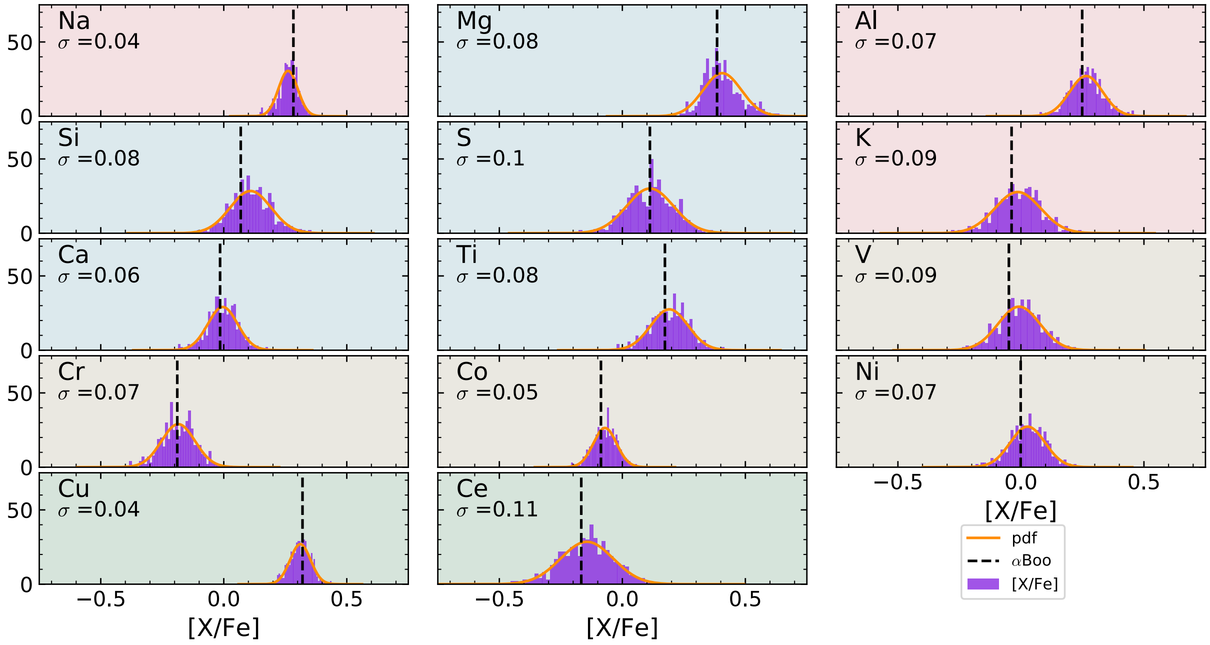

Figure 4.6: The figure shows a histogram of the 500 abundances measured of Arcturus with varying stellar parameters. The histogram are expected to peak at [X/Fe] $\neq 0$, as these uncertainties are reflecting the abundance measurements with Arcturus.

ASPCAP retrieves the parameters in two step. Firstly, a grid of pre-existing spectra are interpolated to fit the observed following a χ^2-minimization (García Pérez et al. 2016). Secondly, individual elemental abundances are measured one at a time, by optimizing the spectral fits (Holtzman et al. 2015).

The first step is to retrieve the stellar parameters T_{eff}, $\log g$, v_{mic}, $v_{\text{mac}}/v \sin i$, overall abundance [M/H], abundances of α-elements, and carbon- and nitrogen abundances. A linelist consisting of theoretical, astrophysical and laboratory atomic data is adopted (Shetrone et al. 2015). For the latest data release (DR16), a new set of MARCS-grids (Gustafsson et al. 2008) were created to generate synthetic spectra with a linelist updated to include Ce and Nd (Smith et al. in prep). ASPCAP has an independent code, `FERRE` (Allende Prieto et al. 2006), that searches for the best fit of the existing synthetic spectra, allowing for interpolation of the synthetic spectrum, to extract the stellar parameters. The synthesized spectra are made with a fast-computing-code, generating spectra with varying $\log(gf)$ to fit the Sun and varying the damping to fit Arcturus (Holtzman et al. 2018). To find the best fitting spectrum of the observation, a χ^2-minimization method is used (Holtzman et al. 2015, 2018). These are known as the **uncalibrated** stellar parameters.

Post-processing are done with the ASPCAP measurements. The T_{eff} and $\log g$ are calibrated with known, independent measurements of photometric and asteroseismic measurements, respectively (Holtzman et al. 2015), for stars with such measurements. Internal calibration of the T_{eff} are done with a trend of T_{eff}. This relation is believed to be a 3rd order dependence, which, for giants, is restricted in the range of 3800 K and 5250 K. T_{eff} are further calibrated by correlating with photometric measurements, where [Fe/H] dependent temperature correction is applied. Kepler field stars provide highly accurate asteroseismic $\log g$ measurements, which are used for the $\log g$ calibrations. The T_{eff} and $\log g$ calibrations are corrected for giants and dwarfs separately. These are known as the **calibrated** stellar parameters.

Using the best fitted spectrum with the uncalibrated stellar parameters, individual elemental abundances are measured in ASPCAP. The α-elements are part of the determined stellar parameters, where O, Mg, Si, S, Ca and Ti are simultaneously derived by varying the [α/Fe]-parameter. Other abundances are determined one element at a time, allowing for the synthesized spectra to focus on the wavelength regions of the element. The synthetic spectra is fitted within these windows.

Calibration of abundance measurements are done assuming solar neighbourhood stars has a similar abundance to that of the Sun (Holtzman et al. 2018). The remaining elements of interest are determined by weighting the reproduction of the wavelength-region using an Arcturus-like star (Holtzman et al. 2015). These are known as the **calibrated** abundance measurements.

Chapter 5

Results

The abundance measurements using *Spectroscopy Made Easy* are presented in this chapter. 14 elemental abundances of 291 spectra are obtained of the four elemental groups of light (3), α (5), iron-peak (4) and neutron-capture (2) elements.

5.1 Data Selection

The data, as described in section 3.1, consist of medium-resolution (R=22, 500) H-band spectra of K-giants. Initially, the quality cuts made in the 308 original spectra are requiring a S/N $\geq$ 100, removing 8 stars. All of the synthetic spectra are **manually** checked to see whether the parameters might be well-constrained. Further cuts are made when the v_{mac} and v_{rad} are constrained, where 7 stars are removed due to bad fits.

One star with two spectra in the sample has a [Fe/H] = -2.83. The low [Fe/H]-spectra made it difficult to disentangle lines from the noise of the spectra, thus these two measurements are also removed from the sample.

The end sample consists of 291 (+ solar spectrum) spectra of 263 K-giants. The properties of the parameters are as following:

$$\begin{aligned}
100 &\leq \text{S/N} \leq 1700 \\
3950\,\text{K} &\leq T_{\text{eff}} \leq 5250\text{ K} \\
0.5 &\leq \log g \leq 3.6 \\
-2.1 &\leq [\text{Fe/H}] \leq 0.4 \\
1.1\text{ km/s} &\leq v_{\text{mic}} \leq 2.3\text{ km/s} \\
5.3\text{ km/s} &\leq v_{\text{mac}} \leq 12.5
\end{aligned}$$

A final quality cut is made by looking through the synthetic spectra of the elemental abundance. A synthetic spectrum is created for each line of interest, and these synthetic spectra

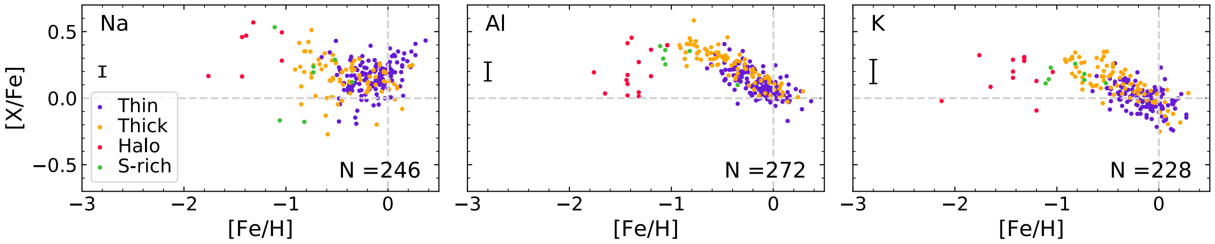

Figure 5.1: The figure shows the abundance trends of light elements: Na, Al and K. The plots show the purple as thin disk stars, yellow as thick disk stars, red as halo and green as s-rich stars, with the number of measurements indicated on the bottom right corner.

are manually checked to see whether fits were representative of the line and continuum for each star. This is to ensure that the line of interest does not show peculiar features not representing the abundance measurement, e.g. a bad measurement or a line too weak for a specific star, as the continuum and line masking are done using 50 stars, representing the whole sample.

5.2 Elemental abundances

In this section, the abundance measurements using the method described in section 4.4 are presented. A typical visualization of chemical evolution is in [X/Fe] vs. [Fe/H] trends. The abundances are related to Fe due to the richness of Fe-lines within optical and infrared spectra. An overview of the transition lines used for each element can be seen in table 5.1, where the wavelength, oscillator strength, lower and upper energy is indicated for each element. Figures 5.1, 5.2, 5.3 and 5.4, presented below are of each successful abundance measurements using the lines presented in table 5.1. The population separation are explained in section 4.4.3, with the thin disk stars represented as purple, thick disk stars as orange and halo stars represented in red. The green represents the s-rich stars, where a higher abundance of s-process elements have been measured with high resolution optical spectra (R. Forsberg Master Thesis (2019)).

5.2.1 Odd Z-elements

Sodium One line within the APOGEE range is used to determine the Na abundance of 246 spectra. The left trend in figure 5.1 shows a large scatter in the abundances trend, with the trend barely going through the solar value. The one line used is highly blended with Ni, which possible causes the large scatter, where the other line available is too weak.

Aluminium Al abundance, middle in figure 5.1, is determined using one line using 263 spectra. Al has shown strong lines, suggesting strong NLTE-effects. The line used has the weakest NLTE effects according to Nordlander & Lind (2017), where the broadening

Element	Wavelength [Å]	log(gf)	E$_{low}$	E$_{up}$	Reference
Na I	16388.85	-1.027	3.7533	4.5096	Ralchenko et al. (2010)
Mg I	15740.70	-0.223	5.9320	6.7190	Ralchenko et al. (2010) (gf: Pehlivan Rhodin et al. (2017))
Mg I	15748.99	0.129	5.9320	6.7190	Ralchenko et al. (2010) (gf: Pehlivan Rhodin et al. (2017))
Mg I	15886.19	-1.896	5.9459	6.7262	Ralchenko et al. (2010) (gf: Pehlivan Rhodin et al. (2017))
Mg I	15954.45	-0.757	6.5879	7.3648	Ralchenko et al. (2010)
Al I	16763.37	-0.514	4.0872	4.8266	Wiese et al. (1969), (gf:Asimina Papoulia , broad:Nordlander & Lind (2017))
Si I	16163.71	-0.862	5.9537	6.7206	Kurucz (2007)
Si I	16241.85	-0.770	5.9639	6.7271	Kurucz (2007)
Si I	16380.14	-0.465	5.8625	6.6192	Kurucz (2007)
S I	15403.77	0.730	8.6995	9.5042	Biemont et al. (1993)
S I	15478.48	0.180	8.0457	8.8464	Biemont et al. (1993)
K I	15163.09	-0.613	2.6700	3.4874	Kurucz (2012)
K I	15168.40	0.480	2.6702	3.4874	Wiese et al. (1969)
Ca I	16136.82	-0.363	4.5313	5.2995	Kurucz (2007)
Ca I	16155.24	-0.496	4.5322	5.2995	Kurucz (2007)
Ca I	16197.08	0.254	4.5347	5.3000	Kurucz (2007)
Ti I	15543.75	-1.080	1,8792	2.6766	Blackwell-Whitehead et al. (2006)
Ti I	15602.84	-1.435	2.2674	3.0618	Kurucz (2010)
Ti II	15873.84	-1.900	3.1235	3.9044	Kurucz (2010), (gf:Wood et al. (2014))
Ti I	16330.54	-0.890	3.1081	3.8672	Wickliffe et al. (2000)
V I	15924.81	-1.108	2.1377	2.9161	Kurucz (2009)
Cr I	15680.06	0.152	4.6969	5.4874	Kurucz (2010) & WLHK
Co I	16757.64	-0.923	3.4092	4.1489	Kurucz (2008)
Ni I	15555.38	0.218	5.4879	6.2847	Kurucz (2008)
Ni I	16363.09	0.588	5.2825	6.0400	Kurucz (2008)
Ni I	16673.70	0.388	6.0346	6.7780	Kurucz (2008)
Cu I	16005.54	-0.045	5.3483	6.1227	Kurucz (2011)
Cu I	16638.98	0.070	6.1227	6.8676	Biémont (1973)
Ce II	15784.75	-1.540	0.3178	1.1030	Cunha et al. (2017)
Ce II	16376.48	-1.790	0.1224	0.8793	Cunha et al. (2017)
Ce II	16595.18	-2.190	0.1224	0.8694	Cunha et al. (2017)

Table 5.1: The table shows the line list used in abundance measurements with the wavelength, line strength and the upper and lower energies, with references for all and specified corrections if included.

effects have been taken into account. The NLTE-effect have been accounted for and the trend shows an increase in lower [Fe/H] with a peak ∼ -0.7 dex. The thin- and thick disk show a decrease in [Fe/H], where the thick disk stars have a lower Al-abundance than thin disk (which will be discussed more in chapter 6; e.g. top right in figure 6.2).

Phosphorous P has three lines within the APOGEE range, but all of the trends using each line shows a large scatter and no trend. Each of the lines are highly blended with molecular lines - CN, CO and OH. For a high surface temperature, molecular lines are minimized, but the number of spectra with high temperatures was too small a sample, where a trend could be identified confidently. Other two P-lines have been identified within

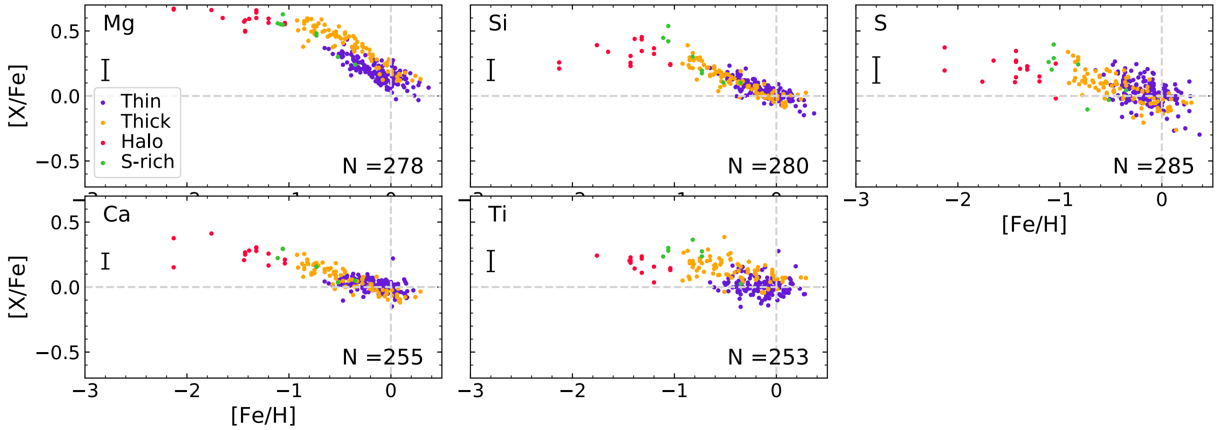

Figure 5.2: The figure shows the abundance trends of α-elements: Mg, Si, S, Ca and Ti. The plots show the purple as thin disk stars, yellow as thick disk stars, red as halo and green as s-rich stars, with the number of measurements indicated on the bottom right corner.

the APOGEE-range. These two lines are too weak, and are unfortunately not measurable in this work. These lines are in 16590.05 Å and 16803.37 Å.

Potassium The K-trend is determined using two lines using 228 spectra. The trend on the right in figure 5.1 goes through the solar-values, and although the trends shows a bit of a scatter, the lines used are showing a knee-like trend, or a trend following the typical one for the α-elements.

5.2.2 α-Elements

Magnesium The Mg-abundance trend is measured using four lines on 278 spectra. The trend on the top left in figure 5.2 shows higher values, and not going through the solar value. The $\log(gf)$'s of the lines are improved by using measurements by Pehlivan Rhodin et al. (2017). A separation is clearly seen in figure 5.2 with thick disk-stars having higher abundance than the thin disk-stars with a knee-like trend. Although only four lines were used, other lines that were not used, show a knee-like trend but with sub- or super-solar values. This is due to the line strengths of each line, but these are disregarded.

Silicon Three lines were used to determine the Si-abundance trend with updated line strengths from Pehlivan et al. (in prep.), measured in the laboratory. The trend can be seen in the top middle in figure 5.2 using 280 spectra. Although no scatter can be seen in the trend, no thin and thick disk separation is observed. Line-by-line trends of the 14 Si-lines showed no large scatter, but due to the uncertainty of the line strength, lines are discarded. The trend shows decreasing Si-abundance with higher [Fe/H], as is expected due to Si being an α-element.

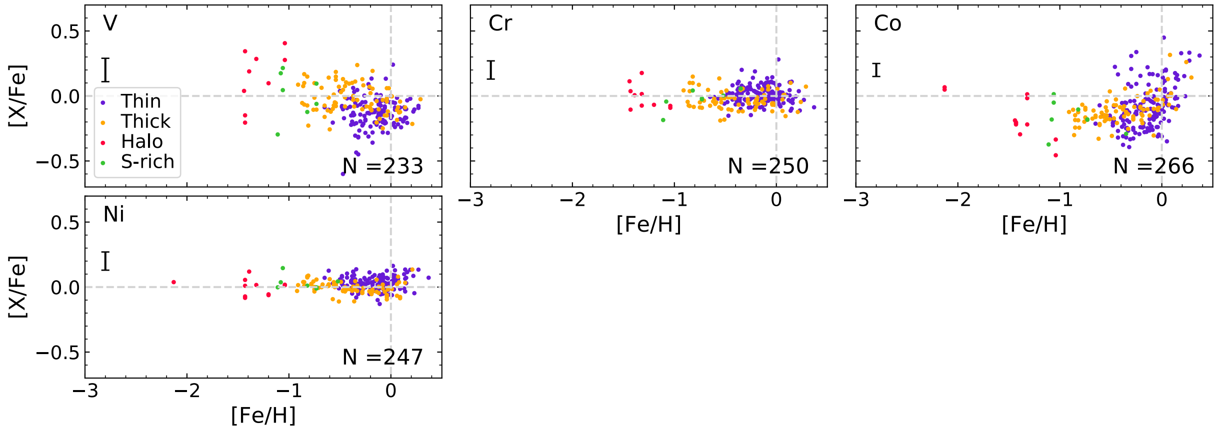

Figure 5.3: The figure shows the abundance trends of iron-peak-elements: V, Cr, Co and Ni. The plots show the purple as thin disk stars, yellow as thick disk stars, red as halo and green as s-rich stars, with the number of measurements indicated on the bottom right corner.

Sulphur S-abundances were determined using two lines of 285 spectra. The trend can be seen on the top right in figure 5.2. Strong lines are discarded from being used in determining the abundances, which also shows a large scatter in line-by-line trends. Although there is a small scatter, the abundance of solar spectra agree with the solar-values.

Calcium The Ca-abundance is determined using three lines measured on 255 spectra. The trend in figure 5.2 bottom left, shows very little scatter and decreasing Ca-abundance with increasing [Fe/H]. The thin disk stars shows a constant Ca-abundance with increasing [Fe/H] where the thick disk shows a decreasing Ca-abundance with increasing [Fe/H], as the latter.

Titanium Four lines are used to determine the abundance of Ti using 253 spectra. Of the four lines, the Ti II line strengths is updated using $\log(gf)$-value by Wood et al. (2014). The trend in figure 5.2 bottom middle, shows a plateau with decreasing Ti-abundance at higher [Fe/H], and decreasing abundance with increasing [Fe/H] of the thick disk. A roughly constant Ti-abundance with increasing [Fe/H] of the thin disk is observed.

5.2.3 Iron-peak Elements

Vanadium The V-abundance is determined using one line measured on 233 spectra. The lines discarded showed high scatter in the line-by-line, such that a trend could not be identified. The one V-line used to determine the abundance in this work showed the least scatter, which can be seen on the top left in figure 5.3. The thick disk shows to have constant solar abundance with [Fe/H], where the thin disk shows lower V-abundance although also constant with increasing [Fe/H]. This is empirised later by looking at the running mean in section 6.

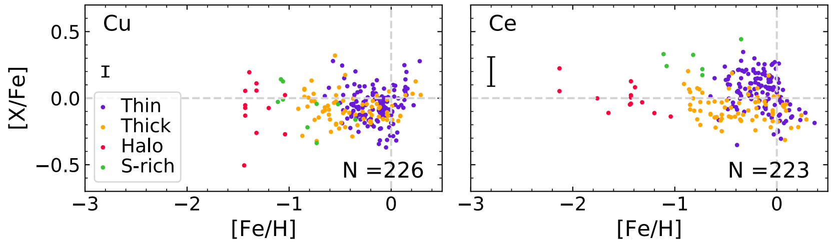

Figure 5.4: The figure shows the abundance trends of α-elements: Cu and Ce. The plots show the purple as thin disk stars, yellow as thick disk stars, red as halo and green as s-rich stars, with the number of measurements indicated on the bottom right corner.

Chromium The Cr-abundances are determined using 249 spectra. The trend, middle in figure 5.3, shows little scatter, with the solar Cr-abundance constant with [Fe/H]. The thin disk shows to have higher Cr-abundance than the thick disk with increasing [Fe/H], and changing to the thick disk having higher Cr-abundance than the thin disk above solar-[Fe/H].

Manganese The Mn-abundances were not determined as all three lines separately shows super-solar values with higher [Fe/H], suggesting an NLTE-effect. NLTE effects of Mn have been observed in the optical regime (Lomaeva et al. 2019), and NLTE-corrections are not available in the IR-regime.

Cobalt The trend of Co on the top right in figure 5.3 uses 266 spectra, and shows a large scatter. The trend shows a roughly constant solar Co-abundance with increasing [Fe/H], and above solar-[Fe/H] increases rapidly. The thin and thick disk stars both show a trend of rapid increase around solar-[Fe/H] while being constant in sub-solar Co-abundance.

Nickel The Ni-abundance is determined using 247 spectra. The discarded lines shows very high scatter, where most of the lines are blended with molecular CN, CO and OH and are very weak lines. The final trend, bottom-left in figure 5.3, shows a constant Ni-abundance with [Fe/H]. The thin and the thick disk shows constant solar Ni-abundance with increasing [Fe/H], but the thick disk, with lower abundance than the thin disk, increases rapidly above solar-[Fe/H] to higher Ni-abundance thin disk stars.

5.2.4 Neutron-capture Elements

Copper The Cu-abundance trend, seen left in figure 5.4, is determined using 225 spectra. There is a high scatter in the abundance line-by-line of the two lines, but these showed similar trends. The third line was discarded due to being highly blended with Fe. The trend of Cu, although showing high scatter, shows a roughly constant abundances with increasing [Fe/H], and increasing Cu-abundance above solar values. The thick disk shows sub-solar values of abundance constant with [Fe/H], where the thin disk shows a high scatter and high increase with [Fe/H] above solar-[Fe/H].

Germanium The Ge-abundance trend is not determined with the one available line within the range of APOGEE. Abundance measurements of this element was attempted but not successful to obtain. The Ge-line is on the wing of a Fe-line, thus making it hard to determine a trend.

Rubidium The Rb-abundance trend could not be determined due to a large scatter in the trend as well as high values. The only line available is near a molecular CN-molecular line, as well as being blended with Fe. Abundance measurements of this element was attempted but not successful to obtain.

Cerium The Ce-abundance is determined using 223 spectra. The discarded lines showed high scatter in line-by-line abundance measurements for some lines, making it hard to determine a trend. Some of the lines discarded are due to being in the wings of Nd, which has no abundance-measurements in this work, and CO. The Ce-trend, right in figure 5.4, shows high scatter, but the green, which have been identified as s-rich stars, are seen to show high abundances. This shows the accuracy of the abundance determinations of this work. The thin disk shows higher abundances with decreasing abundance above solar-[Fe/H], and the thick disk is roughly constant with [Fe/H], showing sub-solar abundances.

Neodymium Nd-abundance trend could not be determined using the available lines within the APOGEE range. The atomic data of Nd from Hasselquist et al. (2016) were adopted due to VALD-linelist having no Nd atomic data. The scatter is too high for a trend to be visible, and the lines are highly blended with molecular line, CO. Abundance measurements of this element was attempted but not successful to obtain.

Ytterbium Yb-trend could not be determined using the one line available within the range of APOGEE. The line is highly blended with the molecular line, CO.

Of all the elements, the line-information and the number of possible lines can be seen in table 5.1 and 5.2, respectively.

Element	No. Lines Investigated	No. Lines Used	No. of Spectra
Na	2	1	246
Mg	9	4	278
Al	3	1	272
Si	14	3	280
P	5	0	0
S	6	3	285
K	2	2	228
Ca	6	3	255
Ti	9	4	253
V	8	1	233
Cr	3	1	249
Mn	3	0	0
Co	8	1	266
Ni	28	3	247
Cu	3	2	225
Ge	1	0	0
Rb	1	0	0
Ce	8	3	223
Nd	10	0	0
Yb	1	0	0

Table 5.2: The table shows the elements of interest with number of lines within the range of APOGEE and the number of lines used to determine the elemental abundances.

Chapter 6

Discussion

The abundance measurements of all elements done by me using APOGEE spectra are compared with the ”official” uncalibrated and the calibrated abundance measurements of APOGEE data release 16 (Ahumada et al. 2019), as well as with abundances determined using high-resolution optical spectra (Jönsson et al. in prep.). Furthermore, as a way of tracking down differences, I also determine the very same abundances from the APOGEE spectra twice more using the ”official” APOGEE DR16 uncalibrated and calibrated stellar parameters as input. Finally, relative ages for a sub-sample of stars in this work are discussed.

The trends of each four chemical groups measured in section 5 are compared with the bench-marked optical measurements by Jönsson et al. (in prep.). The abundance measurements using SME, are done without any calibration. All 14 elemental abundance determined can be seen in figure 6.1 with the running mean trends in figure 6.2.

Each elemental abundance trends determined in this thesis and the ASPCAP abundance (described in section 4.6) trends are compared to the high resolution optical abundance measurements and discussed below. The high resolution optical abundance measurements by Jönsson et al. (in prep.) are marked as the ”true” values of abundance measurements, to evaluate most accurate and precise abundance measurement-method using IR APOGEE spectra. These abundance measurements have been compared to abundance measurements of dwarfs by e.g. Battistini & Bensby (2015) for iron-peak elements and Delgado Mena et al. (2017) for neutron-capture elements.

6.1 Comparison to Optical and ASPCAP

In this section, the abundances analyzed in this work and by uncalibrated and calibrated APOGEE by Ahumada et al. (2019) are compared with optical abundance measurements by Jönsson et al. (in prep.). The figures show each abundance trend of this work and APOGEE over-plotted on optical measurements separated by elemental group. The same

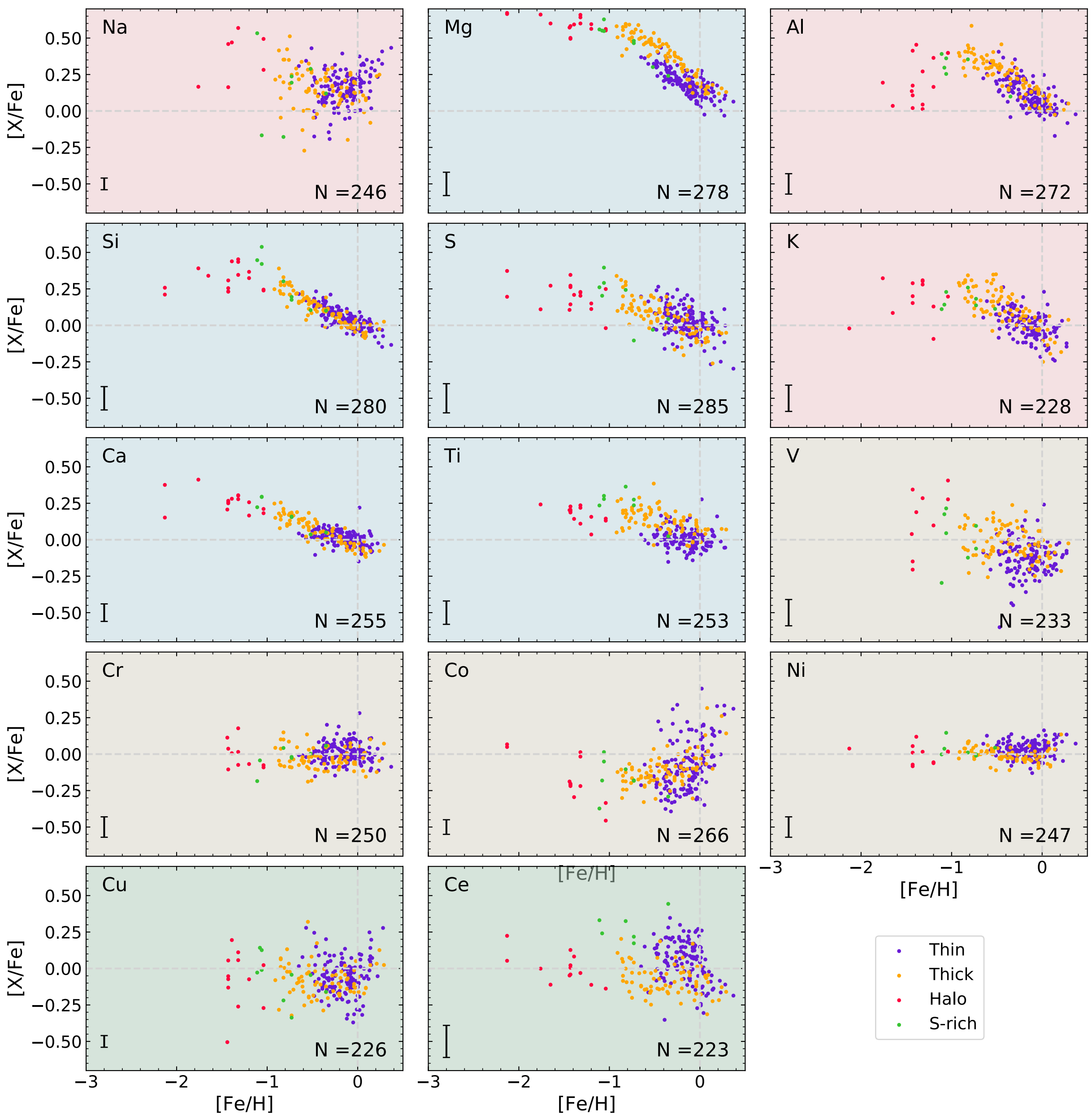

Figure 6.1: Abundance trends with [Fe/H] of all elements. Each element is indicated at the top left corner, with pink, blue, grey and green background indicating odd-Z-, α-, iron-peak - and neutron-capture element. These trends are the same as presented in figures 5.1, 5.2, 5.3 and 5.4. On the bottom right is indicated the sample number. For each trend, purple indicates the thin disk star, orange indicates a thick disk star, red indicated halo star and green indicates s-rich star.

figure-representation is used in section 6.2.

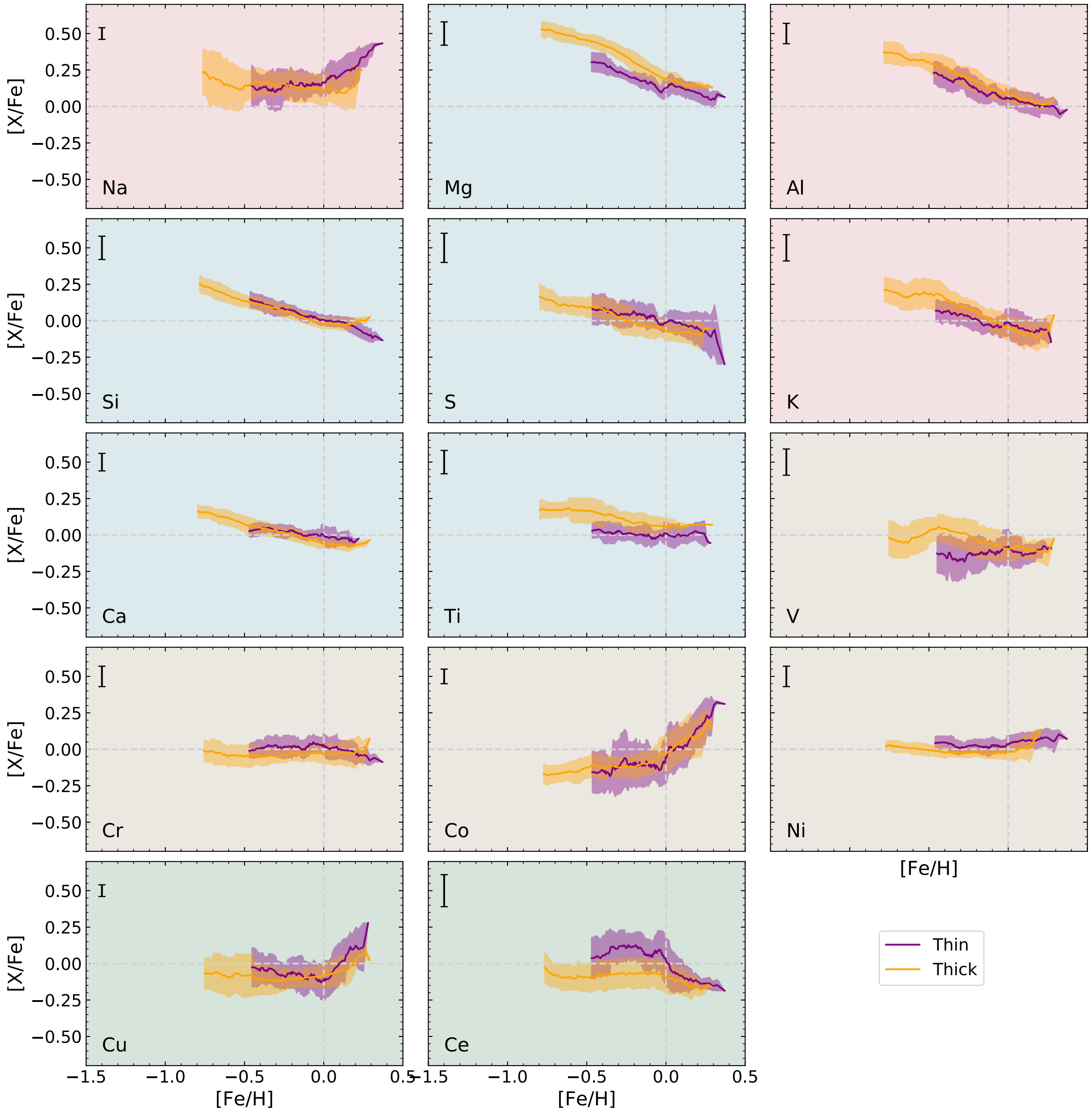

Figure 6.2: Running mean abundance trends with [Fe/H] of all elements. Each element is indicated at the top left corner, with pink, blue, grey and green background indicating odd-Z-, α-, iron-peak - and neutron-capture element. For each trend, purple line indicates the mean thin disk trend with light purple the standard deviation and orange indicates a thick disk trend with light orange the standard deviation.

The comparison between optical abundances and abundances of this work are shown in the figures of this section and section 6.2. The overall comparison between these abundances are described only in this section.

For readability, the following notations are adopted:

Optical abundance measurements by Jönsson et al. (in prep)	**Opt-Abund**
Main abundance measurements of this work	**IR-Abund**
Uncalibrated abundance measurements of APOGEE DR16	**Uncal-ASPCAP**
Calibrated abundance measurements of APOGEE DR16	**Cal-ASPCAP**
Abundance determinations by me using DR16 uncal. stellar parameters	**Uncal+SME**
Abundance determinations by me using DR16 cal. stellar parameters	**Cal+SME**

6.1.1 Light Elements

The abundance trends of light elements (Na, Al and K) can be seen in light pink in figure 6.1 and the running mean trends can be seen in light pink in figure 6.2 with the comparison to Uncal-ASPCAP and Cal-ASPCAP in figure 6.3.

The abundances of Al and K are showing α-like trends, with decreasing abundance with increasing metallicity. This is due to the production channel of both elements occurring in heavier element burning, like the α-elements, as described in section 2, and expelled mainly during SNe II.

A high scatter in Na is observed with IR-Abund, especially a large deviance in the lower [Fe/H]. Na is mainly produced during carbon burning, yet the scatter is thought to be due to the blending of Ni. This high scatter in Na is also observed by Uncal-ASPCAP and Cal-ASPCAP. A tight banana-shaped trend (a decrease and then increase in [Na/Fe] with higher metallicity) is observed by Bensby et al. (2014) and Hawkins et al. (2016). This banana-shape is observed in the running mean in the top left in figure 6.2.

The light element abundances of Na and Al are showing a good agreement with Opt-Abund (see figure 6.3) with lowest mean-difference for both elements (see table 6.1. The mean difference are within the estimated errors determined with IR-Abund (σ([Na/Fe]) = 0.04 and σ([Al/Fe]) = 0.07), suggesting that the atomic data are more precise, with the NLTE-effects in Al taken into account in IR-Abund. The Na and Al trends in figure 6.3 show better agreement with Opt-Abund than Uncal-ASPCAP and Cal-ASPCAP trends. A high scatter observed in Na is also observed in both ASPCAP measurements, yet Na of IR-Abund without calibration agrees best with the Opt-Abund with the lowest mean and standard deviation. The higher standard deviation in Al is thought to occur due to IR-Abund having a tighter trend than the Opt-Abund around solar-[Fe/H], with the IR-Abund going through the solar-abundance.

No Opt-Abund of K with this sample are available due to lack of lines, yet the trends show agreement with the three methods of IR-Abunda, Uncal-ASPCAP and Cal-ASPCAP in figure 6.3. A summary of the mean and standard deviation of the three measurements can be seen in table 6.1. The knee-like trend with K is also observed by Hawkins et al. (2016).

Element	IR-Abund		Uncal-ASPCAP		Cal-ASPCAP	
	Mean	Standard Deviation [dex]	Mean	Standard Deviation [dex]	Mean	Standard Deviation [dex]
Na	0.040	0.133	-0.076	0.149	-0.097	0.149
Al	0.048	0.098	0.082	0.076	-0.066	0.076
K	-	-	-	-	-	-

Table 6.1: A summary of the mean difference and standard deviation of odd-Z element of abundancese by IR-Abund, Uncal-ASPCAP and Cal-ASPCAP, respectively.

This is expected as K is thought to be produced mainly in SNe II (see section 2).

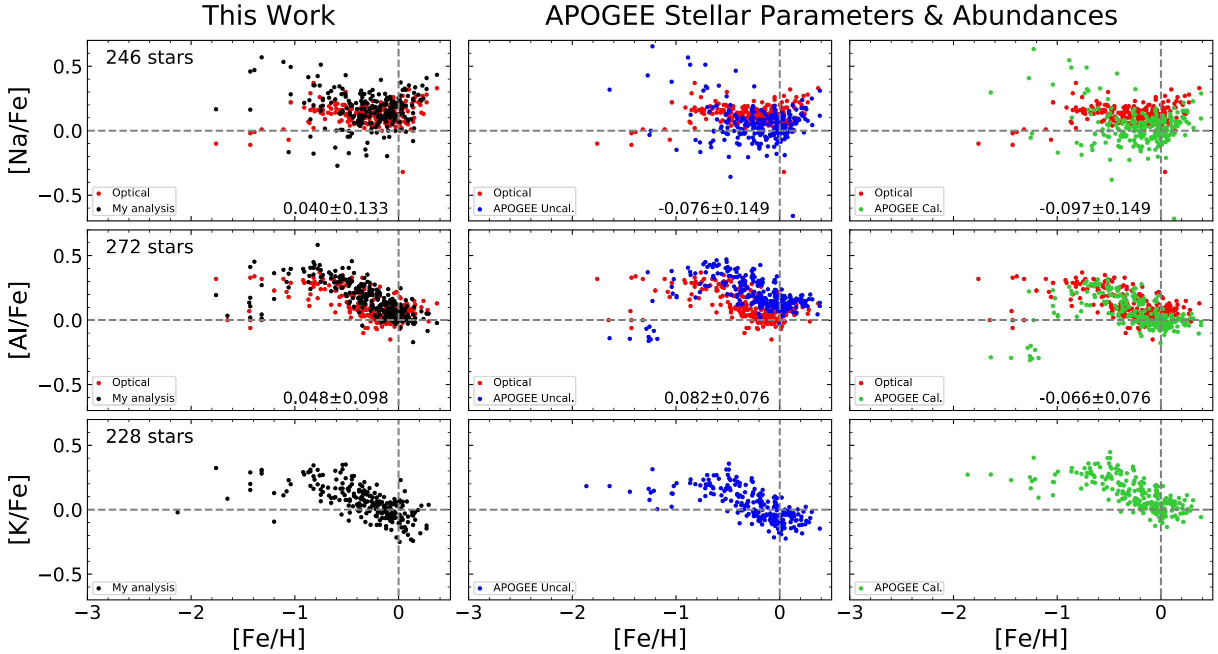

Figure 6.3: The figure shows the abundances of light elements Na, Al and K of IR-Abund (black), Uncal-ASPCAP (blue) and Cal-ASPCAP (green) compared with the Opt-Abund by Jönsson et al. (in prep). The number of stars compared can be seen on the top left, with the mean and standard deviation on the bottom right of each subfigure.

6.1.2 α Elements

The five elements show a similar trend with a plateau at lower [Fe/H] and a decrease with increasing [Fe/H]. This is due to the α-elements mainly produced in massive stars and expelled during SNe II, whereas [Fe/H] is produced in both SNe I and SNe II. The well-observed knee-like trend is due to the delayed contribution of Fe from SNe I, as the lower mass stars with longer lifetimes begin to enrich the interstellar medium with Fe, thus decreasing the [α/Fe]. The plateau at lower [Fe/H] for Mg in IR-Abund agrees well with

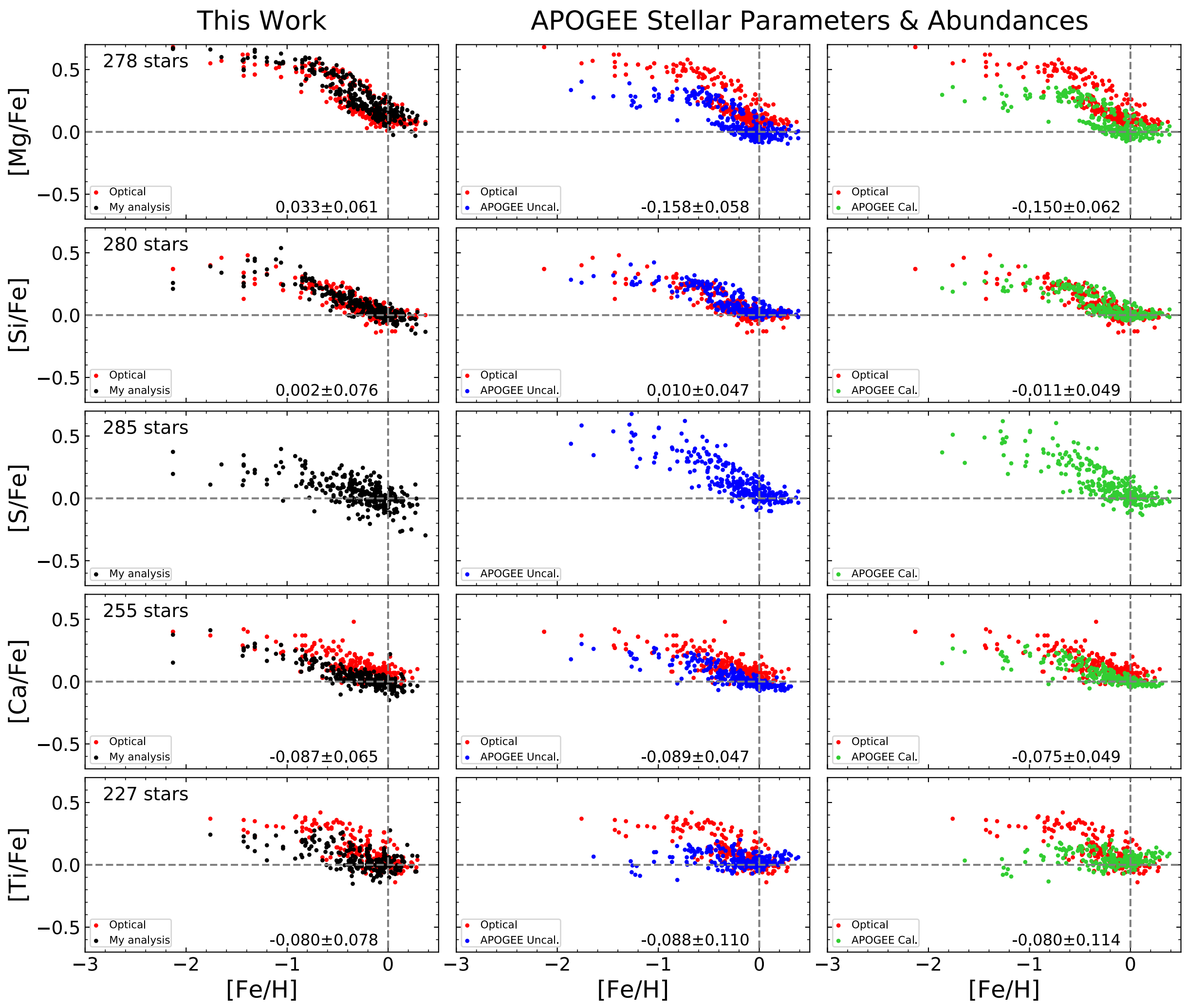

Figure 6.4: The figure shows the comparison of α elements Mg, Si, S, Ca and Ti of IR-Abund and ASPCAP, with the same description as figure 6.3.

the Opt-Abund. Uncal-ASPCAP and Cal-ASPCAP measures this plateau ~ 0.2 dex lower.

A very nice knee-like structure is observed in the [Mg/Fe] vs. [Fe/H] trend (top middle in figure 6.1), showing a separation in the abundances of thin and thick disk stars. The running mean of these (top middle in figure 6.2) shows a higher decreasing trend in the thick disk compared with the thin disk. This separation is observable in abundance trend of [Ti/Fe] vs. [Fe/H] (middle in figure 6.1), yet strangely not observable in other α-elements, especially Si, showing abundances of the thin and thick disk nicely correlating in a decreasing trend. ASPCAP finds a separation in the Si and S, yet there is no clear separation observed with IR-Abund. This separation is not observed with the Opt-Abund of Si-abundance.

	IR-Abund		Uncal-ASPCAP		Cal-ASPCAP	
Element	Mean	Standard Deviation [dex]	Mean	Standard Deviation [dex]	Mean	Standard Deviation [dex]
Mg	0.033	0.061	-0.158	0.058	-0.150	0.062
Si	0.002	0.076	0.010	0.047	-0.011	0.049
S	-0.037	0.098	0.054	0.086	0.031	0.083
Ca	-0.087	0.065	-0.089	0.047	-0.075	0.049
Ti	-0.080	0.078	-0.088	0.110	-0.080	0.114

Table 6.2: A summary of the mean difference and standard deviation of α-elements of abundances by IR-Abund, Uncal-ASPCAP and Cal-ASPCAP, respectively.

The α-trends in IR-Abund show agreement with the Opt-Abund. The α-elements mean and scatter difference compared with the Opt-Abund are within the estimated errors, except Ca, as can be seen in table 6.2. Uncal-ASPCAP measures the α-elements in well agreement with Opt-Abund, with knee-like trends for Si, S and Ca. A lower standard deviation between the differences is observed for Mg, Si, S and Ca by Uncal-ASPCAP, as can be seen in table 6.2, although Mg shows a lower [Mg/Fe]-plateau in the lower metallicities.

Ca and Ti are primarily formed during silicon burning in massive stars, thus a knee-like structure is expected (and observed with IR-Abund). ASPCAP measures a lower abundance at lower [Fe/H] for Ca and Ti[1]. Ti, measured with IR-Abund, is observed to have a knee-like trend, where the ASPCAP measures a fairly flat trend with [Fe/H]. Hawkins et al. (2016) observed a similar discrepancy in the lower [Fe/H] of Ti compared with ASPCAP DR14 (Holtzman et al. 2015), and re-measurements with manual choosing of lines, which measured the knee-like trend, much like optical measurements by Bensby et al. (2014). The T_{eff} is well-known to highly affect the Ti-abundance, thus the lack of the expected structure suggest that T_{eff} is not well-constrained. This is investigated further in section 6.2.

6.1.3 Iron-Peak Elements

The iron-peak elements of V, Cr and Ni show a similar trend with IR-Abund with a fairly flat trend of solar-abundance with increasing [Fe/H]. This is due to the similar formation channels of these elements with Fe, where a larger fraction of these elements are produced in SNe I with a contribution from SNe II.

The IR-Abund, Uncal-ASPCAP and Cal-ASPCAP show a fine wave-like Ni-trend with increasing metallicity. This wave-like, which is observed to be near-solar abundance values with a slight increase at solar-[Fe/H], is also observed by Hawkins et al. (2016). This roughly flat trend, also observed in [Cr/Fe]-trend, is due to correlates formation channels

---

[1] With IR-Abund, Ti I and Ti II-lines are used to represent the Ti-abundance, whereas the ASPCAP (Ahumada et al. 2019) present these separately. Only Ti I-abundance by ASPCAP are used here.

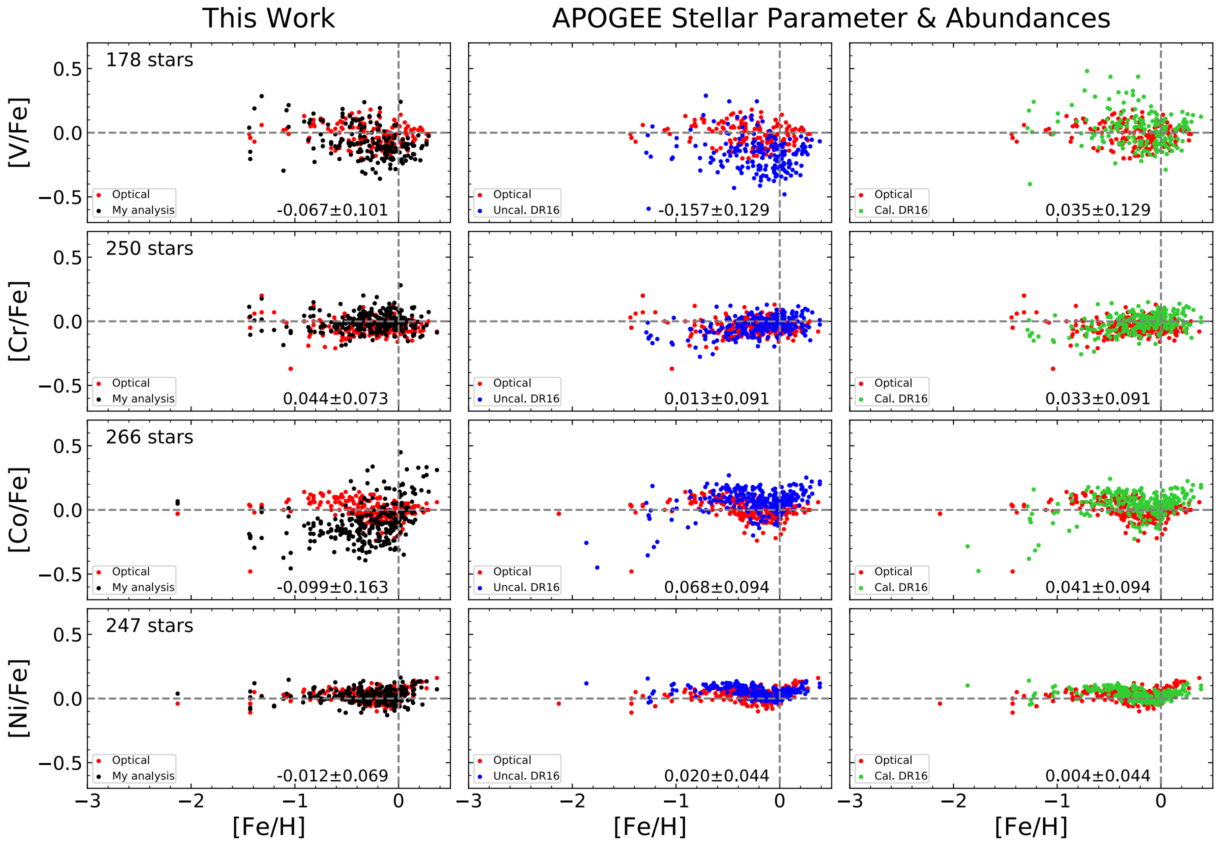

Figure 6.5: The figure shows the comparison of iron-peak elements V, Cr, Co and Ni of IR-Abund and ASPCAP, with the same description as figure 6.3.

with Fe.

Co does not agree with the Opt-Abund with a large scatter and rapid increase in Co-abundance at solar [Fe/H]. Co is produced with SNe I and SNe II, yet the line of Co is thought to be affected by hyperfine structure (Hawkins et al. 2016). The hyperfine-splitting of the line used would $\lambda \sim 0.74$ Å using APOGEE spectra. It is not possible to disentangle the hyperfine splitting at APOGEE resolving power, yet ASPCAP has measured a wavelike trend, similar to Opt-Abund.

The trend of V and Cr agree best with the Opt-Abund compared with ASPCAP, which is reflected in the lower standard deviation (table 6.3). The higher mean difference in IR-Abund can be explained with the large difference between the $\log(gf)$ of the lines used in IR-Abund and the $\log(gf)$'s used for ASPCAP (see table A.1).

Element	IR-Abund		Uncal-ASPCAP		Cal-ASPCAP	
	Mean	Standard Deviation [dex]	Mean	Standard Deviation [dex]	Mean	Standard Deviation [dex]
V	-0.067	0.101	-0.157	0.129	0.035	0.129
Cr	0.044	0.073	0.013	0.091	0.033	0.091
Co	-0.099	0.163	0.068	0.094	0.041	0.094
Ni	-0.012	0.069	0.020	0.044	0.004	0.044

Table 6.3: A summary of the mean difference and standard deviation of iron-peak elements of abundances by IR-Abund, Uncal-ASPCAP and Cal-ASPCAP, respectively.

6.1.4 Neutron-Capture Elements

The neutron capture elements with IR-Abund agree well with the Opt-Abund, as can be seen in the first column in figure 6.6.

The Cu-measurements in the lower [Fe/H] show a higher abundance at around [Cu/Fe] $\sim$ 0.0 dex compared with Opt-Abund at [Cu/Fe] $\sim$-0.5 dex. Cu is mainly produced during helium burning in the shell as a neutron capture which is [Fe/H] dependent. Thus, as expected, there is an increasing in Cu-abundance with increasing [Fe/H]. The running mean of the thin and thick disk separation in bottom left in figure 6.2, shows and overlap in the abundances of these populations, although a rapid increase with the thin disk compared with the thick disk is observed at solar-[Fe/H]. Although, the trends on the top row in figure 6.6 suggest that IR-Abund agrees better with the Opt-Abund, with lower mean difference and lower standard deviation (see table 6.4, there is a high scatter and no thin-thick disk separation is observed.

Ce agrees well with the Opt-Abund, with an increasing and decreasing Ce-abundance with increasing [Fe/H]. In figure 6.1, the thick disk [Ce/Fe] has a flat trend, with a decrease around solar-[Fe/H], showing an onset of the lower mass AGB stars. The thin disk stars show to have a decreasing trend at solar-[Fe/H] with the thick disk stars showing a rather flat trend with increasing metallicity, as can be seen in figure 6.2. The newly-measured Ce-abundance by ASPCAP shows a large scatter (Ahumada et al. 2019). Although the trends are shifted upwards (more in the Uncal-ASPCAP than Cal-ASPCAP), the overall shape with an increase and decrease are similar with IR-Abund and the Opt-Abund. A high scatter in Uncal-ASPCAP and Cal-ASPCAP is observed compared with Opt-Abund, and as Ce-lines are highly dependent on $\log g$-parameter, the surface gravity is further investigated in section 6.2.

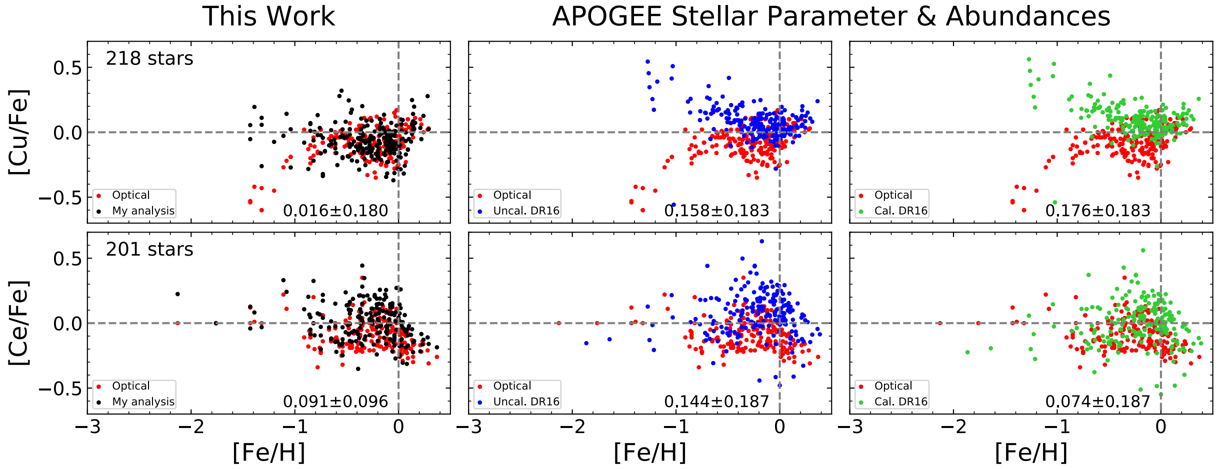

Figure 6.6: The figure shows the comparison of neutron-capture elements Cu and Ce of IR-Abund and ASPCAP, with the same description as figure 6.3.

Element	IR-Abund Mean	IR-Abund Standard Deviation [dex]	Uncal-ASPCAP Mean	Uncal-ASPCAP Standard Deviation [dex]	Cal-ASPCAP Mean	Cal-ASPCAP Standard Deviation [dex]
Cu	0.016	0.180	0.158	0.183	0.176	0.183
Ce	0.091	0.096	0.144	0.187	0.074	0.187

Table 6.4: A summary of the mean difference and standard deviation of neutron-capture elements of abundances by IR-Abund, Uncal-ASPCAP and Cal-ASPCAP, respectively.

6.2 Comparison to APOGEE Stellar Parameters with Manual Method

In this section, abundance measurements of IR-Abund are compared with the abundances measured measured using SME and the APOGEE stellar parameters.

APOGEE determines the uncalibrated stellar parameters using `FERRE`. The stellar parameters of T_{eff} and $\log g$ are calibrated to agree with photometric and asteroseismic measurements, respectively. The uncalibrated and calibrated abundances are determined using the uncalibrated stellar parameters, where calibrated abundances are shifted to ensure that the abundances go through the Solar-values in the [X/Fe] vs. [Fe/H]-plots, if measured too high or too low.

The comparison plots, presented as figures 6.3, 6.4, 6.5 and 6.6, can be seen in figures A.1, A.2, A.3 and A.4. These abundance measurements of the same elements follow the method described in section 4.4 of abundance measurements using APOGEE stellar parameters. The same atomic data and lines are used for measuring Uncal+SME and Cal+SME.

Element	IR-Abund Mean	IR-Abund Standard Deviation [dex]	Uncal+SME Mean	Uncal+SME Standard Deviation [dex]	Cal+SME Mean	Cal+SME Standard Deviation [dex]
Na	0.040	0.133	-0.027	0.139	-0.123	0.185
Mg	0.033	0.061	-0.061	0.064	0.033	0.061
Al	0.048	0.098	-0.013	0.097	0.215	0.171
Si	0.002	0.076	-0.023	0.073	0.135	0.107
S	-0.037	0.098	-0.016	0.099	-0.011	0.109
K	-	-	-	-	-	-
Ca	-0.087	0.065	-0.154	0.079	0.037	0.167
Ti	-0.080	0.078	-0.088	0.141	0.101	0.232
V	-0.067	0.101	0.150	0.142	-0.006	0.162
Cr	0.044	0.073	-0.003	0.107	0.108	0.209
Co	-0.099	0.163	-0.076	0.238	0.081	0.342
Ni	-0.012	0.069	-0.017	0.069	0.131	0.122
Cu	0.016	0.180	0.008	0.172	0.021	0.201
Ce	0.091	0.096	0.161	0.127	0.291	0.361

Table 6.5: A summary of the mean difference and standard deviation of each element following the abundance measurements using SME with stellar parameters by Jönsson et al. (2017), uncalibrated and calibrated stellar parameters by Ahumada et al. (2019), respectively.

The comparison of Uncal-ASPCAP and Uncal+SME suggest that the manual method gives more precise abundance-measurements. These measurements should show similar trends, where the difference between these lies in the manually chosen lines and the atomic data of these. Of the 14 elements, 9 elements show a decrease in mean-difference compared with Opt-Abund.

The odd-elements with APOGEE stellar parameters show improvement in the mean compared with the ASPCAP-measurements. The Cal+SME measurements of odd-elements show a large scatter, making it hard so visualize a trend. Comparing with Opt-Abund, IR-Abund and Uncal+SME trends of odd-Z elements in figure A.1, the calibrated stellar parameters do not visualize a precise or accurate trend, showing a larger scatter with metallicity. Although, IR-Abund shows lower mean and deviation (see table 6.5), the Uncal+SME shows improvement (i.e. lowering of mean and standard deviation compared to Opt-Abund) compared with Uncal-ASPCAP.

The α-elements Mg, Si and S shows an agreement with IR-Abund and Uncal+SMe. The plateau in Mg agrees better with Opt-Abund in Uncal+SME than with Uncal-ASPCAP, and S shows sign of a plateau in the lower metallicities of Uncal+SME and Cal+SME, observed in IR-Abund. Although the Cal+SME in Mg, Si and S shows a knee-like trend, Ca and Ti shows an upward trend in Cal+SME. This upward trend is also observed in Ti using Uncal+SME, where Ca is fairly flat with metallicity.

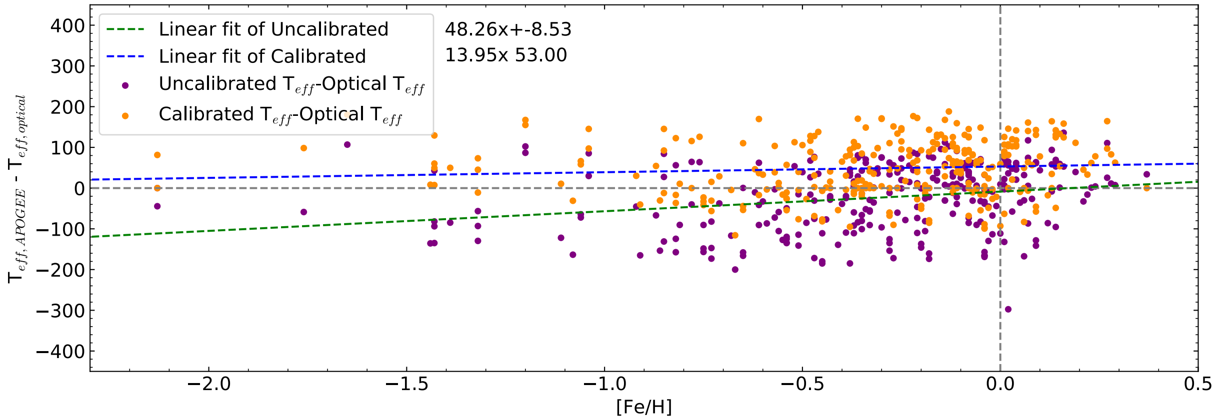

Figure 6.7: The figure shows the difference of T_{eff} with [Fe/H]. The purple scatter shows the difference between Uncal+SME T_{eff} compared with Opt-Abund of T_{eff}, showing a linear fit (green dashes). The orange scatter shows the difference of calibrated APOGEE with Opt-Abund T_{eff} with a linear fit (blue dashes).

The overall comparison of Uncal+SME and Cal+SME with IR-Abund also suggest more accurate abundance-measurements with more accurate stellar parameters. Using the same method of abundance measurements, 11 elements show a lower standard deviation using the stellar parameters, determined by Jönsson et al. (2017), compared with Uncal+SME and Cal+SME.

Ti and Ce are dependent of the T_{eff} and $\log g$, respectively, thus the trends measured can indicate the accuracy of stellar parameter measurements by ASPCAP. As previously observed in section 6.1, Ti shows a lack of knee-like trend with the APOGEE stellar parameters and as this rather flat trend with increasing metallicity is observed with Uncal+SME and Cal+SME. This Ti-abundances suggest that, as both methods use the same stellar parameters, the T_{eff} in ASPCAP-stellar parameters are determined with a [Fe/H]-dependence. The Ce-trends shows slight improvement, yet still there is a large spread.

6.2.1 Effective Temperature and Surface Gravity

APOGEE measures T_{eff} too low for lower [Fe/H] and too high for higher [Fe/H]. The difference between Opt-Abund and APOGEE measured T_{eff} can be seen in figure 6.7, showing for the T_{eff} of the calibrated APOGEE agree best with the T_{eff} determined manually with high resolution optical spectra. For higher [Fe/H] the uncalibrated ASPCAP-T_{eff} agree best with the Opt-Abund T_{eff}. This will affect the abundances and could explain the [Ti/Fe]-trends shown in the top row of figure 6.9, where the Uncal+SME Ti-abundances agree best with Opt-Abund Ti-abundances for subsolar metallicities.

The calibrated $\log g$ by APOGEE agree well with the $\log g$ determined by optical spectra. Both calibrated APOGEE and Opt-Abund of $\log g$ are calibrated to the Kepler field stars,

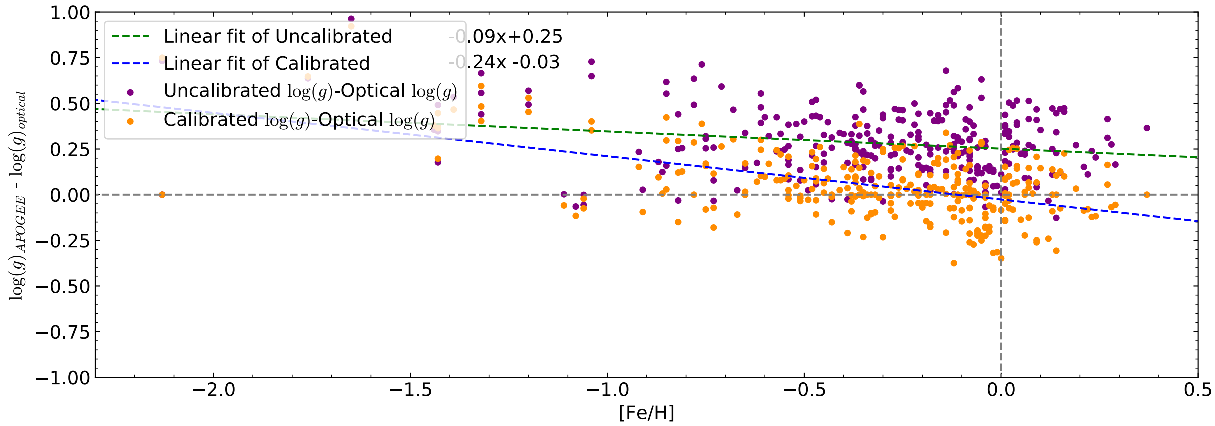

Figure 6.8: The figure shows the difference of $\log g$ with [Fe/H]. The purple scatter shows the difference between Uncal+SME $\log g$ compared with Opt-Abund of $\log g$, showing a linear fit (green dashes). The orange scatter shows the difference of calibrated APOGEE with Opt-Abund $\log g$ with a linear fit (blue dashes).

and agree well through [Fe/H], as can be seen in figure 6.8. Yet, the [Ce/Fe]-trends in figure 6.9, shows that the Uncal+SME Ce-abundances agree better with the Opt-Abund Ce-abundances. Comparing Uncal+SME Ce-abundances with Uncal-ASPCAP (figure 6.6), the Uncal+SME shows less scatter, again supporting that the method of manually choosing the lines used do give more precise for abundance measurements.

6.3 Age Determination

In this thesis, ages are determined using the mass-age relation, matching stars with PARSEC isochrones (Bressan et al. 2012).

The method to determine the ages follows the method of Feuillet et al. (2016), For detailed description on age-determination, see Feuillet et al. (2016). The masses are determined using the fundamental equations.

$$L = 4\pi R^2 \sigma_{SB} T_{\text{eff}}^4 \qquad \text{and} \qquad g = \frac{GM}{R^2} \tag{6.1}$$

$$M = \frac{gL}{4\pi G \sigma_{SB} T_{\text{eff}}^4} \tag{6.2}$$

where G is the gravitational constant, σ_{SB} is the Stefan-Boltzmann constant and M is stellar mass. The luminosities are calculated from the 2MASS K-band magnitudes with corresponding bolometric corrections by Casagrande & VandenBerg (2014). In order to determine accurate bolometric corrections, extinction coefficients are required for each star. Of the 291 spectra in this sample, 153 have available extinction coefficients. These masses are determined using T_{eff}, $\log g$, [Fe/H], [α/Fe] and bolometric magnitudes. In this work,

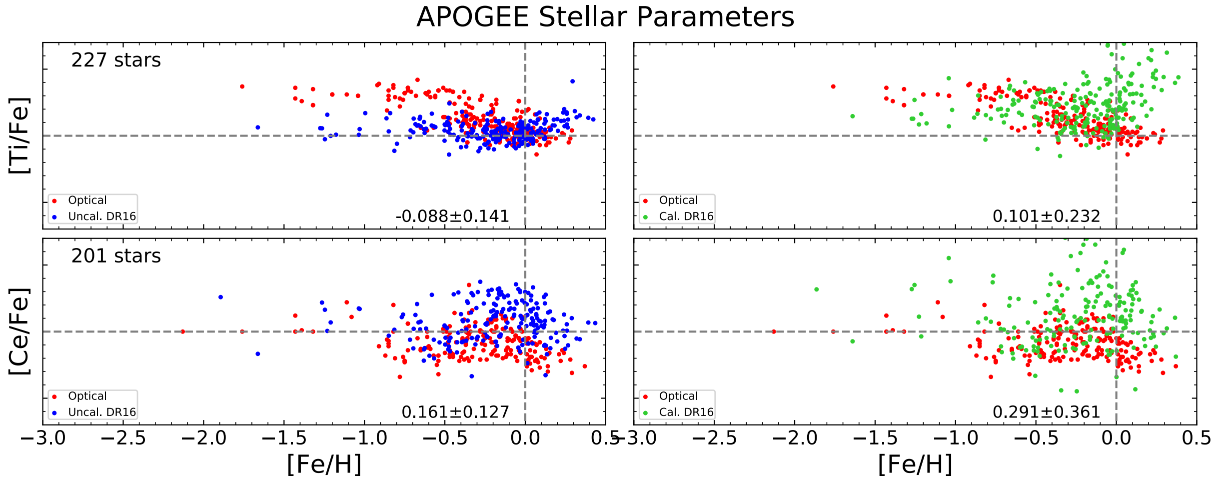

Figure 6.9: The figure shows the trends of Ti and Ce compared with Opt-Abund. The left column shows Uncal+SME and the right shows the Cal+SME. The red dots are Opt-Abund, the blue and green are Uncal+SME and Cal+SME, respectively.

[α/Fe] is taken as the mean abundance of the measured α-abundances (Mg, Si, S, Ca and Ti).

The thick disk stars are relatively older than the thin disk stars. The [Ce/Fe] vs. [Fe/H]-trend in figure 6.10 shows the lower [Ce/Fe]-abundances, coinciding with the thick disk running mean in figure 6.2, are older. Overall, the lower [Fe/H] stars show that they are older than the higher-[Fe/H] stars.

Despite the trends in figure 6.10 suggesting the ages to be population separated in Mg and Ce, the Galactocentric velocities shows a good mix in figure 6.11. Claytor et al. (2019) observed a relation with increasing V_{tot} for older stars and a higher α-abundance for older stars. In this sample, the thick disk stars have a larger velocity in the Toomre diagram, due to the method of separation (see section 4.4.3), yet these a wide range of relative ages. The thin disk stars, which have a lower velocity, also shows a wide range in age with velocities. Yet, the relative ages do show a trend of increasing V_{tot} with older stars, where the thick disk stars have a higher V_{tot} than the thin disk stars (see figure 6.12). This is also observed by Claytor et al. (2019), and is due to the stars having had more time to gain velocity.

6.4 Additional Elements

Within the APOGEE-range, few elements were not measured; P, Mn, Ge, Nd and Yb. Of these, Ahumada et al. (2019) measured P and Mn-abundances, described further below. Below are the elements unsuccessful for abundance measurements, summarized from section 5.2:

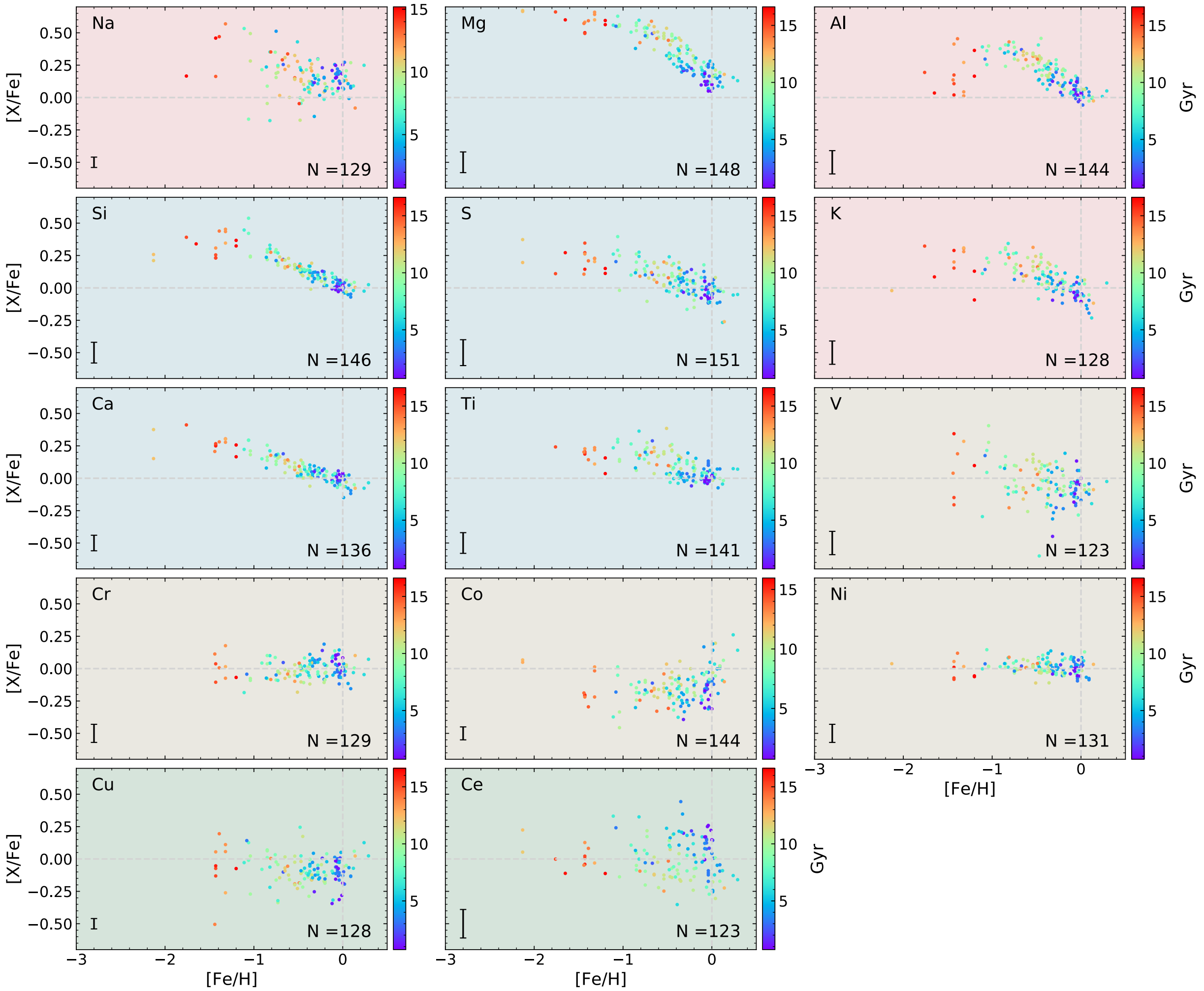

Figure 6.10: The figure shows the [X/Fe]-[Fe/H]-trends with relative ages. The number of stars are reported in the lower right corner, with the bad-fits removed.

Phosphorous There are three lines of P visible. These are highly blended with iron (15711.52 Å) and OH-molecular lines (16254.75 and 16482.93 Å), where a large spread is measured in the abundances. In the latest data release by Ahumada et al. (2019), the P-abundances of a large sample measured a large spread. Furthermore, P is measured by Hawkins et al. (2016) although there is a large spread.

Manganese Three lines of Mn are available. Mn trends of each of these lines show rapid increase in abundance around solar values, thought to be due to NLTE-effects. NLTE-effects of Mn are well known in the optical (Lomaeva et al. 2019), yet no NLTE-correction calculations are available within the APOGEE-wavelength region.

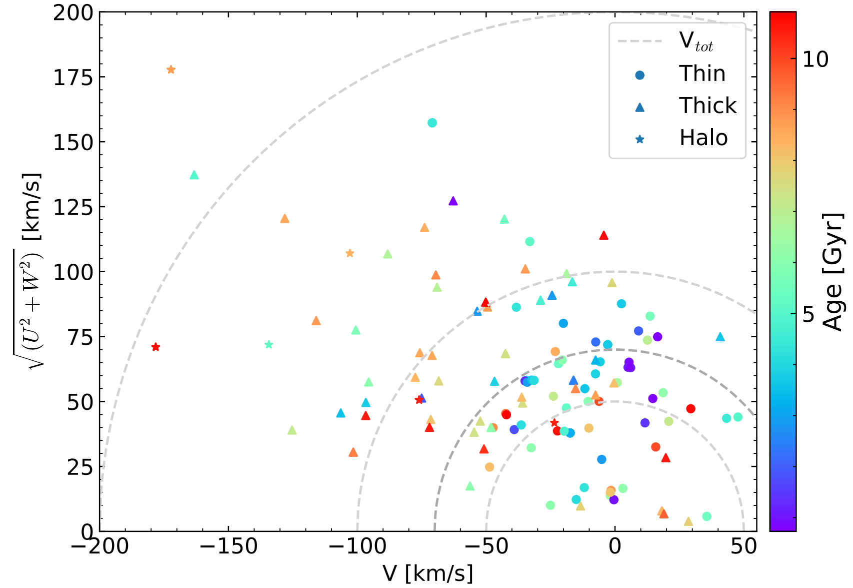

Figure 6.11: The figure shows a Toomre diagram with relative ages. The dashed lines show total velocities of 50, 70, 100 and 200 km/s, with circles marking thin disk stars, triangles marking thick disk stars and stars as halo stars. The color-scheme follows the relative ages, with red as older stars and blue as younger stars.

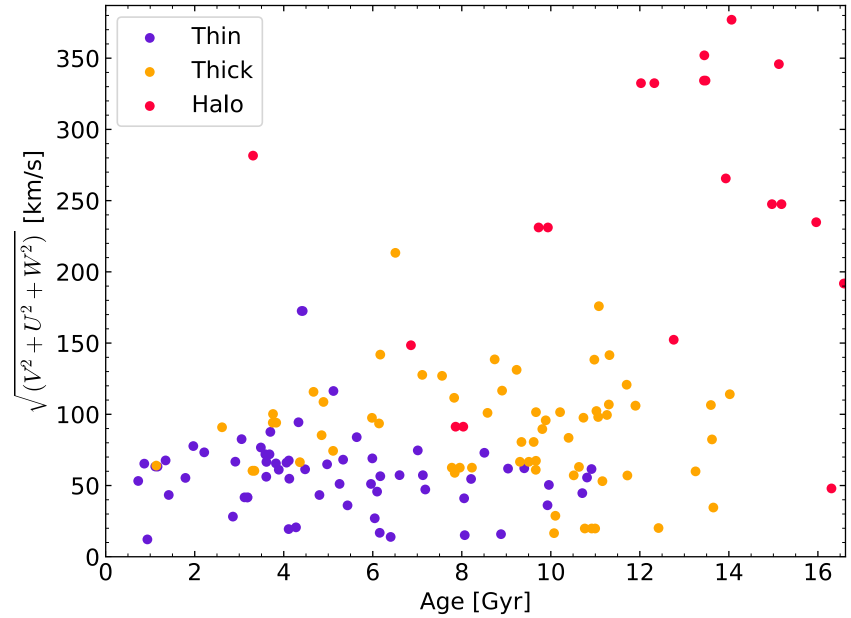

Figure 6.12: The figure shows the total velocities with ages. The thin disk stars are marked with purple, the thick disk stars are marked with orange and the halo stars are marked with red.

Germanium One Ge-line is available, where the line is highly blended with Fe. The abundances measured are overestimated due to the blending.

Rubidium One Rb-line was available within the APOGEE-range. The abundances are overestimated due to being highly blended with iron-lines. Furthermore, the line is sensitive to [Fe/H], which indicates a large spread yet the high abundances could indicate inaccurate atomic data.

Neodymium 10 Nd-lines are available, where the lines are highly blended with several other strong lines. These lines are heavily blended with Ti, Fe, Si as well as molecular lines of CN and CO. The lines each showed an overestimated abundance with a large spread.

Ytterbium There was one line available within the range. A large spread in the abundances are measured due to being highly blended with CO-molecular line.

6.5 Future Prospects

Within the H-band, 14 elements in spectra of medium-resolution are successfully measured in this thesis. It is expected that using a higher resolution would allow for better measurements of the successful and unsuccessful elemental abundances.

With the Immersion Grating Infrared Spectrometer (IGRINS) working with a resolution of 45,000 (Yuk et al. 2010; Park et al. 2014), the manual method with improved atomic data allows for more accurate and precise measurements. Preliminary results of M. Montelius' master thesis (in prep. 2021) can be seen in figures 6.13 and 6.14 of Na and Ni. This shows that a high resolution near-IR measurements agree well with the medium resolution APOGEE measurements for Na. The abundance comparison of Ni show that the higher resolution abundance measurements do show a tighter trend, and are well within the OptAbund of Ni.

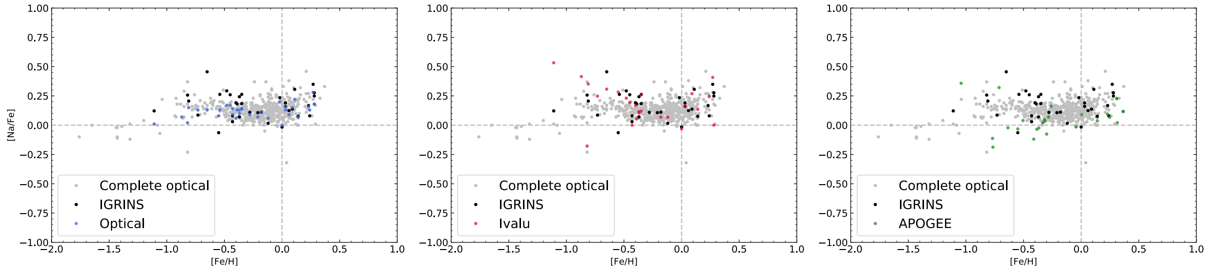

Figure 6.13: The figures shows [Na/Fe] vs. [Fe/H]-trend of sodium abundances with blue as IGRINS (R ∼ 45,000), red as this work and green as APOGEE abundance measurements. The grey measurements background measurements are the optical bench-marked sample, also used as bench-mark in this thesis.

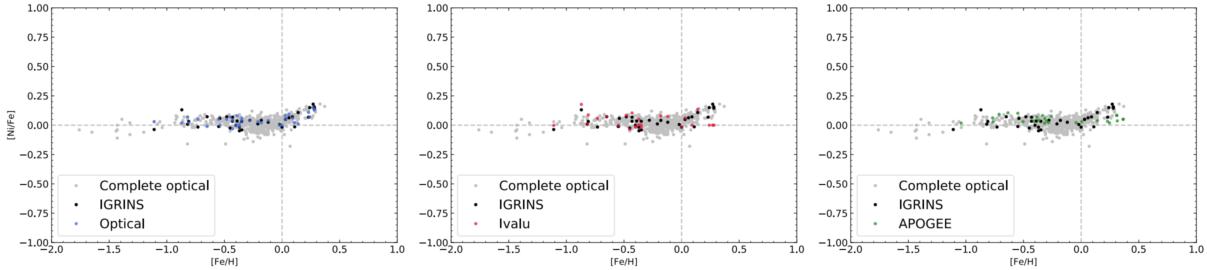

Figure 6.14: The figures shows [Na/Fe] vs. [Fe/H]-trend of sodium abundances with blue as IGRINS (R ∼ 45,000), red as this work and green as APOGEE abundance measurements. The grey measurements background measurements are the optical bench-marked sample, also used as bench-mark in this thesis.

Chapter 7

Conclusions

- 14 elemental abundances are successfully measured using 291 medium-resolution near-IR APOGEE spectra.
- The elemental groups of odd, α, iron-peak and neutron-capture elements show production channels as expected and agree well with optical abundance measurements using giants.
- Manual method of choosing and using laboratory atomic data shows more precise abundance measurements compared with APOGEE abundance measurements.
- Manual method of determining stellar parameters shows more accurate abundance measurements compared with APOGEE determined stellar parameters.

The aim of this thesis is to re-measure elemental abundances of different elemental groups using IR APOGEE spectra. The abundances are measured by synthesizing spectra using SME and manually checked how well the spectra are fitted for each line of each element. To ensure accurate and precise measurements, the sample consists of 291 K-giants, bench-marked with high resolution optical abundance measurements using the Nordic Optical Telescope.

14 elemental abundances of the four chemical groups (odd-, α-, iron-peak and neutron-capture elements) are successfully measured. The three odd-elements measured are sodium (Na), aluminium (Al) and potassium (K); the five α-elements measured are silicon (Si), magnesium (Mg), sulphur (S), calcium (Ca) and titanium (Ti); the four iron-peak elements measured are vanadium (V), chromium (Cr), cobalt (Co) and nickel (Ni); and the two neutron-capture elements measured are copper (Cu) and cerium (Ce). These abundance measurements are similar to the optical measurements by Jönsson et al. (in prep.) of the bench-marked, abundance measurements of dwarfs by Bensby et al. (2014) as well as IR-APOGEE measurements of Hawkins et al. (2016).

Thanks to the IR-regime, abundance trend of K have been measured using two lines. The abundance trend of K shows a knee-like trend, with a plateau in the lower [Fe/H] and a decrease around solar-[Fe/H], similar to α-trends. This agrees well with chemical evolution models, as K is produced mainly in SNe II.

The manual method of determining the stellar parameters and the abundance more precise and accurate measurements. APOGEE's internal abundance measurements of α-elements show promising results, but the stellar parameters of T_{eff} and $\log g$ are shown to have a systematic difference with [Fe/H], with a trend of T_{eff}:

$$T_{\mathrm{eff,APOGEE}} - T_{\mathrm{eff,opt}} = 48.3[\mathrm{Fe/H}] - 8.5 \text{ for uncalibrated stellar parameters} \tag{7.1}$$

$$T_{\mathrm{eff,APOGEE}} - T_{\mathrm{eff,opt}} = 14.0[\mathrm{Fe/H}] + 53.0 \text{ for calibrated stellar parameters} \tag{7.2}$$

and a systematic trend of $\log g$:

$$\log(g)_{\mathrm{APOGEE}} - \log(g)_{\mathrm{opt}} = -0.1[\mathrm{Fe/H}] + 0.3 \text{ for uncalibrated stellar parameters} \tag{7.3}$$

$$\log(g)_{\mathrm{APOGEE}} - \log(g)_{\mathrm{opt}} = -0.2[\mathrm{Fe/H}] - 0.0 \text{ for calibrated stellar parameters} \tag{7.4}$$

The combination of synthesizing a spectra with updated atomic data and **manually** choosing the lines used show more accurate and precise abundance measurements . Using the stellar parameters of APOGEE, 9 elemental abundances show to measure abundances more accurate using the manual method presented here. Furthermore, 11 of the 14 elemental abundances show more precise measurements with the manual method using the stellar parameters of APOGEE. It can be concluded that the manual method gives more accurate and precise elemental abundance measurements. The manual abundance analysis of this study shows that it is valuable to study details of our Milky Way with a large sample of accurate and precise measurements. This gives the achievability of future investigations of possible sub-populations.

Thanks to great measurements by Gaia and distance-calculation by McMillan (2018), the ages of 153 K-giants of this sample are determined. The relative ages determined of this sample shows the older stellar population, mainly thick-disk stars, to have greater velocities than the younger, thin disk stars. This is in well-agreement with previous studies.

Future improvements are also investigation within the same wavelength region at higher resolution. With the preliminary results from manual analysis of IGRINS spectra, I am optimistic that elemental abundances, not possible in this thesis, can be measured. The accurate and precise abundance measurement using IR APOGEE spectra, the manual analysis show great results. With this, I conclude that manual abundance analysis using IR APOGEE spectra can be used to constrain the chemical evolution of our Milky Way.

Bibliography

Adibekyan, V. Z., Santos, N. C., Sousa, S. G., & Israelian, G. 2011, A&A, 535, L11

Adibekyan, V. Z., Sousa, S. G., Santos, N. C., et al. 2012, A&A, 545, A32

Ahumada, R., Allende Prieto, C., Almeida, A., et al. 2019, arXiv e-prints, arXiv:1912.02905

Allende Prieto, C., Beers, T. C., Wilhelm, R., et al. 2006, ApJ, 636, 804

Battistini, C. & Bensby, T. 2015, A&A, 577, A9

Battistini, C. & Bensby, T. 2016, A&A, 586, A49

Bensby, T., Feltzing, S., & Oey, M. S. 2014, A&A, 562, A71

Bergemann, M. 2014, Analysis of Stellar Spectra with 3-D and NLTE Models, 187–205

Bergemann, M. & Nordlander, T. 2014, arXiv e-prints, arXiv:1403.3088

Biémont, E. 1973, Bulletin de la Societe Royale des Sciences de Liege, 42, 206, (BIEMa)

Biemont, E., Quinet, P., & Zeippen, C. J. 1993, , 102, 435, (BQZ)

Blackwell-Whitehead, R. J., Lundberg, H., Nave, G., et al. 2006, Monthly Notices Roy. Astron. Soc., 373, 1603, (BLNP)

Bland-Hawthorn, J. & Gerhard, O. 2016, ARA&A, 54, 529

Bravo, E. & Martínez-Pinedo, G. 2012, , 85, 055805

Bressan, A., Marigo, P., Girardi, L., et al. 2012, MNRAS, 427, 127

Buder, S., Asplund, M., Duong, L., et al. 2018, Monthly Notices of the Royal Astronomical Society, 478, 4513–4552

Burbidge, E. M., Burbidge, G. R., Fowler, W. A., & Hoyle, F. 1957, Reviews of Modern Physics, 29, 547

Busso, M., Gallino, R., & Wasserburg, G. J. 1999, ARA&A, 37, 239

Casagrande, L. & VandenBerg, D. A. 2014, MNRAS, 444, 392

Chiappini, C., Matteucci, F., & Gratton, R. 1997, ApJ, 477, 765

Clayton, D. 2003, Handbook of Isotopes in the Cosmos: Hydrogen to Gallium (Cambridge University Press; 1 edition (October 6, 2003))

Clayton, D. D. 1983, Principles of stellar evolution and nucleosynthesis

Claytor, Z. R., van Saders, J. L., Santos, A. R. G., et al. 2019, arXiv e-prints, arXiv:1911.04518

Cunha, K., Smith, V. V., Hasselquist, S., et al. 2017, ApJ, 844, 145

Delgado Mena, E., Tsantaki, M., Adibekyan, V. Z., et al. 2017, A&A, 606, A94

Edvardsson, B., Andersen, J., Gustafsson, B., et al. 1993, A&A, 500, 391

Feuillet, D. K., Bovy, J., Holtzman, J., et al. 2016, ApJ, 817, 40

Forsberg, R., Jönsson, H., Ryde, N., & Matteucci, F. 2019, A&A, 631, A113

Gaia Collaboration, Brown, A. G. A., Vallenari, A., et al. 2018, A&A, 616, A1

García Pérez, A. E., Allende Prieto, C., Holtzman, J. A., et al. 2016, AJ, 151, 144

Gilmore, G., Randich, S., Asplund, M., et al. 2012, The Messenger, 147, 25

Grevesse, N., Asplund, M., & Sauval, A. J. 2007, , 130, 105

Grimmett, J. J., Karakas, A. I., Heger, A., & Müller, B. 2019, arXiv e-prints, arXiv:1911.05901

Gustafsson, B., Edvardsson, B., Eriksson, K., et al. 2008, A&A, 486, 951

Hasselquist, S., Shetrone, M., Cunha, K., et al. 2016, ApJ, 833, 81

Hawkins, K., Masseron, T., Jofré, P., et al. 2016, A&A, 594, A43

Hayden, M. R., Bovy, J., Holtzman, J. A., et al. 2015, ApJ, 808, 132

Holtzman, J. A., Hasselquist, S., Shetrone, M., et al. 2018, AJ, 156, 125

Holtzman, J. A., Shetrone, M., Johnson, J. A., et al. 2015, AJ, 150, 148

Hoyle, F. 1946, MNRAS, 106, 343

Jofré, P., Heiter, U., Soubiran, C., et al. 2015, A&A, 582, A81

Jönsson, H., Ryde, N., Nordlander, T., et al. 2017a, A&A, 598, A100

Jönsson, H., Ryde, N., Schultheis, M., & Zoccali, M. 2017b, A&A, 600, C2

Jordan, G. C., Gupta, S. S., & Meyer, B. S. 2003, , 68, 065801

Jönsson, H., Ryde, N., Nordlander, T., et al. 2017, A&A, 598, A100

Kratz, K.-L., Farouqi, K., Pfeiffer, B., et al. 2007, ApJ, 662, 39

Kurucz, R. L. 2007, Robert L. Kurucz on-line database of observed and predicted atomic transitions

Kurucz, R. L. 2008, Robert L. Kurucz on-line database of observed and predicted atomic transitions

Kurucz, R. L. 2009, Robert L. Kurucz on-line database of observed and predicted atomic transitions

Kurucz, R. L. 2010, Robert L. Kurucz on-line database of observed and predicted atomic transitions

Kurucz, R. L. 2011, Robert L. Kurucz on-line database of observed and predicted atomic transitions

Kurucz, R. L. 2012, Robert L. Kurucz on-line database of observed and predicted atomic transitions

Lind, K., Bergemann, M., & Asplund, M. 2012, MNRAS, 427, 50

Lodders, K. 2010, Astrophysics and Space Science Proceedings, 16, 379

Lomaeva, M., Jönsson, H., Ryde, N., Schultheis, M., & Thorsbro, B. 2019, arXiv e-prints, arXiv:1903.01476

Majewski, S. R., Schiavon, R. P., Frinchaboy, P. M., et al. 2017, AJ, 154, 94

Matteucci, F. & Greggio, L. 1986, A&A, 154, 279

McMillan, P. J. 2018, Research Notes of the American Astronomical Society, 2, 51

Minchev, I., Anders, F., Recio-Blanco, A., et al. 2018, MNRAS, 481, 1645

Morgan, J. A. 1980, ApJ, 238, 674

Newton, I. 1672, Philosophical Transactions of the Royal Society of London Series I, 7, 5084

Nidever, D. L., Holtzman, J. A., Allende Prieto, C., et al. 2015, AJ, 150, 173

Nordlander, T. & Lind, K. 2017, A&A, 607, A75

Park, C., Jaffe, D. T., Yuk, I.-S., et al. 2014, Society of Photo-Optical Instrumentation Engineers (SPIE) Conference Series, Vol. 9147, Design and early performance of IGRINS (Immersion Grating Infrared Spectrometer), 91471D

Pehlivan Rhodin, A., Hartman, H., Nilsson, H., & Jönsson, P. 2017, A&A, 598, A102

Piskunov, N. & Valenti, J. A. 2017, A&A, 597, A16

Ralchenko, Y., Kramida, A., Reader, J., & NIST ASD Team. 2010, NIST Atomic Spectra Database (ver. 4.0.0), [Online].

Romano, D. & Matteucci, F. 2007, MNRAS, 378, L59

Ryabchikova, T., Piskunov, N., Kurucz, R. L., et al. 2015, , 90, 054005

Sarmento, P., Delgado Mena, E., Rojas-Ayala, B., & Blanco-Cuaresma, S. 2020, arXiv e-prints, arXiv:2001.01995

Shetrone, M., Bizyaev, D., Lawler, J. E., et al. 2015, , 221, 24

Siegel, D. M., Barnes, J., & Metzger, B. D. 2019, Nature, 569, 241

Spitoni, E. & Matteucci, F. 2011, A&A, 531, A72

Spitoni, E., Silva Aguirre, V., Matteucci, F., Calura, F., & Grisoni, V. 2019, A&A, 623, A60

Valenti, J. A. & Piskunov, N. 1996, , 118, 595

Watson, D., Hansen, C. J., Selsing, J., et al. 2019, Nature, 574, 497

Wickliffe, M. E., Lawler, J. E., & Nave, G. 2000, J. Quant. Spectrosc. Radiat. Transfer, 66, 363, (WLN)

Wiese, W. L., Smith, M. W., & Miles, B. M. 1969, Atomic transition probabilities. Vol. 2: Sodium through Calcium. A critical data compilation, ed. Wiese, W. L., Smith, M. W., & Miles, B. M. (US Government Printing Office), (WSM)

Wood, M. P., Lawler, J. E., & Shetrone, M. D. 2014, ApJ, 787, L16

Woosley, S. E. & Weaver, T. A. 1995, , 101, 181

Yuk, I.-S., Jaffe, D. T., Barnes, S., et al. 2010, Society of Photo-Optical Instrumentation Engineers (SPIE) Conference Series, Vol. 7735, Preliminary design of IGRINS (Immersion GRating INfrared Spectrograph), 77351M

Zasowski, G., Johnson, J. A., Frinchaboy, P. M., et al. 2013, AJ, 146, 81

Appendix A

Appendix

A.1 Poster for Astronomdagarna

A.2 Poster for Greenland Science Week

A.3 Log(gf)-Values

Element	Wavelength [Å]	Used $\log(gf)$	APOGEE $\log(gf)$	Gustafsson et al. (2008) $\log(gf)$
Al 1	16718.97	-0.148	-0.186	0.152
Al 1	16750.6	-0.404	-0.506	0.408
Al 1	16763.37	-0.514	-1.568	-0.55
Ca 1	16136.82	-0.363	-0.585	0.018
Ca 1	16150.76	-0.032	-0.237	0.362
Ca 1	16155.24	-0.496	-0.758	-0.118
Ca 1	16157.36	0.246	-0.219	0.492
Ca 1	16197.08	0.254	0.089	0.638
Ca 2	16561.06	0.389	0.441	0.449
Ce 2	15277.65	-1.94	-1.94	-
Ce 2	15784.75	-1.54	-1.51	-
Ce 2	15958.4	-1.71	-1.83	-
Ce 2	15977.12	-2.1	-2.019	-
Ce 2	16327.32	-2.4	-2.4	-
Ce 2	16376.48	-1.79	-1.965	-
Ce 2	16595.18	-2.19	-2.186	-
Ce 2	16722.51	-1.65	-1.83	-
Co 1	16757.64	-0.923	-2.246	-1.369
Cr 1	15680.06	0.152	-0.001	0.27
Cr 1	15860.21	0.021	-0.077	0.129
Cr 1	15974.01	-2.291	0.807	-1.989

Cr 1	16015.32	-0.21	-0.141	-0.105
Cu 1	16005.54	-0.045	-0.822	-0.05
Cu 1	16006.74	0.255	-0.376	0.25
Cu 1	16638.98	0.07	-	0.23
Ge 1	16759.76	-0.3	-0.109	-0.3
K 1	15163.09	0.689	0.632	0.64
K 1	15168.4	0.48	0.441	0.48
Mg 1	15740.7	-0.223	-0.323	-0.24
Mg 1	15748.99	0.129	0.049	-0.06
Mg 1	15765.84	0.4	0.32	0.38
Mg 1	15879.56	-1.326	-1.354	-1.38
Mg 1	15886.19	-1.896	-1.696	-1.82
Mg 1	15889.52	-1.876	-2.153	-2.0
Mg 1	15948.38	-2.0	-2.004	-2.41
Mg 1	15954.45	-1.82	-0.828	-1.82
Mg 1	16595.58	-2.09	-2.137	-1.94
Mn 1	15159.15	0.619	-0.016	-0.437
Mn 1	15217.74	0.52	-0.85	-2.716
Mn 1	15262.49	0.393	-0.261	-
Na 1	16373.87	-1.328	-1.853	-1.33
Na 1	16388.85	-1.027	-2.552	-1.03
Nd 2	15284.46	-2.13	-2.13	-
Nd 2	15368.14	-1.55	-1.55	-
Nd 2	15912.29	-2.39	-2.39	-
Nd 2	15977.95	-2.47	-2.47	-
Nd 2	16053.63	-2.2	-2.2	-
Nd 2	16262.04	-1.99	-1.99	-
Nd 2	16303.78	-2.11	-2.11	-
Nd 2	16382.92	-1.48	-1.48	-
Nd 2	16558.21	-2.4	-2.4	-
Nd 2	16634.67	-2.37	-2.37	-
Ni 2	15170.06	-2.36	-2.36	-
Ni 1	15173.58	-0.547	-0.782	-0.685
Ni 2	15195.27	-0.948	-1.258	-
Ni 2	15199.62	-0.501	-0.64	-0.639
Ni 2	15290.72	-0.889	-0.897	-0.934
Ni 2	15555.38	0.218	0.007	0.065
Ni 2	15605.66	0.017	-0.247	-
Ni 1	15632.62	0.125	0.074	-0.247
Ni 1	15753.61	-0.602	-0.911	-0.746
Ni 1	16136.1	-0.003	-0.156	-0.165
Ni 1	16278.8	-1.585	-1.277	-2.121

Ni 1	16310.5	0.222	-0.425	0.07
Ni 3	16335.62	-9.7	-9.7	-
Ni 1	16363.09	0.588	0.275	0.442
Ni 1	16388.74	-0.253	-0.674	0.1
Ni 1	16480.55	-0.81	-0.716	-0.88
Ni 1	16536.17	-0.156	-0.158	0.173
Ni 1	16550.38	0.266	0.191	0.588
Ni 1	16584.44	-0.709	-0.485	-0.92
Ni 1	16589.44	-0.345	-0.533	-0.493
Ni 1	16673.7	0.388	0.306	0.678
Ni 1	16761.24	-0.307	-0.515	0.019
Ni 1	16815.46	-0.417	-0.501	-0.547
Ni 1	16818.74	0.473	0.347	0.762
Ni 1	16867.28	0.115	-0.03	-0.03
Ni 1	16875.17	-1.772	-2.355	-
Ni 1	16945.31	-0.765	-0.899	-1.217
Ni 1	16996.24	0.458	0.273	0.31
P 1	15711.52	-0.51	-0.404	-0.72
P 1	16254.75	0.0	-2.35	0.0
P 1	16482.93	-0.29	-0.273	-0.4
Rb 1	15289.48	0.42	-1.58	0.42
S 1	15403.77	0.73	0.348	0.52
S 1	15469.82	-0.05	-0.31	-0.22
S 1	15475.62	-0.52	-0.744	-0.7
S 1	15478.48	0.18	-0.04	0.0
S 1	16590.96	-0.76	-1.462	-1.13
S 1	16593.2	-0.56	-1.088	-0.81
Si 1	15376.89	-0.973	-0.701	-0.703
Si 1	15557.79	-0.81	-0.82	-0.812
Si 1	15884.47	-0.826	-0.945	-0.825
Si 1	15888.44	0.009	-0.102	-1.877
Si 1	15960.08	0.397	0.13	0.087
Si 1	16060.02	-0.484	-0.452	-0.483
Si 1	16094.8	-0.105	-0.088	-0.144
Si 1	16163.71	-0.862	-0.858	-0.861
Si 1	16215.69	-0.631	-0.565	-0.631
Si 1	16241.85	-0.77	-0.762	-0.767
Si 1	16380.14	-0.465	-0.827	-0.465
Si 1	16381.55	-0.951	-0.571	-0.459
Si 1	16680.77	-0.227	-0.138	-0.141
Si 1	16828.18	-1.028	-1.058	-1.028
Ti 1	15186.7	-2.32	-2.39	-2.535

Ti 1	15334.84	-0.96	-1.04	-1.149
Ti 1	15543.75	-1.08	-1.16	-1.273
Ti 1	15602.84	-1.435	-1.64	-1.544
Ti 1	15698.98	-2.01	-2.11	-2.218
Ti 1	15715.57	-1.2	-1.28	-1.359
Ti 2	15873.84	-1.9	-2.061	-1.925
Ti 1	16330.54	-0.89	-0.966	-0.983
Ti 1	16635.15	-1.582	-1.771	-2.178
V 1	15567.69	-1.868	-2.67	-3.966
V 1	15700.61	-0.45	-1.381	-3.905
V 1	15924.81	-1.108	-2.323	-1.177
V 1	15939.87	-0.353	-1.344	-1.175
V 1	16200.28	-0.237	-0.778	-1.329
V 1	16570.56	-1.535	-2.315	-1.597
Yb 2	16498.4	-0.64	-0.625	-

Table A.1: The table shows three different values of the oscillator strength by the VALD-linelist, which has been updated with available laboratory log(gf)-values as well as astrophysical log(gf)-values, the APOGEE DR16 log(gf)-values, which is calculated with a combination of astrophysical log(gf) of the Sun, α Boo and μ Leo, and the Gustafsson et al. (2008) log(gf)-values, which are astrophysical log(gf) measurements of the Sun for each element of interest with wavelength indicated.

A.4 Comparison Plots - Manual Analysis with APOGEE Stellar Parameters

LUNDS UNIVERSITET

Abundances of Giant Stars in the Local Disk

Manual Analysis of IR APOGEE Spectra

Ivalu Barlach Christensen[1] Nils Ryde[1] Henrik Jönsson[1,2]
[1]Lund Observatory, Department of Astronomy and Theoretical Physics, Lund University, Box 43, SE-221 00 Lund
[2]Materials Science and Applied Mathematics, Malmö University, SE-205 06 Malmö

Overview

Elemental abundances are great tracers of **Galactic chemical evolution**. The purpose of this work is to investigate the chemical evolution of the Milky Way by determining several **elemental abundances of giants in the local disk**. The data used is a subset of IR spectra from the **APOGEE survey**, of stars that has also been analyzed using independent optical spectra. The determined abundances are compared to the ones derived by the APOGEE analysis pipeline as well as the ones from the optical analysis. Investigating abundances helps constrain Galactic chemical evolution models.

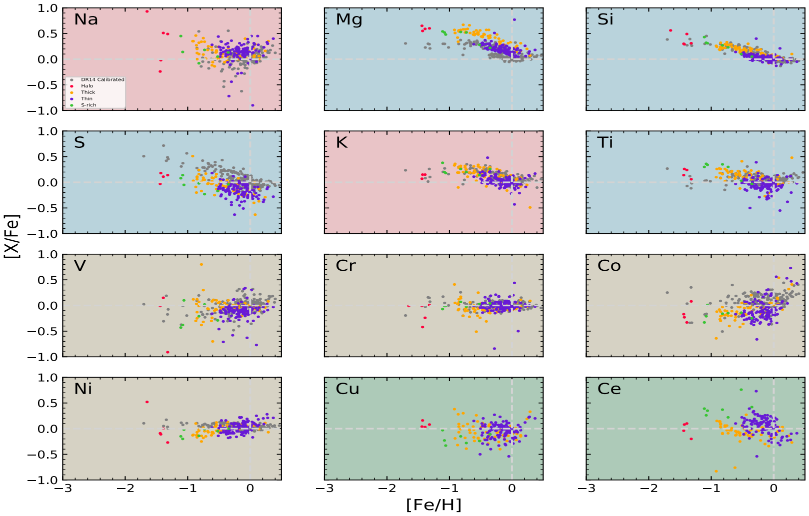

Sample

Sample	187 K-Giants
Spectral Range	1.5 - 1.7 μm
Resolution	∼ 22 500
S/N	∼ 100

Infrared allows observations in the Galactic plane, as the dust is penetrable in this range.

K-giants enables to probe deeper in the Galaxy and the chemical history.

Medium resolution and high signal-to-noise ratio provides sufficient spectra for abundance measurements.

Why Re-analyze?

The industrialized abundance measurements, using APOGEE analysis pipeline, are generalized for all stars, yet there are problems for some elements. The manual re-analysis will specialize in a specific type of star, ensuring, with bench marked high resolution optical abundance measurement, a high accuracy in these measurements as well as aiming to solve the problems by pipeline measurements.

Elements of Interest

Investigating elements with different production channels ensure a broader view of the Galactic chemical evolution. Light- and α-elements are mainly formed in exploding massive stars, iron-peak elements in exploding white dwarfs and neutron-capture elements are formed in neutron rich sources, eg. merging neutron stars.

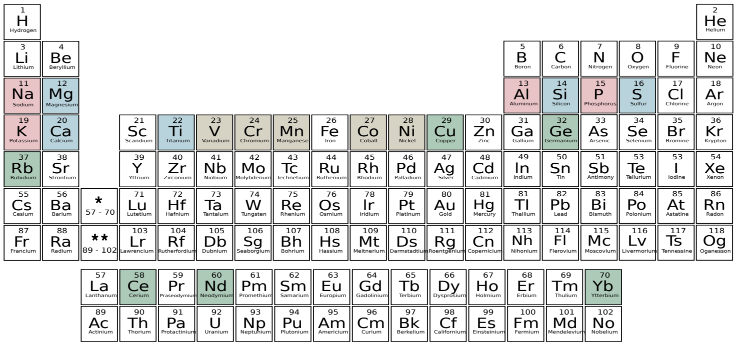

Method

The abundances are determined using Spectroscopy Made Easy by synthesizing a spectrum compared to the observed spectrum with line of interest.

Upcoming Work

- Improve the measurements using the bench marked optical measurements
- Can more iron-peak and r-process elements be measured?
- Expand method to larger set of K-giant spectra

Contact e-mail: ivalubarlach@gmail.com

LUNDS UNIVERSITET

Målinger af kæmpestjerner i vores galakse

Manuel analyse af infrarøde spektra

Ivalu Barlach Christensen[1] Nils Ryde[1] Henrik Jönsson[1,2]

[1]Lund Observatory, Department of Astronomy and Theoretical Physics, Lund University, Box 43, SE-221 00 Lund
[2]Materials Science and Applied Mathematics, Malmö University, SE-205 06 Malmö

Oversigt

Efter Big Bang blev Universet fyldt med de mindste grundstoffer - hydrogen og helium. Siden da, er de større grundstoffer blevet skabt inde i stjernernes indre og frigivet under eksplosion kaldet supernova. Ved at følge Kopernikus' tankegang om at Jorden ikke er speciel, så er vores hjem-galakse, Mælkevejen, ikke speciel. Med viden om hvordan stjerner dannes og hvordan stjernerne danner grundstoffer, kan man undersøge hvordan stjernerne i galaksen har udviklet sig gennem tiden. Ved at bruge stjerner med forskellige aldre, kan man undersøge forskellen af grundstofferne mellem stjerner, der indikerer udviklingen. Der er grupperinger af grundstoffer i det periodiske system, hvor de har forskellige måder at danne sig på. Ved at bruge kæmpestjerner der ligger i forskellige steder i vores galakse, viser det sig at der er to stjernegrupper; gamle stjerner, der bevæger sig hurtigt i alle retninger i vores galakse, og yngre stjerner, der cirkulerer rundt om vores galakse i et roligt tempo. Før de gamle stjerners fødsel, har der ikke været mange eksplosioner. Det er interessant at forstå hvordan vores galakses midte har udviklet sig. Kemisk har stjerner i galaksens midte vist sig at være anderledes end de stjerner vi ser nær Solen. En af måderne hvorpå kan undersøge stjernerne i galaksens midte er at bruge infrarøde målinger.

Stjernernes udvikling

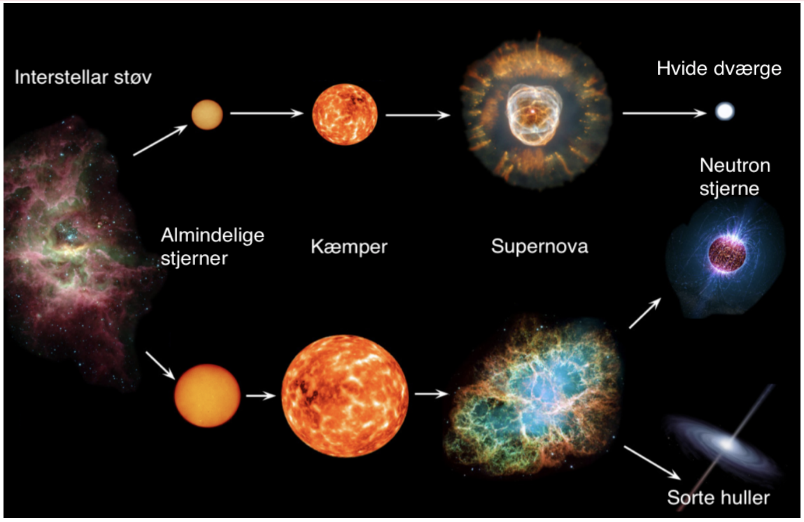

Billedet viser små og store stjerners liv. Forskellen mellem store og små stjerner her er hvad der bliver pustet ud under supernova fasen. Disse danner forskellige grundstoffer. De to forskellige eksplosioner viser 1) planetarisk tåge, der er rester fra en mindre stjerne, og 2) supernova, der er rest fra en kæmpestjerne. Neutron stjerner og sorte huller, der er rester fra kæmpestjerner, danner også andre grundstoffer.

Undersøgelser

Stjerner	187 Kæmpestjerner
Bølgelængde	1.5 - 1.7 μm
Løsning	~ 22 500
S/N	~ 100

Stjerner udsender **infrarødt lys**. Infrarødt lys kan ses gennem støv i rummet, jo tættere på galaksens midte man kigger, des mere støv er der. Udover dette måles **kæmpestjerner**, da disse lyser stærkere og derfor kan ses længere væk fra Jorden og tættere mod midten af Mælkevejen. Der bruges et teleskop kaldet Apache Point Observatory Galactic Evolution Experiment (APOGEE), der måler masser af stjerner på samme tid. Astrofysikere bliver derfor nødt til at undersøge disse målinger hurtigt og nøjagtigt. En metode, der undersøger tusinder af kæmperstjerner nær galaksens midte med **høj nøjagtighed**, bliver udviklet, og derfra vil den kemiske udvikling af vores Mælkevej kunne blive undersøgt med høj nøjagtighed.

Undersøgelser af galaksens udvikling med grundstoffer

Det periodiske system (venstre) viser hvilke grundstoffer der bliver undersøgt med APOGEE. De forskellige farver viser grundstoffer der bliver formet på samme måde. Et eksempel på hvordan man undersøger udviklingen af silikone og hvordan de to stjernegrupper er, kan ses til højre.

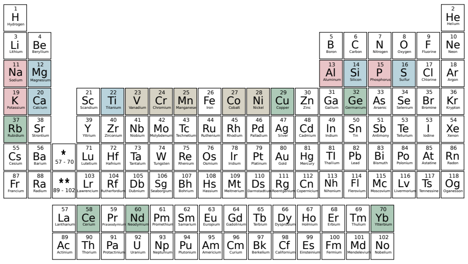

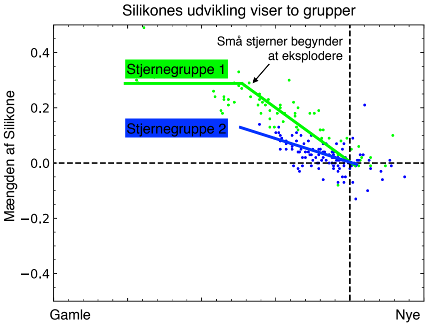

Kontakt: ivalubarlach@gmail.com

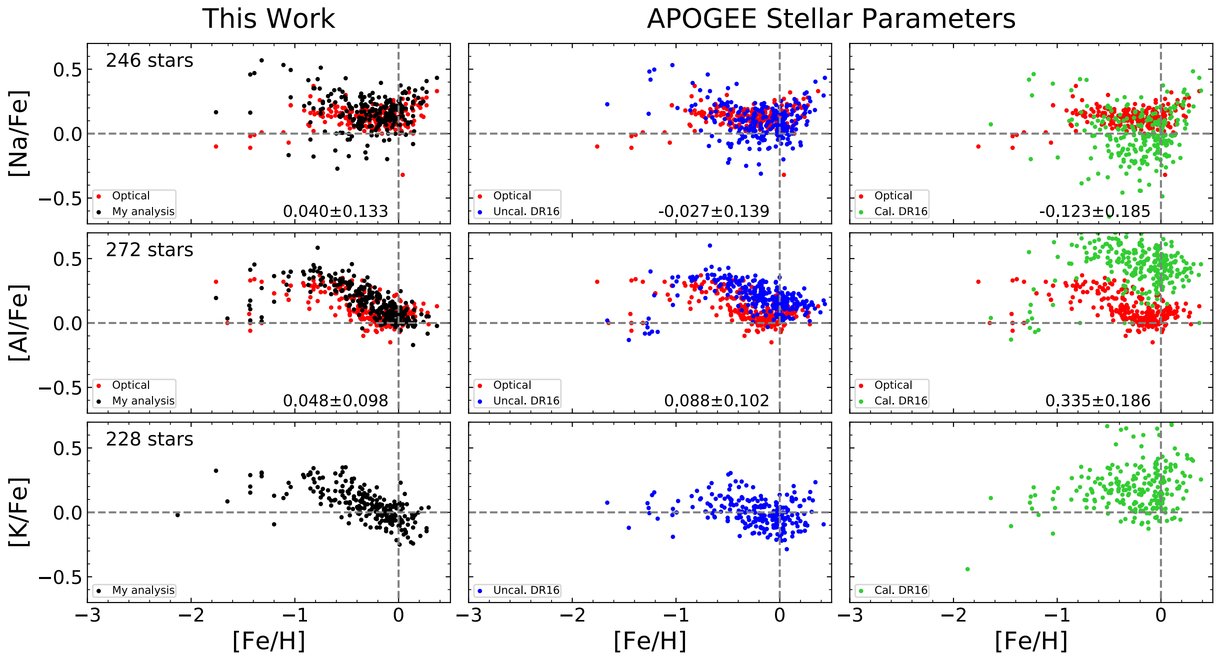

Figure A.1: The figure shows the abundances of light elements Na, Al and K of IR-Abund (black), Uncal+SME (blue) and Cal+SME (green) compared with the Opt-Abund by Jönsson et al. (in prep.). The number of stars compared can be seen on the top left, with the mean and standard deviation on the bottom right of each sub-figure

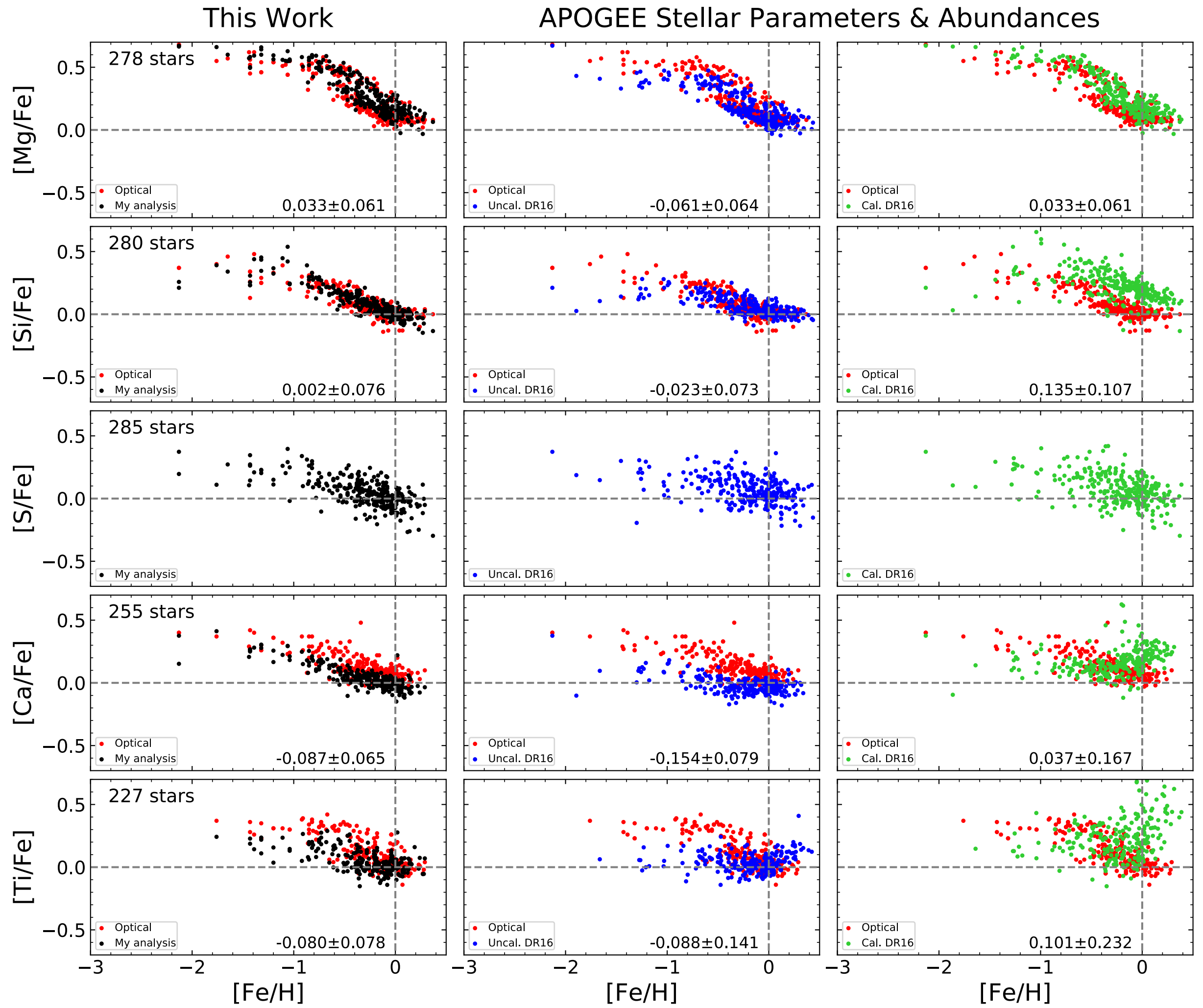

Figure A.2: The figure shows the comparison of α-elements Mg, Si, S, Ca and Ti of IR-Abund and abundance measurements using SME with ASPCAP stellar parameters, with the same description as figure A.1.

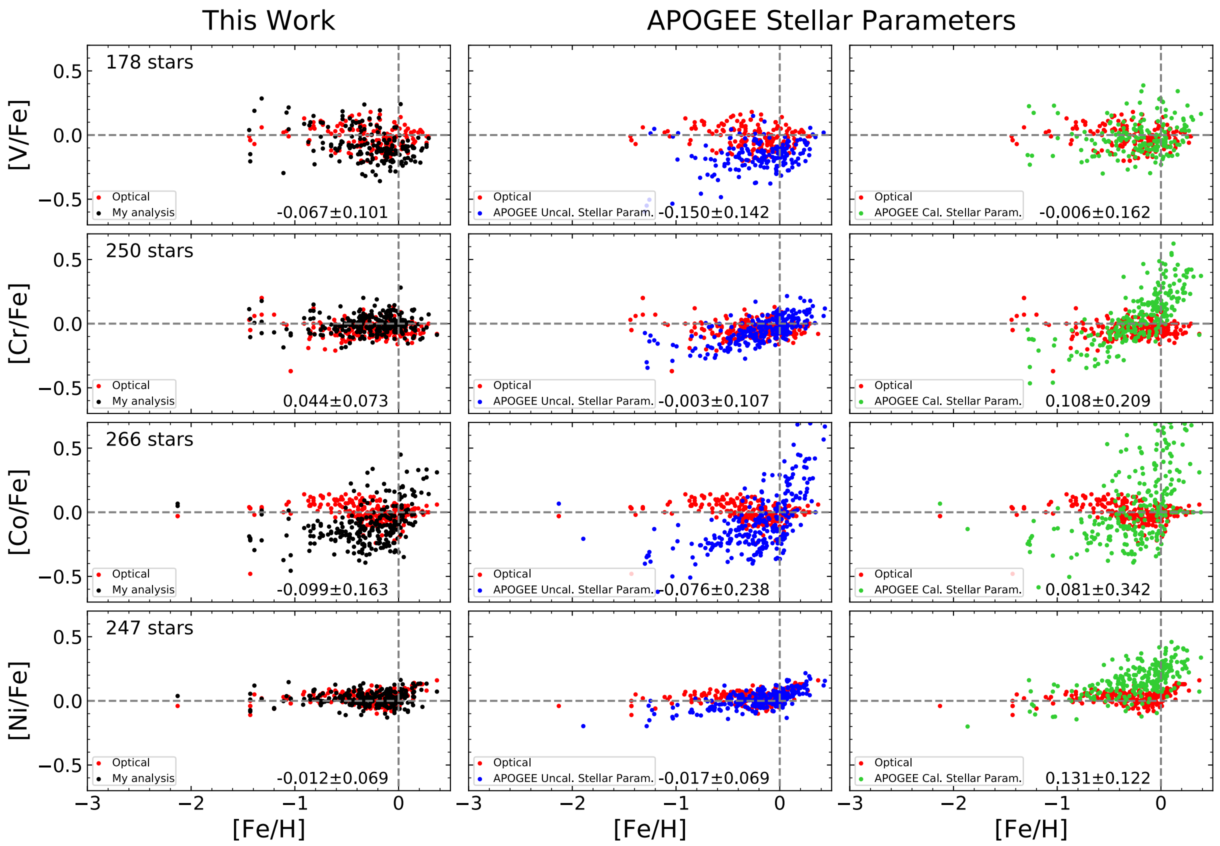

Figure A.3: The figure shows the comparison of iron-peak elements V, Cr, Co and Ni of IR-Abund and abundance measurements using SME with ASPCAP stellar parameters, with the same description as figure A.1.

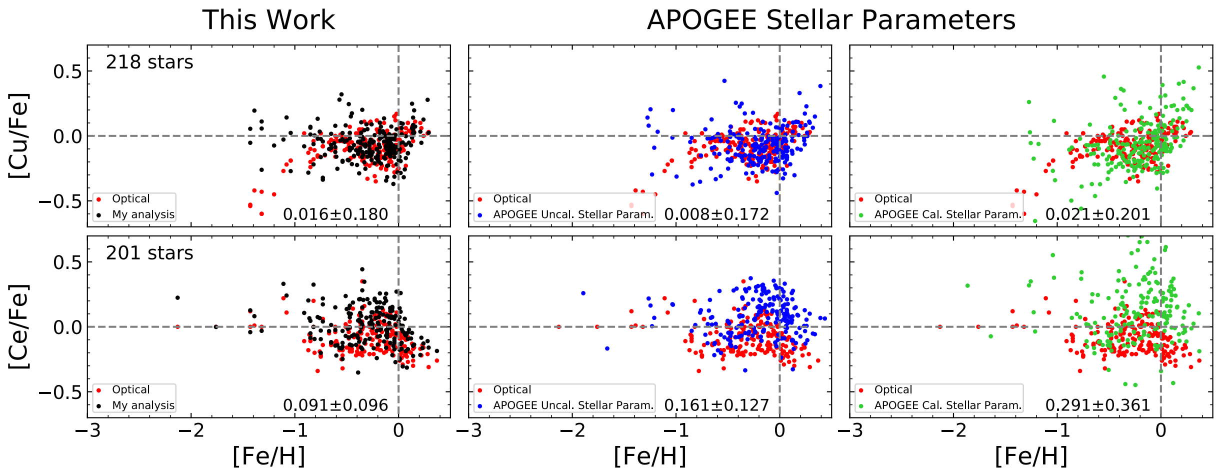

Figure A.4: The figure shows the comparison of netron-capture elements Cu and Ce of IR-Abund and abundance measurements using SME with ASPCAP stellar parameters, with the same description as figure A.1.